Theoretical and Experimental Study on Some Aspects of Resistivity Measurement of Conductive Media Using Both the Four and the Two-Electrode Methods

Chong Chee Earn @ Steven Chong

School of Electrical & Electronic Engineering

A thesis submitted to the Nanyang Technological University
in fulfillment of the requirement for the degree of
Doctor of Philosophy

2007

ACKNOWLEDGMENTS

There are many people I wish to thank for their support and encouragement in helping me overcome many difficulties that I have encountered during my work for this thesis.

First and foremost, I would like to express my deepest gratitude and sincere appreciation to my supervisor, Associate Professor Tan Yoke-Lin for being an inspirational mentor and for his guidance and support in my pursual for higher degree. His professionalism, extensive knowledge and passion for research always inspire me throughout the course of my research.

My sincere appreciation also extends to the technical staff from the Power Engineering Design Laboratory, the System Protection Laboratory, the Power System Laboratory, the Energy and Machines Laboratory, and the Environmental Laboratory. This work would not have been possible without their great assistance and valuable equipments for the conduct of my experiments.

Finally, I would like to thank my parents, my sister and my girlfriend for their endless love, patience and understanding. Last but not least, I will like to thank all my friends who have encouraged and supported me all these years.

TABLE OF CONTENTS

ACKNOWLEDGMENTS ii

TABLE OF CONTENTS iii

SUMMARY xi

LIST OF FIGURES xiii

LIST OF TABLES xviii

CHAPTER 1 - INTRODUCTION 1

1.1 Motivation and Purpose 1

1.2 Objectives of Thesis 5

1.3 Major Contributions of Thesis 6

1.4 Organisation of Thesis 9

CHAPTER 2 - RESISTIVITY MEASUREMENT AND ITS METHODOLOGY 11

2.1 Review on Electrical Resistivity and its Measurement Techniques 11

2.1.1 Biomedical applications 11

2.1.2 Power system grounding applications 17

2.2 Impact of Electrical Resistivity and its Measurement 23

2.2.1 Biomedical applications 23

2.2.2 Power system grounding applications 24

2.3 *In Situ* Resistivity Measurement Technique 26

2.3.1 Two-electrode method 26

2.3.2 Four-electrode method 27

2.4 Concluding Remarks 30

CHAPTER 3 - REVIEW OF THE SOLUTIONS OF THE LAPLACE'S EQUATION 31

3.1 Overview 31

3.2 The Laplace's Equation 31

3.3 The Relationship between the Cylindrical and the Spheroidal Coordinates Systems 34

3.4 Solutions of the Laplace's Equations 36

3.4.1 Cylindrical coordinates 36

3.4.2 Prolate spheroidal coordinates 39

3.4.3 Oblate spheroidal coordinates 44

3.5 Concluding Remarks 47

CHAPTER 4 - RESISTIVITY MEASUREMENT OF FINITE-VOLUME SAMPLES USING THE FOUR-ELECTRODE METHOD WITH CONSIDERATION OF THE FINITE DIMENSIONS OF THE ELECTRODES 48

4.1 Overview 48

4.2 The Theoretical Geometric Factor for Resistivity Measurement with Slender Cylindrical Electrodes Modelled using the Prolate Spheroidal Coordinates 53

4.2.1 Potential of a point 54

4.2.2 Potential of an electrode 55

4.2.3 Potential difference between electrodes *B* and *C* 57

4.2.4 Theoretical geometric factor for resistivity measurement using the four-electrode method in the prolate spheroidal coordinates 57

4.3 Numerical Simulations of the Derived Geometric Factor 58

4.4 Measurement System 60

4.4.1 Square wave generator 60

4.4.2 Current source unit 61

4.4.3 Voltage measurement unit 61

4.5 Experimental Set-Up 62

4.5.1 Saline solutions 63

4.5.2 Electrodes 65

4.6 Experimental Procedures 66

4.6.1 Effect of the frequency on the measured resistance 66

4.6.2 Effects of s, l_c and h on the measured resistance and the calculated resistivity 66

4.7 Experimental Results and Discussions 67

4.7.1 Shape of typical waveforms of V and V_{R_l} 67

4.7.2 Effect of the frequency on the measured resistance 68

4.7.3 Effects of s, l_c and h on the measured resistance and the calculated resistivity 69

4.8 Concluding Remarks 75

CHAPTER 5 - THE DETERMINATION OF THE PARAMETERS OF A TWO-LAYER MODEL BASED ON THE FOUR ELECTRODE RESISTIVITY MEASUREMENTS 76

5.1 Overview 76

5.2 Theory 78

5.3 Methodology 79

5.3.1 The Sunde's method 79

5.3.2 Determination of the resistivity of the first and second layers 80

5.3.3 Determination of the depth of the first layer 81

5.3.4 Procedure of the proposed method 82

5.4 Experimental Set-Up 82

5.4.1 Electrodes 83

5.4.2 Preparation of the agar and the saline solution 84

5.5 Results and Discussions 85

5.5.1 Measured parameters 85

5.5.2 Measured resistances 85

5.5.3 Estimation of the resistivities of the first and second layers 86

5.5.4 Estimation of the depth of the first layer using the Sunde's method 88

5.5.5 Short-coming of the Sunde's method 90

5.5.6 Point of inflection 92

5.5.7 Estimation of the depth of the first layer using the proposed method 92

5.6 Concluding Remarks 93

CHAPTER 6 - RESISTIVITY MEASUREMENT OF SMALL-VOLUME SAMPLES USING TWO SLENDER CYLINDRICAL ELECTRODES 94

6.1 Overview 94

6.2 Theoretical Derivation 97

6.2.1 Polarisation impedance 97

6.2.2 Relationship between the measured resistance, the electrical resistivity and the geometric factor in the cylindrical coordinates 100

6.2.2.1 Potential of a point 100

6.2.2.2 Potential of a point due to a current emanating from a slender cylindrical electrode 101

6.2.2.3 Self-potential 101

6.2.2.4 Mutual potential 102

6.2.2.5 Potential difference between electrodes *A* and *B* 103

6.2.2.6 The theoretical geometric factor 104

6.2.3 Relationship between the measured resistance, the electrical resistivity and the geometric factor in the prolate spheroidal coordinates 104

6.2.3.1 Potential of a point 105

6.2.3.2 Self-potential 105

6.2.3.3 Mutual potential 106

6.2.3.4 Overall potential 107

6.2.3.5 Potential difference between electrodes *A* and *B* 107

6.2.3.6 The theoretical geometric factor 107

6.3 Numerical Simulations of the Derived Geometric Factors 108

6.4 Experimental Set-Up 110

6.4.1 Saline solutions 111

6.4.2 Electrodes 111

6.5 Experimental Procedures 112

6.5.1 Effect of the frequency on the measured resistance 112

6.5.2 Effect of the current density on the geometric factors 112

6.5.3 Effect of the time on the measured resistance and the calculated resistivity 113

6.5.4 Effects of d, l_c and h on the calculated resistivity 113

6.5.5 Effect of the temperature on the calculated resistivity 113

6.6 Experimental Results and Discussions 114

6.6.1 Shape of typical waveforms of V and V_{R_l} 114

6.6.2 Effect of the frequency on the measured resistance 114

6.6.3 Effect of the current density on the geometric factors 116

6.6.4 Effect of the time on the measured resistance and the calculated resistivity 117

6.6.5 Effects of d, l_c and h on the calculated resistivity 119

6.6.6 Effect of the temperature on the calculated resistivity 121

6.7 Concluding Remarks 124

CHAPTER 7 - RESISTIVITY MEASUREMENT OF ULTRA-SMALL-VOLUME SAMPLES USING TWO PLANAR DISC ELECTRODES WITH A VIEW TO MICROFLUIDICS APPLICATIONS 125

7.1 Overview 125

7.2 Theory 127

7.2.1 Relationship between the measured resistance, the electrical resistivity and the geometric factor in the oblate spheroidal coordinates 128

7.2.1.1 Potential of a point 129

7.2.1.2 Self-potential 129

7.2.1.3 Mutual potential 130

7.2.1.4 Overall potential 130

7.2.1.5 Potential difference between electrodes A and B 131

7.2.1.6 The theoretical geometric factor 131

7.3 Experimental Set-Up 132

7.3.1 Saline solutions 133

7.3.2 Electrodes 133

7.4 Experimental Procedures 134

7.4.1 Effects of *d* and *h* on the calculated resistivity 135

7.5 Experimental Results and Discussion 135

7.5.1 Effects of *d* and *h* on the calculated resistivity 135

7.6 Concluding Remarks 138

CHAPTER 8 - EFFECTS OF THE SET-UPS ON RESISTIVITY MEASUREMENT OF FINITE-VOLUME SAMPLES USING BOTH THE FOUR AND THE TWO-ELECTRODE METHODS 139

8.1 Overview 139

8.2 Set-ups and Resistivity Calculations 141

8.2.1 The four-electrode method 141

8.2.1.1 Set-ups for resistivity measurement 141

8.2.1.2 Resistivity calculations 143

8.2.2 The two-electrode method 144

8.2.2.1 Set-ups for resistivity measurement 144

8.2.2.2 Resistivity calculations 145

8.3 Numerical Simulations on the Different Set-ups 146

8.4 Experimental Set-Up and Procedures 148

8.4.1 Saline solutions 149

8.4.2 Electrodes 149

8.4.3 Experimental procedures 150

8.5 Experimental Results and Discussion 150

8.5.1 Experimental results for the four-electrode method 150

8.5.2 Discussions for the four-electrode method 153

8.5.3 Experimental results for the two-electrode method 156

8.5.4 Discussions for the two-electrode method 159

8.6 Concluding Remarks 160

CHAPTER 9 - CONCLUSION AND RECOMMENDATION 161

9.1 Conclusion 161

9.2 Recommendations for Future Research Work 164

CANDIDATE'S PUBLICATIONS 166

BIBLIOGRAPHY 167

SUMMARY

The focus of this thesis is the theoretical and experimental study on some aspects of resistivity measurement of conductive media using both the four and the two-electrode methods. Theoretical derived novel geometric factors and new modelling techniques for biomedical and power system grounding applications were proposed and experimentally validated. The study of the resistivity measurement of biological tissue is of fundamental interest in the study and learning of the bioelectric phenomena. In addition, knowledge of the soil resistivity and the soil structure are of significant interest and importance in the design and analysis of an efficient grounding system.

First, a novel geometric factor, derived in the prolate spheroidal coordinates, for the *in situ* resistivity measurement of conductive media using the four-electrode method with slender cylindrical electrodes was proposed and validated through experiments. The evaluation of the experimental results showed that the saline resistivities that were obtained using a commercial conductivity meter and the proposed geometric factor were both in good agreement as the inter-electrode spacing or the length of immersed electrode was varied. In particular, a percentage error of less than 5% was achieved even when the length of the immersed electrode was comparable with or larger than the inter-electrode spacing, an improvement over the resistivities obtained using the geometric factors proposed by other researchers and currently available in the literature.

A new technique incorporating more accurate resistivity data for the determination of the parameters of a two-layer soil model is then reported. The evaluation of the experimental results showed that the depth of the first layer estimated using the proposed technique was more accurate than the depth estimated using the conventional Sunde's graphical method.

In an effort to address the issue of the resistivity obtained using the four-electrode method being affected when the sample volume is small, novel geometric factors were derived and presented for the resistivity measurement of both small and ultra-small-volume samples by means of the two-electrode method incorporating slender cylindrical electrodes and planar disc electrodes. The techniques to control and minimize the electrode polarisation impedance effect were also discussed. The evaluation of the experimental results showed that when the experiments were conducted at an excitation frequency of 3 kHz and nearly non-polarizable electrodes silver-silver chloride electrodes were used, the resistivities of the saline solutions determined using the derived geometric factors and a commercial conductivity meter were both in good agreement when the inter-electrode spacing, the length of the immersed electrode or the depth of the sample was varied. In the case of planar disc electrodes, the evaluation also showed that accurate resistivities were obtained even for small inter-electrode spacing and depth of the sample, therefore making the proposed two-electrode method a promising measurement technique for biomedical and microfluidic applications.

Lastly, as the large variation in the reported resistivities of the biological tissues has also been attributed to errors in the measurement set-ups by other researchers, the effects of the different set-ups on the resistivities of finite-volume samples determined using both the four and the two-electrode methods were investigated and reported. An experimental study was made to investigate the effects of different set-ups on the calculated resistivities of finite-volume samples, as the inter-electrode spacing or the length of the immersed electrodes was varied. The resistivities determined based on the different set-ups and those that were obtained using a commercial conductivity meter were then compared and evaluated. The set-ups, which are suitable for resistivity measurement under the above-mentioned circumstances, were then reported.

LIST OF FIGURES

Figure 2.1 - The two-electrode method for the *in situ* resistivity measurement of conductive media. 26

Figure 2.2 - The four-electrode method for the *in situ* resistivity measurement of conductive media. 28

Figure 3.1 - The relationship between the prolate spheroidal coordinates (η, δ, ϕ) and the cylindrical coordinates (r, ϕ, z). 34

Figure 3.2 - The relationship between the oblate spheroidal coordinates (η, δ, ϕ) and the cylindrical coordinates (r, ϕ, z). 35

Figure 3.3 - Point current source (r_s, z_s) inside the semi-infinite conductive medium.....36

Figure 4.1 - Four-electrode method for *in situ* resistivity measurement using slender cylindrical electrodes. 48

Figure 4.2 - Four-electrode method for *in situ* resistivity measurement using planar disc electrodes....49

Figure 4.3 - Current distribution of a current source electrode modelled in (a) the cylindrical coordinates and (b) the prolate spheroidal coordinates. 52

Figure 4.4 - Application of the image method for currents to the current source and sink electrodes *A* and *D*, respectively, with the electrodes modelled in the prolate spheroidal coordinates. 54

Figure 4.5 - Numerical values of the geometric factors as the inter-electrode spacing was varied from (a) 1 mm to 40 mm, and (b) 1 mm to 10 mm, with the number of segments used to compute the derived geometric factor $K_{4E,ps}$ in (4.14) set at 100.....59

Figure 4.6 - The oscilloscope (LeCroy model WaveSurfer 424).....62

Figure 4.7 - The measurement system for experiments using the four-electrode method with slender cylindrical electrodes. The current was injected into the electrode *A* while the electrode *D* was grounded. 62

Figure 4.8 - The commercial conductivity meter (YSI model EC300).....64

Figure 4.9 - The thermometer (Fluke model FLU65).....65

Figure 4.10 - The digimatic calliper (Mitutoyo model CD-6" CsX). 65

Figure 4.11 - Typical waveforms of V and V_{R_t} 67

Figure 4.12 - The plots of resistivity ρ for saline solution 4*X* as $s = 5\,mm$ and $2\,mm \le l_c \le 10\,mm$. The resistivities were obtained using a commercial conductivity meter and the geometric factors $K_{4E,pt}$, $K_{4E,cyl}$, and $K_{4E,ps}$ ...72

Figure 4.13 - The plots of resistivity ρ for saline solution 4*X* as $l_c = 5\,mm$ and $5\,mm \le s \le 30\,mm$. The resistivities were obtained using a commercial conductivity meter and the geometric factors $K_{4E,pt}$ and $K_{4E,ps}$. 73

Figure 4.14 - The plots of resistivity ρ for saline solution 4*X* as $l_c = 5\,mm$ and $10\,mm \le h \le 60\,mm$ for different s (s fixed at 5 mm, 10 mm, 20 mm, and 30 mm). The resistivities were obtained using a commercial conductivity meter and the geometric factor $K_{4E,ps}$ 73

Figure 5.1 - Four-electrode method for determination of the two-layer soil model. 78

Figure 5.2 - The experimental set-up. The upper layer was a saline solution with resistivity ρ_1, while the lower layer was agar with resistivity ρ_2. (Note: The figure was not drawn to scale). 83

Figure 5.3 - The plots of the measured apparent resistivity versus inter-electrode for experiments (a) 5*X*2 and (b) 5*Y*2.....88

Figure 5.4 - Sunde's curve for the case where ρ_2/ρ_1 was (a) 0.61 and (b) 2.08. 89

Figure 5.5 - The plots of measured and theoretical apparent resistivity versus inter-electrode spacing for experiments (a) 5*X*2 and (b) 5*Y*2. 91

Figure 6.1 - Two-electrode method for *in situ* resistivity measurement using slender cylindrical electrodes. 97

Figure 6.2 - Simplified equivalent circuit model. 98

Figure 6.3 - Application of the image method for currents to the current source and sink electrodes *A* and *B*, respectively, with the electrodes modelled in the cylindrical coordinates. 100

Figure 6.4 - Application of the image method for currents to the current source and sink electrodes *A* and *B*, respectively, with the electrodes modelled in the prolate spheroidal coordinates.....105

Figure 6.5 - Numerical values of the geometric factors as the inter-electrode spacing *d* was varied from 1 mm to 40 mm, with the number of segments *n* used to compute the derived geometric factor K_{ps} in (6.23) set at 10.....109

Figure 6.6 - The measurement system for experiments using the two-electrode method with slender cylindrical electrodes. The current was injected into the electrode *A* while the electrode *B* was grounded.....110

Figure 6.7 - Plot of measured resistance *R* versus frequency *f* for saline solution 6*X*. 116

Figure 6.8 - Plot of measured resistance R versus frequency f for saline solution $6Y$. 116

Figure 6.9 - Plot of resistivity versus temperature difference with respective to the lowest temperature measured $(21\,°C)$ for the saline solution $6X$.....123

Figure 6.10 - Plot of resistivity versus temperature difference with respective to the lowest temperature measured $(21\,°C)$ for the saline solution $6Y$.....123

Figure 7.1 - Two-electrode method for resistivity measurement using planar disc electrodes.....127

Figure 7.2 - Application of the image method for currents to the current source and sink electrodes A and B, respectively, with the electrodes modelled in the oblate spheroidal coordinates.....128

Figure 7.3 - The measurement system for experiments using the two-electrode method with planar disc electrodes. The current is injected into both electrodes A and B. 132

Figure 7.4 - Resistivity measurement of saline solution in an enlarged model of a microfluidic channel using two relatively non-polarizable planar disc electrodes.....137

Figure 8.1 - Conceptual representation for set-ups (a) C_1, C_3 and C_5 and (b) C_2, C_4 and C_6 for the four-electrode method. (Note: V_{cc} is the supply voltage).....141

Figure 8.2 - Conceptual representation for set-ups (a) C_1, C_3 and C_5 and (b) C_2, C_4 and C_6 for the two-electrode method. (Note: V_{cc} is the supply voltage). 144

Figure 8.3 - Plots of potential distribution simulated using the set-ups (a) C_1, (b) C_2, (c) C_4 and (d) C_6, for both the four and the two-electrode methods. For the two-electrode method, the text "Electrode D" is replaced by the text "Electrode B". 146

Figure 8.4 - Plot of the calculated resistivity using the four-electrode method as the inter-electrode spacing was varied for saline solutions (a) 8*X* and (b) 8*Y*. 151

Figure 8.5 - Plot of the calculated resistivity using the four-electrode method as the length of the immersed electrode was varied for saline solutions (a) 8*X* and (b) 8*Y*. 153

Figure 8.6 - Plot of the calculated resistivity using the two-electrode method as the inter-electrode spacing was varied for saline solutions (a) 8*X* and (b) 8*Y*. 157

Figure 8.7 - Plot of the calculated resistivity using the two-electrode method as the length of the immersed electrode was varied for saline solutions (a) 8*X* and (b) 8*Y*. 158

LIST OF TABLES

Table 4.I - Numerical values of the geometric factors for different inter-electrode spacing, immersed electrode length and number of segments. 58

Table 4.II - Measured resistances of saline solutions $4X$ and $4Y$ as the frequency was varied.....68

Table 4.III - Measured resistances and calculated resistivities of saline solution $4X$.....69

Table 4.IV - Measured resistances and calculated resistivities of saline solution $4Y$.....70

Table 4.V - Measured resistances and calculated resistivities of saline solution $4X$.....71

Table 4.VI - Measured resistances and calculated resistivities of saline solution $4Y$.....71

Table 5.I - Measured parameters for experiments $5X$ $(\rho_1 > \rho_2)$ and $5Y$ $(\rho_1 < \rho_2)$.....85

Table 5.II - Measured resistances R for experiments $5X$ $(\rho_1 > \rho_2)$ and $5Y$ $(\rho_1 < \rho_2)$ as the inter-electrode spacing is varied from 5 mm to 100 mm. 85

Table 5.III - Calculated resistivities $\rho_{a,pt}$ and $\rho_{a,ps}$ were calculated using (5.5) and (5.6), respectively, for experiments $5X$ $(\rho_1 > \rho_2)$ and $5Y$ $(\rho_1 < \rho_2)$.....86

Table 5.IV - Estimated resistivities of the first and second layer based on apparent resistivities calculated using (5.5) only. 87

Table 5.V - Estimated resistivities of the first and second layer based on apparent resistivities calculated using (5.6) only. 87

Table 5.VI - Effect of ρ_a/ρ_1 on estimated h for experiments $5X$ $(\rho_1 > \rho_2)$ and $5Y$ $(\rho_1 < \rho_2)$ using the Sunde's method. Measured h was 20 mm.....90

Table 5.VII - Inter-electrode spacing where the point of inflection occurred.....92

Table 5.VIII - Estimated h using the proposed method. Measured h was 20 mm.....92

Table 6.I - Numerical values of the geometric factors for different inter-electrode spacing, immersed electrode length and number of segments. 108

Table 6.II - Measured resistances of saline solutions 6*X* and 6*Y* as the frequency of the current source was varied. 115

Table 6.III - The theoretical and measured geometric factors as the current density *J* was varied for the saline solution 6*X*. 117

Table 6.IV - The theoretical and measured geometric factors as the current density *J* was varied for the saline solution 6*Y*. 117

Table 6.V - The measured resistance and calculated resistivity over a measurement period of 1 hour for the saline solution 6*X*. 118

Table 6.VI - The measured resistance and calculated resistivity over a measurement period of 1 hour for the saline solution 6*Y*. 118

Table 6.VII - The measured resistance and calculated resistivity as the inter-electrode spacing and the length of immersed electrode were varied for the saline solution 6*X*. 119

Table 6.VIII - The measured resistance and calculated resistivity as the inter-electrode spacing and the length of immersed electrode were varied for the saline solution 6*Y*. 120

Table 6.IX - The measured resistance and calculated resistivity as the depth of the saline solution 6*X* was varied. 120

Table 6.X - The measured resistance and calculated resistivity as the depth of the saline solution 6*Y* was varied. 121

Table 6.XI - The measured resistance and calculated resistivity as the temperature of the saline solution 6*X* was varied. 122

Table 6.XII - The measured resistance and calculated resistivity as the temperature of the saline solution 6*Y* was varied. 122

Table 7.I - The measured resistance and calculated resistivity as the inter-electrode spacing was varied for the saline solution 7*X*. 136

Table 7.II - The measured resistance and calculated resistivity as the inter-electrode spacing was varied for the saline solution 7*Y*. 136

Table 7.III - The measured resistance and calculated resistivity as the depth of the saline solution 7*X* was varied. 136

Table 7.IV - The measured resistance and calculated resistivity as the depth of the saline solution 7*Y* was varied. 137

Table 8.I – Possible set-ups for the four-electrode method. 141

Table 8.II – ossible set-ups for the two-electrode method. 144

Table 8.III - Calculated resistivities of saline solutions 8*X* and 8*Y* using the different set-ups as the inter-electrode spacing was varied. 151

Table 8.IV - Calculated resistivities of saline solutions 8*X* and 8*Y* using the different set-ups as the length of the immersed electrode was varied. 152

Table 8.V - Calculated resistivities of saline solutions 8*X* and 8*Y* using the different set-ups as the inter-electrode spacing was varied. 156

Table 8.VI - Calculated resistivities of saline solutions 8*X* and 8*Y* using the different set-ups as the length of the immersed electrode was varied. 158

CHAPTER 1 - INTRODUCTION

1.1 Motivation and Purpose

Information pertaining to the electrical resistivity of conductive media and its measurement has always captivated the human race. Researchers have always been interested in the interaction of electricity and biological substances [1] and also in the resistivity measurement of the soil pertaining to power system grounding applications.

The study of the electrical resistivity, or its inverse, the electrical conductivity measurement of biological tissue is of fundamental interest in the study and learning of the bioelectric phenomena [2], where the conductivity of a biomaterial is known to affect the electrical property of the biomaterial [3]. The resistivity measurement of the tissue is also an important diagnostic method in the analysis of the properties of the tissue by making use of the relationship between the electrical properties of the tissues and its biological or physiological parameters [4], for example, in the analysis of the characteristics of the myocardial, the information on the resistive properties of the myocardial are important [5-7]. Knowledge of the cardiac resistivity is also useful in the study of the heart [8]. The accurate computational model of the head is also dependent on the precise resistivities of the various tissues in the head [9]. Similarly, the resistivities of the different tissues are also important for the modelling of the human body [10] and the theoretical cochlear model [11]. In addition, with the significant difference in the electrical conductivity of a normal and a neoplastic or tumour tissue, information of the tissue conductivity can also be used to diagnostically differentiate between the normal and the neoplastic or tumour tissue [12] and for the detection of the tumour tissue of the liver [12] and the human breast [13]. In biomedical applications where all

the living tissues are enveloped by a dielectric membrane, of which the capacitance of the membrane is essential, the frequency of the current used to measure the resistivity is important. In addition, some cells are spherical; others are cylindrical. Low frequency current passes around the cell and high frequency current goes through the cell and around it as well [14].

With regards to the resistivity measurements in power system grounding applications, an accurate soil resistivity measurement is of vital importance in the design of the power system grounding [15] where the interpretations of the soil resistivity measurements are essential for the precise analysis of the grounding system [16]. In addition, the knowledge of the soil structure at a particular site is also an important requirement for the accurate analysis of grounding system performance [17], where the study of the grounding system is dependent of the parameters of the earth structure [18]. The soil structure can be determined from the investigations of the soil resistivity. Variations in soil resistivity have considerable influence on the performance of most grounding systems and it is of use to distinguish the soil structure, as the soil model derived is a good approximation of the actual soil. Two-layer soil models are frequently used as an approximation of many soil structures and are accepted as a representation of non-homogeneous soil for grounding system design [19, 20]. It is also important to know the actual soil structure at a particular site to prevent issues of over-design or under-design of the grounding system [19]. Therefore, it is apparent that the resistivity of the soil and the knowledge of the soil structure are of significant interest and importance in the design and analysis of an efficient grounding system.

For the *in situ* resistivity measurement of conductive media, an obvious and simple measurement technique is the two-electrode method [21], where the current is injected and the voltage difference is measured across the same pair of electrodes. However, resistivity measurement by means of the two-electrode method is known to be affected by the effect of

the electrode polarisation impedance [21-24]. Consequently, the two-electrode method has not produced accurate results for the resistivity of conductive media thus far. So as to avoid the electrode polarisation impedance effect, the *in situ* resistivity measurement of conductive media can be conducted using the four-electrode method [21], or known as the Wenner method, which was first proposed by Dr. Frank Wenner in 1916 [25]. In the four-electrode method, the current is injected and the voltage difference is measured across different pairs of electrodes. The four-electrode method has been extensively used for the soil resistivity measurements since its introduction and it remains one of the most commonly used technique for the measurement of the soil resistivity [19]. It is worthwhile to note that in power grounding applications, resistivity measurements are usually conducted for large or infinite volume samples.

More recently, the four-electrode method is also widely used for the resistivity measurement of the electrical resistivity or conductivity of the biological tissues [4, 12, 22, 26-31], where fixed or small-volume samples are often encountered. For resistivity measurement conducted using the four-electrode method, a number of different signals and measurement set-ups have been used in the past, such as: the waveform of the sources used; the method of storage of samples during the measurement process; and the type of measurement. Due to the differences in the set-ups and the types of tissue tested, there exists a wide variation in the published values of tissue resistivity. In two excellent reviews by Geddes, Gabriel and associates [32, 33], a comparison of the resistivities of the same kind of tissues reported also showed that there were significant dissimilarities between the reported resistivities. There were also considerable differences in the reported resistivities of the myocardial from different researchers [34]. In addition, the resistivity of the myocardial also varied between different positions in the heart and between different hearts [35]. It was also reported that a significant difference in the conductivity of the skull was observed from the samples obtained from the various parts of the human cadaver skull [36].

Although the four-electrode method has been widely used for the measurements of the resistivity of the soil and the biological tissue, there is much more to be learnt about the measurements being conducted on scale models in the laboratory. The reason is that the measurements of the resistivity using scale models in the laboratory can be conducted using different experimental set-ups. Moreover, the four-electrode *in situ* resistivity measurement is used historically in geophysical applications, where there are no limits on the sample volume, i.e., the sample volume can be assumed as semi-infinite. However, resistivity measurements for biomedical applications often involved finite-volume samples. In addition, small-volume samples are often encountered in resistivity measurements of biological tissues or biofluids. The challenge for the resistivity measurements of finite-volume samples has resulted in newer phenomena and discoveries.

It is also worthwhile to note that although the calibration of electrodes before any measurements can be used to obtain accurate resistivities from the measured data, the calibration is only valid for specific electrode geometry and configurations. However, in circumstances whereby the electrode geometry or the configuration is varied, i.e., when the inter-electrode spacing or the length of the immersed electrode is varied, the calibration of the electrodes is no longer applicable. The considerable differences in the literature on the measured resistivities of the tissues also indicated that there is much more to be learned from the resistivities of the biological tissues and its measurement techniques. The wide variations in the reported resistivities have been viewed from a measurement theoretical viewpoint and one of the factors is in the error in the measurement set-up and the method applied to calculate the resistivity from the actual measured data [2].

In view of the above, the study and the enhancement of the resistivity measurement technique for biomedical and power system grounding applications are important, where there are innumerable discoveries yet to be revealed in the resistivity measurements of conductive

media and on using the information pertaining to resistivity values as a research tool in different biomedical and power system grounding applications.

1.2 Objectives of Thesis

This thesis endeavours to propose theoretical derived novel geometric factors and modelling techniques for the theoretical and experimental study on some aspects of resistivity measurement of conductive media using both the four and the two-electrode methods. The theoretical derived geometric factors and new modelling techniques are proposed for biomedical and power system grounding applications at low excitation frequencies where the conductive current phenomena are more significant as compared to the displacement current. Consequently, the broadly classified objectives of the thesis are as follows:

(i) to propose a new geometric factor, derived using the prolate spheroidal coordinates, for *in situ* resistivity measurement of conductive media using the four-electrode method with slender cylindrical electrodes when the length of the immersed electrodes become long with respect to the inter-electrode spacing;

(ii) to propose a new technique incorporating more accurate resistivity data, which is an improvement to the conventional Sunde's graphical method, for the accurate determination of the parameters of a two-layer soil model;

(iii) to develop a new measurement technique for *in situ* resistivity measurement of small-volume samples of conductive media using two slender cylindrical electrodes with novel geometric factors derived in the prolate spheroidal and the cylindrical coordinates;

(iv) to propose a new measurement technique for resistivity measurement of ultra-small-volume samples of conductive media using two planar disc electrodes with a new geometric factor derived in the oblate spheroidal coordinates;

(v) to investigate the effects of the different set-ups on the measured resistivities of finite-volume samples obtained using both the four and the two-electrode methods.

1.3 Major Contributions of Thesis

The major contributions of this thesis are theoretical derived novel geometric factors for resistivity measurement of conductive media using both the four and the two-electrode methods and a new technique incorporating more accurate resistivity data for the determination of the parameters of a two-layer soil model. The derived novel geometric factors and the new technique were validated through experiments. In addition, the derived novel geometric factors remained applicable even when resistivity measurements are conducted in the circumstances where the electrode geometry or the configuration is varied.

First, the use of the four-electrode method for resistivity measurement in biomedical applications was studied. A new geometric factor for *in situ* resistivity measurement of conductive media using four slender cylindrical electrodes was derived using the prolate spheroidal coordinates, experimentally validated and reported in Chapter 4. Using the new derived geometric factor, accurate and consistent resistivities were obtained as the inter-electrode spacing or the length of the immersed electrode was varied. In particular, accurate and consistent resistivities were obtained even when the length of the immersed electrode became long with respect to the inter-electrode spacing, circumstances which are common in

biomedical experiments. This is an improvement over the resistivities that were obtained using the currently available geometric factors reported in the literature, namely, the geometric factors derived by Wenner [25] and Baishiki *et al.* [37].

Next, the use of the four-electrode resistivity measurement technique in power system grounding applications was studied. A new technique incorporating more accurate resistivity data, which is an improvement over the conventional Sunde's graphical method, for the determination of the parameters of a two-layer soil model was presented in Chapter 5. The proposed technique was experimentally validated and the results were presented in the chapter. More accurate two-layer models, which are characterised by the resistivities of the first and the second layer, as well as the depth of the first layer, were obtained using the proposed technique. The potential of the proposed technique in obtaining accurate information on the electrical properties of the soil is important for a good understanding of the composition of the soil structure, which is essential for the proper design and analysis of the performance of the power system grounding.

Subsequently, the use of the two-electrode method for resistivity measurement in biomedical applications was studied. A two-electrode method for *in situ* resistivity measurement of a conductive medium was proposed and presented in Chapter 6. Novel geometric factors for resistivity measurement of small-volume biological samples by means of two slender cylindrical electrodes were derived using the cylindrical and the prolate spheroidal coordinates, experimentally validated and reported in the chapter. The theoretically derived geometric factors were validated through the evaluation of the experimental results, which were discussed in the chapter. In addition, the effect of the electrode polarisation impedance, which had previously impeded the usage of the two-electrode method, and techniques to control and minimize the electrode polarisation impedance effect were meticulously discussed in the chapter. The evaluation of the experimental results showed that accurate resistivities

were obtained with the new geometric factors as the inter-electrode spacing, the length of the immersed electrode or the depth of sample was varied. Moreover, the evaluation also showed that the proposed technique was able to measure the resistivity accurately when the ratio of the inter-electrode spacing to the depth of the sample was 1:1, making it a promising measurement technique in biomedical applications where small-volume samples are often encountered. This is a significant improvement over the four-electrode method presented in Chapter 4, where the resistivity obtained using the four-electrode method was known to be affected by the small-volume sample.

In an extension to the resistivity measurement technique of small-volume samples using the two slender cylindrical electrodes presented in Chapter 6, the use of the two-electrode method for resistivity measurement in microfluidic applications was studied. A new geometric factor for the resistivity measurement of an ultra-small-volume sample of biofluids by means of two planar disc electrodes was derived using the oblate spheroidal coordinates, experimentally validated and reported in Chapter 7. The evaluation of the experimental results showed that accurate resistivities were obtained using the new geometric factor as the interelectrode spacing or the depth of sample was varied. In particular, using the derived geometric factor, accurate resistivity values were obtained even when the ratio of the inter-electrode spacing to the depth of the sample was 1:0.6, this ratio is an improvement over the ratio of 1:1 which was achieved using the resistivity measurement technique reported in Chapter 6. Consequently, the latest resistivity measurement technique reported in Chapter 7 is a promising resistivity measurement technique for applications in microfluidics devices.

Lastly, the use of both the four and the two-electrode methods for resistivity measurement in biomedical applications was studied. The effects of the different set-ups on the resistivities obtained using both the four and the two-electrode methods were meticulously studied and reported in Chapter 8. The effects of the different set-ups on the measured resistivities of

finite-volume samples obtained using both the four and the two-electrode methods as the inter-electrode spacing or the length of the immersed electrode was varied were studied. The set-ups that are suitable for resistivity measurement under the above-mentioned circumstances were reported. The knowledge of the set-ups to be used is important as resistivity measurement can be conducted under different experimental circumstances in the laboratory. Hence, it is prudent to know the proper set-ups for the accurate resistivity measurement under the different experimental circumstances.

1.4 Organisation of Thesis

This thesis is organised into nine chapters and the structure is as follows:

(i) Chapter 1 presents the introduction, encompassing the motivation and purpose of the thesis, the objectives, the major contributions and the organisation of the thesis.

(ii) Chapter 2 provides the detailed literature review of the subjects covered in this thesis. In particular, the fundamentals of the resistivity measurement, its methodology and the impact of the resistivity measurement in both the biomedical and the power grounding applications are discussed.

(iii) Chapter 3 reviews the solutions of the Laplace's equation in the cylindrical and the spheroidal coordinates. The derivations of the potential of a point inside a conductive medium that is induced by a current source located inside a slender cylindrical electrode and a planar disc electrode are reviewed and the derivations are utilised in the subsequent chapters in the thesis.

(iv) Chapter 4 presents a new geometric factor, derived in the prolate spheroidal coordinates, for the resistivity measurement of conductive media by means of four slender cylindrical electrodes. The effect of the relative size of the sample volume on the four-electrode resistivity measurement is also presented.

(v) Chapter 5 describes a new technique incorporating more accurate resistivity data to determine the parameters of a two-layer soil model. More accurate two-layer models, which are characterised by the resistivities of the first and the second layer, as well as the depth of the first layer, were obtained using the proposed technique.

(vi) Chapter 6 reports a new measurement technique for the resistivity measurement of small-volume samples by means of two slender cylindrical electrodes and novel geometric factors derived using the cylindrical and the prolate spheroidal coordinates.

(vii) Chapter 7 presents an extension to the measurement technique presented in Chapter 6 for application in ultra-small-volume samples, such as microfluidics devices. A new geometric factor, derived using the oblate spheroidal coordinates, for resistivity measurement using two planar disc electrodes is reported.

(viii) Chapter 8 reports the effects of the set-ups on the resistivity measurement of finite-volume samples using both the four and the two-electrode methods. The set-ups, which are suitable for resistivity measurement under the different laboratory circumstances, are reported.

(ix) Chapter 9 concludes the thesis and presents the recommendations for the future research work.

CHAPTER 2 - RESISTIVITY MEASUREMENT AND ITS METHODOLOGY

2.1 Review on Electrical Resistivity and its Measurement Techniques

2.1.1 Biomedical applications

Bioimpedance refers to the electrical properties of a biological tissue, measured when a current flows through it [38]. The electrical resistance of a tissue is a fundamental property in bioimpedance. Though the resistance of a sample is a fixed measure of the individual sample, it is also practical to be able to depict the general properties of the sample, which is the electrical resistivity, or its inverse, the electrical conductivity of a sample. The resistivity of a tissue is the ability of the tissue to oppose the flow of the electrical current for a defined unit of the tissue [38].

Numerous researchers have been interested in the measurement of the electrical resistivity of the biological tissues. The resistivities of the tissues at low excitation frequencies were studied by Rush *et al.* in 1963 [26]. Resistivity measurements of the tissues of the thorax of living anesthetised dogs were conducted using the four-electrode method [25] and the resistivities of the thorax and the arm of human subjects were also studied. The tissue resistivity values found are approximately 1.6 $\Omega \cdot$m for blood, 20 $\Omega \cdot$m for lung, 25 $\Omega \cdot$m for fat and 7 $\Omega \cdot$m for liver. Rush *et al.* also reported on the reasons behind the variations in the resistivities of various tissues. In 1967, Witsoe and Kinnen reported on the electrical resistivity of the lung at high excitation frequency [39]. *In vivo* four-electrode resistivity measurements on the surface of canine lung were conducted at an excitation frequency of 100

kHz and the resistivity of the lung was determined. Robillard and Poussart reported on the relative efficacy of the four-electrode resistivity measurement technique of the biological material in terms of its spatial resolution in 1979 [31]. From the four-electrode assembly buried in the medium, the apparent resistivities were obtained and analysed. The circumstances that must be fulfilled for an accurate measurement of the apparent resistivity were established. Results show that the four-electrode array where the current electrodes were adjacent to the potential electrodes resulted in the least responsiveness in the resistivity measurement to the neighbouring structures. In 1982, Plonsey and Barr reported on the conditions for applying the four-electrode method in obtaining the resistivity of the cardiac tissue [30]. It was shown that when the anisotropy ratios were the same, the four-electrode resistivity measurement technique can be utilised in the cardiac tissue. However, if the anisotropy ratios were not the same, the four-electrode method cannot be used in the conventional manner. The electrical conductivity of the skeletal muscle tissue was studied by Gielen and associates in 1984 [29]. Experimental results obtained from the *in vivo* measurements on the different muscles were reported and the results appeared to be either dependent or independent of the frequency depending on the inter-electrode spacing of the four-electrode method. There were also considerable differences in the experimental results obtained for the different muscle types.

In recent times, there have been continuous interests in the electrical resistivity of the biological tissues and its measurement. In 1993, Suesserman and Spelman reported on a four-electrode *in vivo* resistivity measurement system that measured the complex resistivity of the cochlear tissue in a non-destructive manner [40]. Steendijk and associates, in 1993-1994, researched on the measurement of the myocardial electrical resistivity using the four-electrode method [8, 22]. The four-electrode resistivity measurement technique was studied with particular interest in the establishment of the depth of the penetration attained using the four-electrode method and in the volume of an anisotropic sample in [22]. The experimental

results obtained by Steendijk *et al.* suggested that variations in the volume of the blood or the myocardial perfusion affected the resistivity of the myocardial. It was found that the difference between the apparent resistivity and the actual resistivity is less than 10% if the layer thickness is more than 1.95 times the inter-electrode spacing. In [8], the variations during the cardiac cycle of the electrical resistivity of the myocardial and the source frequency dependence of the electrical resistivity of the myocardial were established. The electrical resistivity was shown to decrease as the source frequency increased. It was reported in [8] that the mean longitudinal resistivity decreased from $3.13 \pm 0.49\ \Omega \cdot m$ at 5 kHz to $2.12 \pm 0.32\ \Omega \cdot m$ at 60 kHz and the mean transverse resistivity decreased from $4.87 \pm 0.49\ \Omega \cdot m$ at 5 kHz to $3.78 \pm 0.53\ \Omega \cdot m$ at 60 kHz. In 1996, Cheng *et al.*, used the four-electrode method with current of rectangular pulse and studied the relationship between the electrical conductivity and the peak current density and the relationship between the conductivity and the pulse rate in the pig skin dermis and the subcutaneous fat specimens [41]. The conductivities obtained for the pig dermis range from 0.27 S/m to 0.38 S/m, while the conductivities for the subcutaneous fat range from 0.045 S/m to 0.113 S/m. The experimental results obtained indicated that the conductivities of the pig skin dermis and the subcutaneous fat were anisotropic and were not dependent on the ranges of the current density and the pulse rate tested. Entcheva *et al.*, in 1997, studied the myocardium conductivity measurements obtained using the four-electrode method in [42]. An alternative position of the sensing electrodes for the measurements was suggested based on the sensitivity maps of the potential fields induced by the different conductivity tensors. Baumann and associates measured the electrical conductivities of human cerebrospinal fluids at both room and body temperatures in 1997 [43]. The body temperature conductivity was found to be 1.79 S/m whereas the room temperature conductivity was found to be 1.45 S/m. Experimental results showed the conductivity measured at the body temperature was higher than that measured at the room temperature in the range of the frequency tested.

Wang *et al.*, in 1998, investigated the accuracy of the resistivities of the tissues measured using the four-electrode method as the diameter of the electrode, the length of the electrode, the spacing between the electrodes and the sample volume were varied [27]. The measured longitudinal and transverse resistivities of the skeletal muscle of a pig vary from 2.15 $\Omega \cdot m$ to 6.57 $\Omega \cdot m$ and 2.34 $\Omega \cdot m$ to 17.45 $\Omega \cdot m$, respectively. The results obtained showed that the measured resistivities were strongly dependent on the geometric factors, in particular for anisotropic tissues. In 1998, Xie *et al.* studied the relationship between the flow velocity and the resistivity of the blood [44] and reported that the resistivity value of the blood was a fundamental measure that affected the results obtained using the various techniques pertaining to the study of the heart and circulation. The experimental results obtained showed that when the velocity of the flow of the blood was increasing, the resistivity of the blood decreased. The results showed that the resistivity of the blood changed by ± 1.1% when the velocity of the blood changed from 2.83 cm/s to 40 cm/s. When the velocity of the blood was lower than 2.83 cm/s, the change in the resistivity of the blood increased to 23%. In addition, the results showed that the resistivity of the blood was greatly affected by the acceleration and the deceleration of the blood flow. Recently, the conditions for which the equations derived by Rush *et al.* [26] were studied and the extents of their suitable usages were reported by Kun and Peura in 2000 [4]. Their studies indicated that the resistivities of the tissues measured using the four-electrode method were affected by both the configurations of the electrodes and the geometry of the sample. The longitudinal and transverse resistivities of the muscle obtained from the experimental results were 1.75 $\Omega \cdot m$ and 7 $\Omega \cdot m$, respectively. The results also showed that the measured resistivity was affected by the sizes of the samples and the measured resistivity increased when the ratio of the inter-electrode spacing over the tissue thickness decreased as the electrodes were aligned longitudinally. From 2000 to 2002, the electrical conductivities of the human skulls were studied by Akhtari *et al.* [36, 45]. The electrical conductivities were obtained at the room temperature as the electric fields were varied using the four-electrode method. The results showed that the conductivities of the

various tissues of the skull were considerably different and inhomogeneous. The conductivities of the spongiform and the two compact layers of the skull vary from 0.76 ± 0.14 mS/m to 11.5 ± 1.8 mS/m.

In a series of studies from 2000 to 2002, Tsai and associates studied on the dependence of the apparent resistance obtained using the four-electrode method with the length of the immersed electrode [28], the error analysis of the measurement of the tissue resistivity [46] and the resistivity measurement of the swine myocardial [47]. Experimental results obtained in [28] showed that the apparent resistance decreased with increasing length of the immersed electrode, whereby this knowledge was critical for the accurate *in vivo* and *in vitro* resistivity measurement of the myocardial. In addition, the measured resistivity of the myocardial and the in-chamber blood ranges from about 1.5 Ω·m to 5.6 Ω·m and 1 Ω·m to 2 Ω·m, respectively. The sources of error in a resistivity measurement system using the four-electrode method were determined in [46]. Using a theoretical derived formula, the measured resistivity was expressed with considerations of all the error terms. The resistivities of the myocardial of pigs were determined using the four-electrode method with plunge probes. Experimental results obtained in [47] showed that the mean of the measured resistivities decreased from 3.19 Ω·m to 1.66 Ω·m as the frequency increased from 1 Hz to 1 MHz. In addition, there were also considerable differences in the measured resistivities of the different pigs, although there were no significant differences in the resistivity measured at the different sites on the pig. In 2003, Haemmerich *et al.* measured and determined the conductivities of the hepatic tumour and the normal tissues of rats [12] using the four-electrode method with plunge electrodes. Measurements were conducted from 10 Hz to 1 MHz and the measured conductivities of the normal liver tissue range from 1.26 ± 0.15 mS/cm to 4.61 ± 0.42 mS/cm, respectively. The measured conductivities of the tumour tissues range from 2.69 ± 0.91 mS/cm to 5.23 ± 0.82 mS/cm, respectively. The experimental results showed that the conductivity of the normal tissue was considerably different from that of the tumour tissue.

The difference in the conductivity was attributed to the necrosis inside the tumour and the related membrane breakdown. The frequency range for the greatest sensitivity in differentiating the normal and malignant tissues was also specified to be below 1 kHz. By means of the divided electrodes, Zhao and associates in 2004, described a novel method for the measurements of the conductivity and the structure of multilayer tissue [48]. In the proposed new method, the current electrodes were separated into numerous elements. The distribution of the conductivity in a two-dimensional model was studied based on the steepest descent and the finite difference methods. In addition, estimations of the distribution of the conductivity and the structure of the tissue were obtained concurrently by increasing the number of the divided electrodes.

At this juncture, it is worthwhile to note that numerous researchers have been conducting measurements using saline solutions in various biomedical experiments, where the resistivities of the saline solutions were chosen to approximate that of biological tissues. In addition, the measuring systems used for the biomedical experiments were also often calibrated using saline solutions with known resistivities. In 1991, Fuks and associates, in their study on the detection and imaging of the resistivity of a body's interior at low frequency, presented experimental results obtained using a measuring system on various objects contained in a saline bath with resistivity of 3 $\Omega \cdot m$. [49]. In the measurement system used by Steendijk *et al.* in their research on the four-electrode measurement technique on myocardial tissue in 1993 [22], the measurement system was calibrated using the saline solutions with known resistivities in the expected range of those of myocardial tissues. In 1993, Suesserman and Spelman conducted measurements with the electrodes located in the center of a 0.9% saline solution filled beaker [40] in their study of an *in vivo* resistivity measurement system that measured the complex resistivities of cochlear tissues. In 1998, Newell *et al.* researched on the sensitivity of an impedance imaging system to the small cylindrical in-homogeneities placed in the tanks containing saline solutions with a

conductivity of 300 mS/m [50]. In 1999, Mueller and associates, in their study to establish the distribution of the conductivity under the surface of a medium [51], presented experimental results which were obtained using a measurement system in a rectangular tank filled with saline solution with a conductivity of 300 mS/m. The saline solution and the agar conductivities were chosen to approximate that of healthy breast tissue and tumour, respectively. The conductivity of the electrode-sized agar target is 900 mS/m. In a series of studies by Tsai and associates from 2000 to 2002, measurements were conducted on a physical model that consisted of air, saline solution and agar, which replicated the actual resistivity measurement [28]. Measurements were also conducted on reference saline solutions with resistivities ranging from 1 $\Omega \cdot$m to 5 $\Omega \cdot$m in the study of the error analysis of the measurement of the resistivity of the tissue [46]. In addition, the probe for the *in vivo* measurement of the resistivity of the swine myocardial was calibrated in saline solutions contained in a metal cup located near the heart [47]. Haemmerich *et al.* calibrated their measurement setup using the 0.9% saline solution, in their study of the *in vivo* electrical conductivity of the hepatic tumours in 2003 [12].

2.1.2 Power system grounding applications

A prominent individual who contributed to the field of the resistivity measurement of the soil in 1912 was Wenner, who was considered the father of the modern quantitative resistivity techniques [52]. Wenner made two significant contributions to the field of the resistivity measurement of the soil. Firstly, Wenner gave a clear statement of the reciprocity theorem applicable to his four-electrode measurement, where he noted that in any conductor systems having four terminals, the potential drop between the first and the second electrodes as induced by a current flow between the third and the fourth electrodes is the same as the potential drop between the third and the fourth electrodes as induced by a current flow

between the first and the second electrodes. Secondly, Wenner developed the Wenner configuration of electrodes for his four-electrode measurement method in 1915. Wenner placed four electrodes in a straight line, with equal inter-electrode spacing, on the ground. The current was injected into the ground through the two outer electrodes and the potential difference between the two inner electrodes was then measured. In an effort to overcome the polarisation effect associated with the use of the direct current with the metal electrodes, Wenner used alternating current for his measurements. From the geometry of the electrode configuration and the measured resistance, the apparent resistivity was calculated. Wenner noted that the measured apparent resistivity depended primarily on the resistivity near and between the inner potential electrodes. Wenner also reported that by positioning the electrodes on the surface of the ground far apart, it was possible to measure the resistivities to a much greater depth. In addition, the resistivities at the different depths of the ground can also be estimated from the resistivity measurements.

A comprehensive review on the development of the resistivity measurement of the soil was written by van Nostrand and Cook [52]. In 1924, Gish studied the resistivity measurements of the ground using the Wenner configuration [53]. The inter-electrode spacing was varied regularly and vertical resistivity profiles were taken. Gish noted that there were oblivious lateral and depth variations in the vertical profiles. Rooney and Gish then reported the changes in the resistivity with the changes in the strata from their resistivity measurement of large volumes of the ground in 1925 [54]. Pertaining to a two-layer situation, they noted that when the boundary between two layers of earth was approximately horizontal and that there was a sudden change in the resistivity at a particular depth, from a series of resistivity measurements conducted using different inter-electrode spacing, a set of equations as a function of the unknown resistivities and the inter-electrode spacing can be established. Solving the equations empirically will then determine the absolute resistivity values. In 1927, Rooney hypothesised that a significant discontinuity in the slope of the apparent resistivity

curve occurred at an inter-electrode spacing approximately which is equal to the depth of the horizontal geological feature that caused the discontinuity in the slope [55]. Lee, in 1928, measured the earth resistivity and studied the depth attainable using the Wenner configuration [56]. In 1931, Swartz conducted experiments on the resistivity of artificial beds, where he dug a hole in the ground and filled it with alternating layers of clay and sand [57]. Using the Wenner configuration with direct current and non-polarising electrodes, Swartz obtained the vertical resistivity profile of the different layers of the clay and the sand.

The interpretation of the resistivity data are based on the Laplace's equation, as developed by Maxwell, where he specified the mathematical analysis involved in a layered-earth problem [58]. Neumann, in 1887, derived the equation for the potential at any point in the ground induced by the current flowing between two current electrodes located on the surface of the ground [52]. Expressions comparable to the derived equation by Neumann were then used by Wenner to derive the equations used to determine the apparent resistivity using the Wenner configuration. Although Maxwell developed the mathematical analysis involved in the problem of the layered earth in 1891, the major development of this issue only happened in the late 1920s [52]. Hummel derived formulas for the two-layer earth using the image theory in 1929 [59]. Hummel also provided a table which allowed the computation of the formulas for the two-layer earth and presented several sample curves obtained using the Wenner configuration. In addition, Hummel noted that with regards to a two-layer case, a lower bed of higher conductivity can be detected easier than a lower bed of lower conductivity. Hummel reported as well that the plot of the apparent resistivity curve versus the inter-electrode spacing was asymptotic to a straight line when the lower layer was perfectly insulating. Stefanesco, Schlumberger and Schlumberger, in 1930, solved the problem of the distribution of the potential inside the ground which comprised of homogeneous and isotropic horizontal layers [60]. Lancaster-Jones, in a completely independent study in 1930, conducted experiments similar to that conducted by Hummel and reached many conclusions of Hummel

[61]. Lancaster-Jones noted that the effect of the buried layers was apparent for small inter-electrode spacing. Lancaster-Jones also concluded that the empirical rule by Gish and Rooney that for a Wenner configuration, the depth of the penetration equals the inter-electrode spacing should be taken as just a rough estimation. In 1930, Tagg presented a graphical method for the determination of the depth [62]. Ehrenburg and Watson applied the image theory to a multi-layer problem and provided numerical calculations and theoretical curves for two-layer cases in 1931 [63]. A detailed study on the apparent resistivity for a two-layered earth was also made by Roman (a key supporter of the curve-matching method) in 1931, where the image theory was used to determine the potential induced by a current electrode located on the surface of the two-layer earth [64]. Roman presented a table for the calculation of the theoretical apparent resistivity for a two-layered earth when the Wenner configuration was used with any inter-electrode spacing. In 1934, Roman also presented theoretical apparent resistivity curves which were based on the table [65]. In addition, Roman's solution for the two-layer problem was the first acceptable image analysis of the problem of the determination of the depth [52]. Pekeris, in 1940, by means of a technique that used the transformation theory to determine the resistivities directly from the observed potentials on the surface of the ground, obtained the variation of the resistivity with the depth for a ground with horizontal layers [66]. In 1947, Maillet defined the relationship between the apparent resistivity as a function of the inter-electrode spacing and the relationship between the resistivity of the ground as a function of the depth [67].

Over the past 50 years, there have been continuous interests in the measurement and the application of the resistivity of the soil. Blattner, in 1982, investigated the apparent soil resistivity measured using the four-electrode method [68]. Measurements were conducted for both uniform and non-uniform soil conditions. Blattner derived an expression for the calculation of the apparent soil resistivity of the two-layer soil condition based on the Wenner configuration. The actual measurement results were also studied based on the theoretical

consideration of the two-layer model. In addition, Blattner reported on the possible limitations of the resistivity measurement technique using the Wenner configuration. Blattner, in 1985, also conducted a comprehensive study of the performance of the Wenner method in the resistivity measurement of the soil in a two-layer earth [17]. In 1986, Meliopoulos and Papalexopoulos, by means of a computational program, studied the interpretation of the resistivity measurement of the soil [69]. A model, which was based on the statistical estimation of the parameters of the soil from the Wenner measurements, for the interpretation of the measurements of the soil resistivity was presented. The model also specified the best estimation of the parameters of the soil and the error bounds versus the confidence level. A comparison of the effectiveness of eight different techniques to determine the resistivities and the thickness of a two-layered earth which corresponded to a particular mathematical model was studied by del Alamo in 1993 [70]. An optimum fitting between the set of the resistivities measured in the field using the Wenner method and those calculated from the mathematical model was obtained from the estimation of the electrical grounding parameters of the two-layered earth.

The most difficult part of the soil resistivity measurement program is perhaps to interpret the apparent resistivity acquired. The fundamental objective is to derive the soil model, although it must be recognised that the soil model is only an approximation of the actual soil and that a perfect match is unlikely. The most commonly used soil resistivity models are the uniform soil model and the two-layer soil model [19]. Two-layer soil models are frequently used as an approximation of many soil structures and is in general an acceptable representation of non-homogeneous soil for grounding system design [19, 71, 72]. A uniform soil model should be used only when there is a modest variation in apparent resistivity. If there is a large variation in measured apparent resistivity, the uniform soil model is not likely to generate accurate results. A more accurate illustration of the actual soil conditions can then be obtained by use of a two-layer soil model [19]. The two-layer soil model consists of a first layer soil of finite

depth and with different resistivity value than a second layer soil of infinite thickness. In some cases, a two-layer soil model can be approximated by visual examination of a plot of apparent resistivity versus depth from driven rod measurements or apparent resistivity versus probe spacing from measurements obtained using the Wenner method.

Analogous to the use of the saline solutions in biomedical experiments, scale model experiments pertaining to grounding applications were also conducted using the saline solutions. As stated in the IEEE Std. 80 [19], scale model tests have been shown to be effective for studies pertaining to the power system grounding applications. It was also reported in the IEEE Std. 81 [20] that one of the recommended materials for a scale model test is to use an electrolytic tank. So as to replicate the actual measurement of the soil in the field, electrodes were either immersed solely on the upper layer of the two-layer soil model, or immersed into the lower layer of the model. A solid medium is inconvenient both from the measurement point of view and when there is a need to change the electrodes. The obvious alternative is to use an electrolytic tank. The saline solution is also a convenient choice for modelling a homogeneous medium. In a review of the design and the use of scale models for the assessment of the effectiveness of the grounding grids presented by Caldecott and Kasten in 1983 [73], it was stated that the method of the use of scale models in an electrolytic tank to obtain the distribution of the surface potential was proposed by Koch in 1950 and Armstrong in 1953. Caldecott and Kasten concluded in their report that scale models can be effectively used in the parametric studies of the design of the grounding grids. In 1984, Caldecott and associates reported the experimental results of a study of the interpretation techniques for the measurement of the soil resistivity [74]. A variety of two-layer soil models in an electrolytic tank were used for the measurements. The lower layer was made of agar and the upper layer was a mixture of tap water and dissolved sodium chloride. Caldecott *et al.* concluded that when proper measurement parameters were met, the soil structure can be determined.

2.2 Impact of Electrical Resistivity and its Measurement

2.2.1 Biomedical applications

As mentioned earlier, researchers have always been interested in the electrical resistivity or the conductivities measurement of biological tissues [27]. Knowledge pertaining to the resistivity of various tissues is of basic concern in the study of bioelectric phenomena [2] and have been utilised in various biomedical applications. One of the factors that influenced the electrical property of biomaterial is the conductivity of the biomaterial [3]. With the knowledge of the connection between the electrical properties of the tissues and its biological or physiological parameters, the measurement of the resistivity of the tissue became a key diagnostic method for the non-invasive assessment of the characteristics of the tissues [4].

The resistive properties of the myocardial were often significant in the study of the myocardial behaviour [5-7]. In addition, information pertaining to the resistivity of the cardiac was also important for the understanding of the electrical properties of the heart [8]. The accurate resistivities of the different tissues within the head made an important contribution to the proper computational model of the head [9]. Information on the resistivities of the tissues was also necessary for the modelling of the human body [10] and the theoretical cochlear model [11]. The current flow in the tissues was dependent on the resistivities of the tissues and the resistivities were also associated with the electrophysiological measurements [75]. A precise resistivity of the blood was needed to establish the blood vessel's cross-sectional area when the impedance method was used [44]. The correctness of the measurement of the blood vessel's cross-sectional area was also dependent on the specific measurement of the blood's resistivity. It was reported in [41] that knowledge of the conductivity of the skin was required for the usage of a model which uses rectangular pulsed electrical current stimulation to enhance the healing of the skin wound. Information pertaining to the conductivity of the skin

was critical as the amounts of current that penetrated the subcutaneous fat and the skin can be estimated from the knowledge of the conductivity of the skin [41].

As there is a considerable difference in the conductivity of a normal and a neoplastic or tumour tissue, information regarding the electrical conductivity of the tissue was also utilised to diagnostically distinguish between the normal and the neoplastic or tumour tissue [12], where it was reported that the conductivities of the normal liver tissue range from 1.26 ± 0.15 mS/cm to 4.61 ± 0.42 mS/cm, whereas that of the tumour tissues range from 2.69 ± 0.91 mS/cm to 5.23 ± 0.82 mS/cm when measurements were conducted from 10 Hz to 1 MHz. From the conductivity values obtained using bioimpedance measurement, the detection of the tumour tissue was achievable with comparison of the conductivities of the normal liver parenchyma and the neoplastic tissue. In a review of the electrical impedances techniques for the detection of the breast cancer by Zou [76], it was reported that malignant tumours of the human breast tissues generally had higher conductivity values as compared to the normal human breast tissue [13]. Information pertaining to the conductivities of the normal and the tumour tissues became important as the distribution of the electromagnetic energy being absorbed was a factor of the ratios of the electrical conductivity between the normal and the tumour tissues [12].

2.2.2 Power system grounding applications

Researchers have also always been interested in the resistivity measurement of the soil. Information pertaining to the soil resistivity is a fundamental and important consideration in various aspects with regards to grounding applications. For the precise analysis of the grounding system performance, it is important to have knowledge with regards to the accurate measurement of the apparent soil resistivity and the knowledge of the soil structure.

The design of the grounding system is dependent on a precise estimate of the parameters of the soil [77]. At the preliminary phase of the grounding design, it is essential to determine the parameters of the soil where the grounding is going to be installed. The parameters of the soil must always be estimated based on the soil resistivity measurements [70]. Soil resistivity measurements and interpretations are crucial tasks for the precise analysis of the grounding system [16] as the value of the soil resistivity has a direct impact and significantly influenced the value of the grounding resistance [19]. Therefore, the precise measurement of the soil resistivity have a substantial impact on the grid design [19] and is of paramount importance in the design of the power system grounding design [15] and the subsequent study of the effectiveness of the grounding design [78].

In addition, knowledge of the soil structure at a particular site is an important requirement for the precise investigation of the performance of the grounding system [17], where the study of the grounding system is dependent of the parameters of the earth structure [18]. The design of complex grounding system has to be based on the measured resistivity data as the soil structure significantly influences the effectiveness of the grounding electrodes [79]. Resistivity investigations are required to determine both the soil structure and the extent of homogeneity. Taking measurements on the surface of the soil and taking note of the behaviour in which the resistivity values changes can provide useful information on the nature of the sub-soil. Variations in soil resistivity have considerable influence on the performance of most grounding systems and it is of use to distinguish the soil structure, as the soil model derived is a good approximation of the actual soil. It is also important to know the soil structure at a particular site to prevent issues of over-design or under-design of the grounding system [19]. Two-layer soil models are frequently used as an approximation of many soil structures and are accepted as a representation of non-homogeneous soil for grounding system design [19, 20]. In general, for a two-layer soil model with the top layer of soil more resistive

than the lower layer, the resistance determined would be less than that of the same grounding system modelled in uniform soil model. This would imply an over-design of the grounding system designed in a uniform soil model, which is not cost-effective. On the other hand, for a two-layer soil model with the top layer of soil less resistive than the lower layer, the resistance determined would be more than that of the same grounding system modelled in uniform soil model. This would result in under-design of the grounding system designed in a uniform soil model, which have serious complications, as it involves the issue of safety.

2.3 *In Situ* Resistivity Measurement Technique

2.3.1 Two-electrode method

The two-electrode method, which is shown in Fig. 2.1, is said to be the most easy and simple technique for the measurement of the biological system [22]. In addition, the two-electrode method is described as a 'clear-cut' measurement technique of the soil resistivity [80]. The two-electrode method is an appropriate measurement technique for the determination of the electrical properties of the materials provided that the potential measured between the electrodes *A* and *B* is a reasonable approximation to the potential between the medium that is being measured [81].

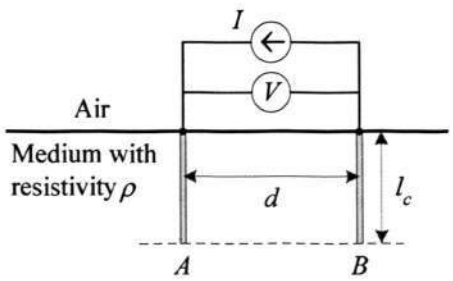

Figure 2.1 - The two-electrode method for the *in situ* resistivity measurement of conductive media.

In the two-electrode method, the electric current I is injected to the medium through the two outer electrodes A and B. The induced potential difference V between the same pair of electrodes is then measured. Although the two-electrode method is a simple and obvious method for the *in situ* resistivity measurement of the conductive media, the two-electrode method has not produced accurate results for the resistivity of conductive media thus far. The two-electrode method was reported to be inefficient because the measurement results were affected by the effect of the frequency dependent electrode polarisation impedance [21-24], where the measured impedance consisted of the combination of the sample impedance and the electrode polarisation impedance. The electrode polarisation impedance, or known as the contact impedance, occurs when the potential is measured on the current flowing electrodes [82]. The potential that is measured between the two electrodes A and B consists of the potential induced by the current that flowed through the electrode polarisation impedance at the interface of the electrode-medium interface and this affected the accuracy of the measurement results obtained using the two-electrode method [28].

2.3.2 Four-electrode method

As noted in the discussions, the two-electrode method for the *in situ* resistivity measurement of conductive media has been hindered by the effect of the electrode polarisation impedance. One of the techniques to overcome the electrode polarisation impedance effect is to conduct the resistivity measurement using the four-electrode method proposed by Wenner [25], as shown in Fig. 2.2. In the four-electrode method, the electric current I is injected to the medium through the two outer electrodes A and D. The induced potential difference V between the two inner electrodes B and C is then measured. By using separate pairs of electrodes for the flow of excitation current and voltage sensing, the problems associated with

the effect of the electrode polarisation impedance at the current source and sink electrodes can be effectively eliminated [3, 12, 21-23, 27, 28, 30, 47, 81-86].

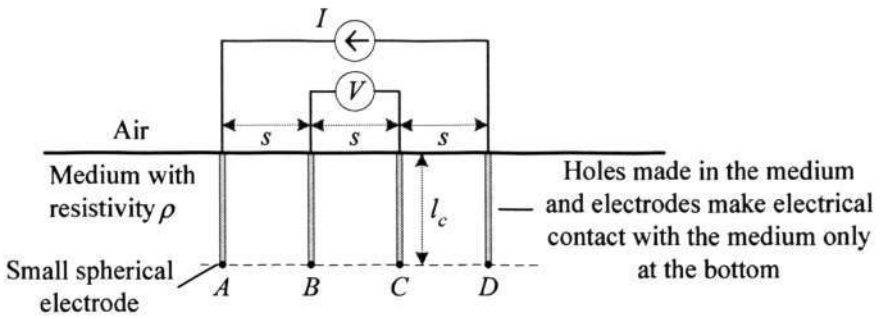

Figure 2.2 - The four-electrode method for the *in situ* resistivity measurement of conductive media.

Experiments pertaining to biomedical and power system grounding applications are commonly conducted using measurement techniques based on the four-electrode method proposed by Wenner [25]. In the four-electrode method, an array of four electrodes with the same inter-electrode spacing, denoted by s, is arranged in a straight line. Four holes, of approximately the same depth, are made in the medium to be tested and the diameter of the holes is smaller than 10% of the s [87]. An electrode is then positioned in each hole, and the electrodes made electrical contact with the medium only at the bottom. The electrodes are assumed to be small spherical electrodes.

In the four-electrode method, the values of the injected I, the measured V and the spacing s are utilised to obtain the measured resistivity of the medium. For resistivity measurement using the four-electrode method, when the medium is not homogeneous, the measured resistivity was not the actual resistivity of the medium. Instead, what was being measured was the apparent resistivity of the medium. Generally, the penetration depth of the current flow is larger with a larger s [52, 80, 88-92]. Resistivity surveys in the field can be carried out using two techniques, namely the electrical sounding and the electrical profiling [93]. The electrical sounding process was conducted as measurements are carried out with the center location of

the four-electrode configuration remained at the same position but with s increased successively. Consequently, the apparent resistivity is determined as a function of the effective depth of the penetration. The electrical profiling process was conducted as measurements are carried out with the electrode array moving about an area with the arrangement of the array and the s remained constant. The electrical profiling process determines the variation of the apparent resistivity over the area. The combination of the measurement results obtained from both the process of the electrical sounding and profiling can be used to obtain a three-dimensional representation of the resistivity of the medium.

The potential fields in the medium, and consequently, the flow of the current through the medium were affected by a few parameters, namely the different thickness and resistivities of the different layers in the medium, and the inter-electrode spacing at which the measurements were taken [94]. At the interface between the different layers of the medium, the different resistivities of the different layers influenced the flow of the current as it flowed between the interfaces of the different layers. The amount of current that flowed through the different layers of the medium depended on the reflection coefficient between the different layers. More current will flow into the medium if the resistivity of the medium is relatively low; on the contrary, less current will flow into the medium if the resistivity of the medium is relatively high. As the penetration depth of the current flow is larger with a larger s, more current will flow through the lower layers of the medium as s is increased. Consequently, the measured apparent resistivity is more affected by the resistivities of the lower layers of the medium as s is increased.

Although experiments are commonly conducted using measurement techniques based on the four-electrode configuration, the resistivity measured using the four-electrode method was known to be affected by the electrode geometry [27] and the sample size [4], in particular for biomedical applications where both fixed and small-volume samples are often encountered.

The measured resistivities were reported to be considerably influenced by the geometry of the electrode in [27]. It was also noted that the measured resistivity increased when the sample size became smaller in [4]. In addition, when there was a decrease in the ratio of the inter-electrode spacing with respect to the thickness of the tissue, there was an increase in the measured resistivity of the tissue [4].

2.4 Concluding Remarks

This chapter presents a comprehensive review on the pioneering works on resistivity measurement and its impact on the study and learning of the bioelectric phenomena and the power system grounding. In addition, the fundamental methodology of the resistivity measurement technique were also discussed in details - these form the groundwork for further research work which will be presented in the subsequent sections in this thesis.

CHAPTER 3 - REVIEW OF THE SOLUTIONS OF THE LAPLACE'S EQUATION

3.1 Overview

In this chapter, the work of the solutions of the Laplace's equation available in the literature is reviewed. Theoretical novel geometric factors for the resistivity measurement of the conductive media using both the four and the two-electrode methods are derived and presented in the subsequent chapters. However, before the theoretical novel geometric factors are derived, it is prudent to first comprehend the concept in deriving the electric potential, which is denoted by V, of a point in a conductive medium in the presence of a current source and the boundary. Once the expression of V has been derived, it can be utilised in the derivations of the theoretical novel geometric factors presented in the subsequent chapters.

3.2 The Laplace's Equation

The Laplace's equation is one of the most significant partial differential equations in the application of the mathematics to the physical phenomena and it occurs in many branches of learning, including electrostatics [95]. The derivation of the Laplace's equation is described below. Consider a continuous current I flowing in a homogeneous isotropic medium. The current passing through an element of the surface, denoted by $\delta\vec{A}$, can be expressed as [91]:

$$I = \vec{J} \cdot \delta\vec{A} \tag{3.1}$$

where $\vec{J}$ is the current density.

The electric field, denoted by $\vec{E}$, and $\vec{J}$ are related through the Ohm's law and expressed as:

$$\vec{J} = \sigma \vec{E} \tag{3.2}$$

where σ is the conductivity of the medium.

The electric field $\vec{E}$ is described as the gradient of a scalar potential and can be expressed as:

$$\vec{E} = -\nabla V . \tag{3.3}$$

Consequently, substituting (3.3) into (3.2), the $\vec{J}$ can be expressed as:

$$\vec{J} = -\sigma \nabla V . \tag{3.4}$$

If the charge is conserved within a volume enclosed by a surface $\overrightarrow{A_s}$, then:

$$\int_{A_s} \vec{J} \cdot d\overrightarrow{A_s} = 0 . \tag{3.5}$$

From (3.5) and the Gauss' Theorem, the volume integral of the divergence of the current throughout a given region is equal to the total charge enclosed, hence:

$$\int_{V} \nabla \cdot \vec{J} d\vec{V} = 0 . \tag{3.6}$$

From (3.4) and (3.6), $\nabla \cdot \vec{J} = -\nabla \cdot \nabla(\sigma V) = 0$, thus:

$$\nabla \sigma \cdot \nabla V + \sigma \nabla^2 V = 0 . \tag{3.7}$$

If σ is constant throughout, $\nabla \sigma = 0$. Therefore (3.7) became the Laplace's equation, which is expressed as:

$$\nabla^2 V = 0 \tag{3.8}$$

The potential V at any point in the conductive medium satisfied the Laplace's equation $\nabla^2 V = 0$ [96]. Therefore, the V at all points in a semi-infinite conductive, homogeneous and isotropic medium, which is due to a steady or direct current that enters the medium at the surface, is determined by solving for V in the Laplace's equation and applying the appropriate boundary conditions. Such boundary conditions included either the known potential on the surface of the metallic conductor or the potential behaviour at regions in infinity [95].

The above analysis is also applicable using an alternating current if the frequency is low enough such that displacement currents are insignificant [91]. In the bioelectric problems, the V can be assumed quasistatic, i.e., the capacitive and inductive effects and the finite speed of propagation of the electromagnetic radiation can be ignored. This assumption is valid for frequencies below 100 kHz for the bioelectric phenomena [97]. It was also reported in [24] that the displacement currents can be ignored at frequencies less than 100 kHz. For power system grounding applications, this direct current analysis is also valid for power system frequencies. The direct current analysis is also a realistic approximation when analysis is performed for large grounding system [98].

The Laplace's equation can be solved using the method of the separation of the variables when the appropriate boundary conditions are specified on the surface of a complete coordinate system. Such coordinates included the cylindrical and the spheroidal coordinates, where the Laplace's equation can be expressed as follows [95]:

(i) Cylindrical coordinates (r, ϕ, z):

$$\nabla^2 V = \frac{1}{r}\frac{\partial}{\partial r}\left(r\frac{\partial V}{\partial r}\right) + \frac{1}{r^2}\frac{\partial^2 V}{\partial \phi^2} + \frac{\partial^2 V}{\partial z^2} = 0. \tag{3.9}$$

(ii) Prolate spheroidal coordinates (η,δ,ϕ):

$$\nabla^2 V = \frac{\partial}{\partial\eta}\left[(\eta^2-1)\frac{\partial V}{\partial\eta}\right]+\frac{\partial}{\partial\delta}\left[(1-\delta^2)\frac{\partial V}{\partial\delta}\right]+\frac{\eta^2-\delta^2}{(\eta^2-1)(1-\delta^2)}\frac{\partial^2 V}{\partial\phi^2}=0. \tag{3.10}$$

(iii) Oblate spheroidal coordinates (η,δ,ϕ):

$$\nabla^2 V = \frac{\partial}{\partial\eta}\left[(\eta^2+1)\frac{\partial V}{\partial\eta}\right]+\frac{\partial}{\partial\delta}\left[(1-\delta^2)\frac{\partial V}{\partial\delta}\right]+\frac{\eta^2+\delta^2}{(\eta^2+1)(1-\delta^2)}\frac{\partial^2 V}{\partial\phi^2}=0. \tag{3.11}$$

3.3 The Relationship between the Spheroidal and the Cylindrical Coordinates Systems

A brief description of the spheroidal and the cylindrical coordinates systems is in order. The relationship between the prolate spheroidal coordinates (η,δ,ϕ) and the cylindrical coordinates (r,ϕ,z) [99] is shown in Fig. 3.1. η_0 denotes the surface of the prolate spheroid, a is the semifocal distance of the prolate spheroid, $a\sqrt{\eta_0^{\,2}-1}$ is the radius of the prolate spheroid and $2a\eta_0$ is the length of the prolate spheroid.

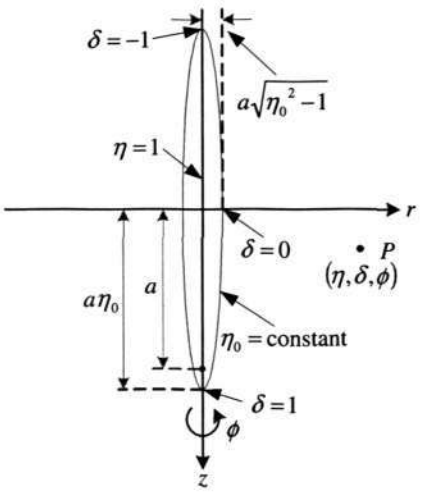

Figure 3.1 - The relationship between the prolate spheroidal coordinates (η,δ,ϕ) and the cylindrical coordinates (r,ϕ,z).

The relationship between the oblate spheroidal coordinates (η,δ,ϕ) and the cylindrical coordinates (r,ϕ,z) [99] is shown in Fig. 3.2. η_0 denotes the surface of the oblate spheroid, a is the semifocal distance of the oblate spheroid, $a\sqrt{\eta_0^2+1}$ is the radius of the oblate spheroid and $2a\eta_0$ is the thickness of the oblate spheroid.

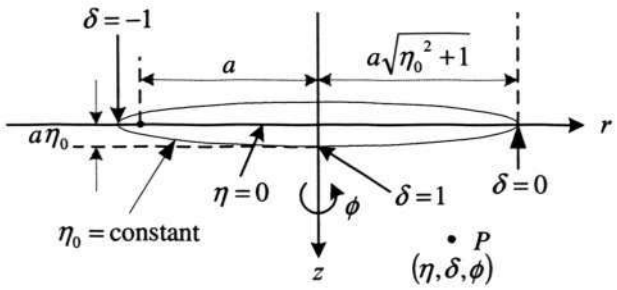

Figure 3.2 - The relationship between the oblate spheroidal coordinates (η,δ,ϕ) and the cylindrical coordinates (r,ϕ,z).

It is worthwhile to note that slender cylindrical and planar disc objects are often modelled using the spheroidal coordinates. The spheroidal coordinates are of consideration as the general ellipsoidal form covers, as an approximation, almost the whole variety of possible shapes for particles and segregates of physical interest [100]. Furthermore, the spheroids are examples of objects that have continuously varying surface curvatures [101]. The prolate and the oblate spheroids are of interest because the prolate and the oblate spheroids are good approximation to the slender cylinders [101-105] and the planar discs [103-105], respectively.

3.4 Solutions of the Laplace's Equations

3.4.1 Cylindrical coordinates

The general solution to the Laplace's equation in the cylindrical coordinates in (3.9) is shown as follows. Consider a point current source (r_s, z_s) embedded in a semi-infinite conductive medium of resistivity ρ as shown in Fig. 3.3. A total current of *I* is radiated from the source.

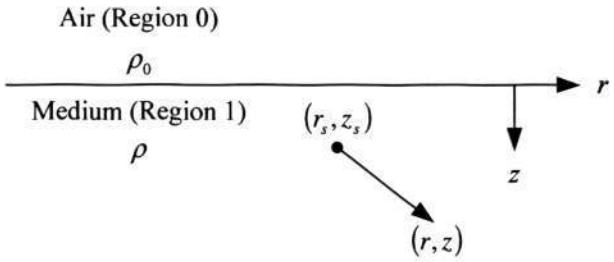

Figure 3.3 - Point current source (r_s, z_s) inside the semi-infinite conductive medium.

In Region 1 in the conductive medium, where there is a point current source and for the case where $0 \le z \le z_s$, the general solution to (3.9) is given as [96]:

$$V_{1-upper}(r,z) = \frac{\rho I}{4\pi}\left[\int_0^\infty J_0(\lambda r)e^{\lambda(z-z_s)}d\lambda + \int_0^\infty \theta_1(\lambda)J_0(\lambda r)e^{-\lambda z}d\lambda + \int_0^\infty \varphi_1 J_0(\lambda r)e^{+\lambda z}d\lambda\right]. \quad (3.12)$$

In the same region, where $z \ge z_s$, the general solution is given as:

$$V_{1-lower}(r,z) = \frac{\rho I}{4\pi}\left[\int_0^\infty J_0(\lambda r)e^{-\lambda(z-z_s)}d\lambda + \int_0^\infty \theta_1(\lambda)J_0(\lambda r)e^{-\lambda z}d\lambda + \int_0^\infty \varphi_1 J_0(\lambda r)e^{+\lambda z}d\lambda\right]. \quad (3.13)$$

In region 0 in the air,

$$V_0(r,z) = \frac{\rho I}{4\pi}\left[\int_0^\infty \theta_0(\lambda)J_0(\lambda r)e^{+\lambda z}d\lambda + \int_0^\infty \varphi_0 J_0(\lambda r)e^{-\lambda z}d\lambda\right]. \quad (3.14)$$

The following boundary conditions were applied to (3.12) to (3.14). As z goes to negative infinity, the value of $V_0(r,-\infty)$ must go to zero; i.e., $\varphi_0 = 0$, as the term $e^{-\lambda z}$ cannot exist.

Therefore,

$$V_0(r,z)=\frac{\rho I}{4\pi}\int_0^\infty \theta_0(\lambda)J_0(\lambda r)e^{+\lambda z}d\lambda\ . \tag{3.15}$$

Similarly, as z goes to infinity, the value of $V_1(r,\infty)$ must go to zero; i.e., $\varphi_1=0$. as the term $e^{+\lambda z}$ cannot exist.

$$V_{1-upper}(r,z)=\frac{\rho I}{4\pi}\left[\int_0^\infty J_0(\lambda r)e^{\lambda(z-z_s)}d\lambda+\int_0^\infty \theta_1(\lambda)J_0(\lambda r)e^{-\lambda z}d\lambda\right], \text{ and} \tag{3.16}$$

$$V_{1-lower}(r,z)=\frac{\rho I}{4\pi}\left[\int_0^\infty J_0(\lambda r)e^{-\lambda(z-z_s)}d\lambda+\int_0^\infty \theta_1(\lambda)J_0(\lambda r)e^{-\lambda z}d\lambda\right]. \tag{3.17}$$

At the interface between the air and the medium, the voltages and current densities normal to the interface are equal. Therefore,

$$V_{1-upper}(r,0)=V_0(r,0)$$

for all the values of r, and $J_{1-upper}\big|_{z=0}=J_0\big|_{z=0}$.

Hence, for all the values of r,

$$\frac{1}{\rho}\cdot\frac{dV_{1-upper}}{dz}\bigg|_{z=0}=0. \tag{3.18}$$

Substituting $z=0$ into (3.15) and (3.16) and equating them result in

$$\theta_0(\lambda)=e^{-\lambda z_s}+\theta_1(\lambda). \tag{3.19}$$

Also, solving (3.18), it is found that:

$$\theta_1(\lambda)=e^{-\lambda z_s}. \tag{3.20}$$

Substituting (3.20) into (3.19),

$$\theta_0(\lambda) = 2e^{-\lambda z_s}. \tag{3.21}$$

Finally, the general solutions for the voltage are obtained as follows. In Region 0, the potential of a point is given as:

$$V_0(r,z) = \frac{\rho I}{4\pi}\int_0^\infty 2J_0(\lambda r)e^{\lambda(z-z_s)}d\lambda. \tag{3.22}$$

In Region 1, for the case where $0 \le z \le z_s$, the potential of a point is given as:

$$V_{1-upper}(r,z) = \frac{\rho I}{4\pi}\left[\int_0^\infty J_0(\lambda r)e^{\lambda(z-z_s)}d\lambda + \int_0^\infty J_0(\lambda r)e^{-\lambda(z+z_s)}d\lambda\right]; \tag{3.23}$$

whereas, for the case where $z \ge z_s$, the potential of a point is given as:

$$V_{1-lower}(r,z) = \frac{\rho I}{4\pi}\left[\int_0^\infty J_0(\lambda r)e^{-\lambda(z-z_s)}d\lambda + \int_0^\infty J_0(\lambda r)e^{-\lambda(z+z_s)}d\lambda\right]. \tag{3.24}$$

Subsequently, only the potential in Region 1 is of interest [96].

Using the identity equation of Bessel function [96]:

$$\int_0^\infty J_0(\lambda r)e^{-\lambda z}d\lambda = \frac{1}{\sqrt{r^2+z^2}}. \tag{3.25}$$

Therefore, the potential of a point in the conductive medium that is induced by a point current source, derived in the cylindrical coordinates, is expressed as:

$$V_1(r,z) = \frac{\rho I}{4\pi}\left[\frac{1}{\sqrt{r^2+(z-z_s)^2}} + \frac{1}{\sqrt{r^2+(z+z_s)^2}}\right]. \tag{3.26}$$

3.4.2 Prolate spheroidal coordinates

The general solution to the Laplace's equation in the prolate spheroidal coordinates in (3.10) is shown as follows. Consider a prolate spheroid body in a conductive, homogeneous, isotropic and infinite medium, when a current point source is inside the prolate spheroid body, the potential distribution outside a prolate spheroid surface $\eta = \eta_0$, which is held at potential V_0 is expressed as [106]:

$$V = \sum_{n=0}^{\infty}\sum_{m=0}^{n}[A_{mn}\cos(m\phi) + B_{mn}\sin(m\phi)]P_n^m(\delta)\left[\frac{Q_n^m(\eta)}{Q_n^m(\eta_0)}\right] \tag{3.27}$$

where

$$A_{mn} = \frac{\varepsilon_m}{4\pi}(2n+1)\frac{(n-m)!}{(n+m)!}\int_0^{2\pi}\cos(m\phi)d\phi\int_{-1}^{1}V_0P_n^m(\delta)d\delta\,; \tag{3.28}$$

$$B_{mn} = \frac{\varepsilon_m}{4\pi}(2n+1)\frac{(n-m)!}{(n+m)!}\int_0^{2\pi}\sin(m\phi)d\phi\int_{-1}^{1}V_0P_n^m(\delta)d\delta\,; \text{ and} \tag{3.29}$$

ε_m is the Neumann factor, $\varepsilon_0 = 1, \varepsilon_n = 2\,(n = 1, 2, 3, \ldots)$.

For a constant potential V_0 over the surface of the prolate spheroid body, this implies that the potential V is independent of the coordinate ϕ. Hence, $\int_0^{2\pi}\cos(m\phi)d\phi = \text{constant}$, which occurs when $\cos(m\phi) = 1$. This arises when m = 0. Similarly, for a constant V_0 over the surface of the prolate spheroid body, the V is also independent of the coordinate δ. Hence, $\int_{-1}^{1}V_0P_n^m(\delta)d\delta = V_0\int_{-1}^{1}P_n^m(\delta)d\delta = \text{constant}$, which occurs when $P_n^m(\delta) = 1$. This arises when $m = n = 0$.

Therefore, for constant V_0 over the surface of the prolate spheroid body, the potential distribution is:

$$V = [A_{00}\cos(0) + B_{00}\sin(0)]P_0(\delta)\left[\frac{Q_0(\eta)}{Q_0(\eta_0)}\right] = A_{00}P_0(\delta)\left[\frac{Q_0(\eta)}{Q_0(\eta_0)}\right] \tag{3.30}$$

where, from (3.28)

$$A_{00} = \frac{\varepsilon_0}{4\pi}(1)\frac{(0)!}{(0)!}\int_0^{2\pi}\cos(0)d\phi\int_1^1 V_0P_0(\delta)d\delta\,. \tag{3.31}$$

Now

$P_n(\delta) = \frac{1}{2^n n!}\frac{d^n}{dz^n}\left[z^2-1\right]^n$, which implies that, for $n = 0$:

$$P_0(\delta) = \frac{1}{2^0(0)!}\frac{d^0}{dz^0}\left[z^2-1\right]^0 = 1\,. \tag{3.32}$$

For $m = 0$, the value of ε_m is

$$\varepsilon_0 = 1\,. \tag{3.33}$$

Therefore, substituting (3.32) and (3.33) into (3.31), the value of A_{00} is expressed as:

$$\begin{aligned} A_{00} &= \frac{1}{4\pi}\int_0^{2\pi}(1)d\phi\int_1^1 V_0(1)d\delta \\ &= \frac{1}{4\pi}(2\pi)V_0(2) \\ &= V_0\,. \end{aligned} \tag{3.34}$$

Consequently, from (3.30), for a constant V_0 at the prolate spheroid surface, the potential distribution is expressed as:

$$V = V_0\left[\frac{Q_0(\eta)}{Q_0(\eta_0)}\right]. \tag{3.35}$$

Now, for $z>1$,

$$Q_n(z)=\frac{1}{2^n n!}\frac{d^n}{dz^n}\left[(z^2-1)^n \ln\left(\frac{z+1}{z-1}\right)\right]-\frac{1}{2}P_n(z)\ln\left(\frac{z+1}{z-1}\right). \tag{3.36}$$

Substituting $n=0$ into (3.36):

$$\begin{aligned} Q_0(z)&=\frac{1}{2^0(0)!}\frac{d^0}{dz^0}\left[(z^2-1)^0 \ln\left(\frac{z+1}{z-1}\right)\right]-\frac{1}{2}P_0(z)\ln\left(\frac{z+1}{z-1}\right)\\ &=\ln\left(\frac{z+1}{z-1}\right)-\frac{1}{2}\ln\left(\frac{z+1}{z-1}\right)\\ &=\frac{1}{2}\ln\left(\frac{z+1}{z-1}\right). \end{aligned} \tag{3.37}$$

Substitute (3.37) into (3.35), the potential distribution V is expressed as:

$$\begin{aligned} V&=V_0\left[\frac{1}{2}\ln\left(\frac{\eta+1}{\eta-1}\right)\Big/\frac{1}{2}\ln\left(\frac{\eta_0+1}{\eta_0-1}\right)\right]\\ &=V_0\left[\ln\left(\frac{\eta+1}{\eta-1}\right)\Big/\ln\left(\frac{\eta_0+1}{\eta_0-1}\right)\right]. \end{aligned} \tag{3.38}$$

The total current I applied to the prolate spheroid shaped electrode must cross the surface of the electrode at $\eta=\eta_0$, hence I can be expressed as [99]:

$$\begin{aligned} I&=-\frac{1}{\rho}\int_1\int_0^{2\pi}\frac{1}{h_\eta}\frac{\partial V}{\partial \eta}h_\phi d\phi h_\delta d\delta\Big|_{\eta=\eta_0}\\ &=-\frac{1}{\rho}\frac{h_{\phi_0}h_{\delta_0}}{h_{\eta_0}}(4\pi)\frac{V_0}{Q_0(\eta_0)}\left(-\frac{1}{\eta_0^{\,2}-1}\right)\\ &=\frac{4\pi V_0}{\rho(\eta_0^{\,2}-1)Q_0(\eta_0)}\frac{h_{\phi_0}h_{\delta_0}}{h_{\eta_0}}. \end{aligned} \tag{3.39}$$

where from (3.37), $\dfrac{dQ_0(\eta)}{d\eta}=\dfrac{d}{d\eta}\left[\dfrac{1}{2}\ln\left(\dfrac{\eta+1}{\eta-1}\right)\right]=-\dfrac{1}{\eta^2-1}$.

The metric coefficients h_η, h_δ, and h_ϕ are obtained from [107] and derived as:

$$h_\eta = a\sqrt{\frac{\eta^2-\delta^2}{\eta^2-1}}; \tag{3.40}$$

$$h_\delta = a\sqrt{\frac{\eta^2-\delta^2}{1-\delta^2}}; \text{ and} \tag{3.41}$$

$$h_\phi = a\sqrt{(\eta^2-1)(1-\delta^2)}. \tag{3.42}$$

From (3.40) to (3.42),

$$\begin{aligned}\frac{h_{\phi_0}h_{\delta_0}}{h_{\eta_0}} &= \frac{a^2\sqrt{(\eta_0^2-\delta_0^2)(\eta_0^2-1)}}{a\sqrt{\frac{\eta_0^2-\delta_0^2}{\eta_0^2-1}}} \\ &= a(\eta_0^2-1).\end{aligned} \tag{3.43}$$

Substituting (3.43) into (3.39), I can be expressed as:

$$\begin{aligned}I &= \frac{4\pi a(\eta_0^2-1)V_0}{\rho(\eta_0^2-1)Q_0(\eta_0)} \\ &= \frac{4\pi a}{\rho}\left[\frac{V_0}{Q_0(\eta_0)}\right].\end{aligned} \tag{3.44}$$

Substituting (3.44) into (3.38), the potential V of a point in the conductive medium induced by a point current source I, derived in the prolate spheroidal coordinates, is expressed as:

$$\begin{aligned}V &= \frac{\rho I}{4\pi a}Q_0(\eta_0)\left[\ln\left(\frac{\eta+1}{\eta-1}\right)\Big/\ln\left(\frac{\eta_0+1}{\eta_0-1}\right)\right] \\ &= \frac{\rho I}{4\pi a}\left(\frac{1}{2}\right)\ln\left(\frac{\eta_0+1}{\eta_0-1}\right)\left[\ln\left(\frac{\eta+1}{\eta-1}\right)\Big/\ln\left(\frac{\eta_0+1}{\eta_0-1}\right)\right] \\ &= \frac{\rho I}{8\pi a}\ln\left(\frac{\eta+1}{\eta-1}\right).\end{aligned} \tag{3.45}$$

η is obtained from the defining equation for a confocal family of spheroids that is given by [99]:

$$\frac{r^2}{a^2(\eta^2-1)}+\frac{z^2}{a^2\eta^2}=1. \tag{3.46}$$

From (3.46), η is expressed as:

$$\begin{aligned} r^2\eta^2+z^2(\eta^2-1)&=a^2(\eta^2-1)\eta^2 \\ \eta^2&=\frac{(a^2+r^2+z^2)\pm\sqrt{(a^2+r^2+z^2)^2-4a^2z^2}}{2a^2} \\ \eta&=\sqrt{\frac{(a^2+r^2+z^2)\pm\sqrt{(a^2+r^2+z^2)^2-4a^2z^2}}{2a^2}}. \end{aligned} \tag{3.47}$$

Since the range of η is $1\le\eta<\infty$, therefore, from (3.47), η is obtained using:

$$\eta=\sqrt{\frac{(a^2+r^2+z^2)+\sqrt{(a^2+r^2+z^2)^2-4a^2z^2}}{2a^2}}. \tag{3.48}$$

For a long and thin or slender cylindrical electrode, the prolate spheroid surface $\eta_0\cong 1$ [99] and since $a=l_c/\eta_0$, hence $a\cong l_c$. Therefore, from (3.45) and (3.48), the potential V of a point in the conductive medium that is induced by a point current source I in the prolate spheroidal coordinates is expressed as:

$$V=\frac{\rho I}{8\pi l_c}\ln\left(\frac{\eta+1}{\eta-1}\right) \tag{3.49}$$

$$\text{where } \eta=\sqrt{\frac{(l_c^{\,2}+r^2+z^2)+\sqrt{(l_c^{\,2}+r^2+z^2)^2-4l_c^{\,2}z^2}}{2l_c^{\,2}}}. \tag{3.50}$$

3.4.3 Oblate spheroidal coordinates

The general solution to the Laplace's equation in the oblate spheroidal coordinates in (3.11) is shown as follows. Consider an oblate spheroid body in a conductive, homogeneous, isotropic and infinite medium. Similar to discussions given in Section 3.4.2, for a constant potential V_0 over the surface of the oblate spheroid, denoted by η_0, the potential function V is again independent of the coordinates δ and ϕ. Hence, when a current point source is inside the oblate spheroid body, the potential distribution outside a oblate spheroid surface $\eta = \eta_0$, is given by [107]:

$$\begin{aligned} V &= A + B\cot^{-1}(\eta) \\ &= A + B\tan^{-1}(1/\eta) \end{aligned} \tag{3.51}$$

where A and B are solved as follows. The potential V of a point at a large or infinite distance from the current source or sink is zero, i.e., $V \to 0$ as $\eta \to \infty$. As $\eta \to \infty$, $(1/\eta) \to 0$, and consequently, $\tan^{-1}(0) = 0$. Therefore, (3.51) can be expressed as:

$$\begin{aligned} V &= A + B\tan^{-1}(1/\eta)\Big|_{\eta\to\infty} \\ &= A + B\tan^{-1}(0) \\ &= 0. \end{aligned} \tag{3.52}$$

For (3.52) to be zero and due to the fact that $B\tan^{-1}(0) = 0$, this implies that:

$$A = 0. \tag{3.53}$$

An oblate spheroid body will represent a planar disc when $\eta = 0$ [106]. Therefore, at the surface of a disc modelled in the oblate spheroidal coordinates, i.e., at $\eta = \eta_0 = 0$, the potential on the surface of the oblate spheroid body, which is denoted by V_0, is expressed as:

$$\begin{aligned} V_0 &= B\tan^{-1}(1/\eta)\big|_{\eta\to 0} \\ &= B\tan^{-1}(\infty) \\ &= B(\pi/2). \end{aligned} \tag{3.54}$$

Rearranging (3.54), $B = 2V_0/\pi$. (3.55)

Substituting (3.53) and (3.55) in (3.51), the potential distribution is expressed as:

$$V = \frac{2V_0}{\pi}\tan^{-1}\left(\frac{1}{\eta}\right). \tag{3.56}$$

The total current I applied to the oblate spheroid body must cross the surface of the oblate spheroid at $\eta = \eta_0$, hence [99]:

$$\begin{aligned} I &= -\frac{1}{\rho}\int_{-1}^{1}\int_{0}^{2\pi}\frac{1}{h_\eta}\frac{\partial V}{\partial \eta}h_\phi d\phi h_\delta d\delta\Big|_{\eta=\eta_0} \\ &= -\frac{1}{\rho}\frac{h_{\phi_0}h_{\delta_0}}{h_{\eta_0}}(2)(2\pi)\frac{2V_0}{\pi}\left(-\frac{1}{\eta_0^{\,2}+1}\right) \\ &= \frac{8V_0}{\rho(\eta_0^{\,2}+1)}\frac{h_{\phi_0}h_{\delta_0}}{h_{\eta_0}} \end{aligned} \tag{3.57}$$

where $\dfrac{d}{d\eta}\left[\tan^{-1}\left(\frac{1}{\eta}\right)\right]\Big|_{\eta=\eta_0} = -\dfrac{1}{\eta_0^{\,2}+1}$.

The metric coefficients for the oblate spheroidal coefficients are expressed as [107]:

$$h_\eta = a\sqrt{\frac{\eta^2+\delta^2}{\eta^2+1}}; \tag{3.58}$$

$$h_\delta = a\sqrt{\frac{\eta^2+\delta^2}{1-\delta^2}}\text{; and} \tag{3.59}$$

$$h_\phi = a\sqrt{(\eta^2+1)(1-\delta^2)}. \tag{3.60}$$

Substituting (3.58), (3.59) and (3.60) into (3.57), the total current I applied to the surface of the oblate spheroid body at $\eta = \eta_0$ is expressed as:

$$\begin{aligned} I &= \frac{8V_0}{\rho\left(\eta_0^{\,2}+1\right)}\left[\frac{a^2\sqrt{\left(\eta_0^{\,2}+\delta_0^{\,2}\right)\left(\eta_0^{\,2}+1\right)}}{a\sqrt{\left(\eta_0^{\,2}+\delta_0^{\,2}\right)/\left(\eta_0^{\,2}+1\right)}}\right] \\ &= \frac{8V_0}{\rho\left(\eta_0^{\,2}+1\right)}\left[a\left(\eta_0^{\,2}+1\right)\right] \\ &= \frac{8aV_0}{\rho}. \end{aligned} \tag{3.61}$$

Rearranging (3.61), the self-potential of an oblate spheroid is expressed as:

$$V_0 = \frac{\rho I}{8a}. \tag{3.62}$$

Substituting (3.62) into (3.56), the potential V of a point in the conductive medium induced by a point current source I, derived in the oblate spheroidal coordinates, is expressed as:

$$V = \frac{\rho I}{4\pi a}\tan^{-1}\left(\frac{1}{\eta}\right). \tag{3.63}$$

η is obtained from the defining equation for a confocal family of spheroids that is given by [95]:

$$\frac{r^2}{a^2\left(\eta^2+1\right)}+\frac{z^2}{a^2\eta^2}=1. \tag{3.64}$$

From (3.64), η is expressed as:

$$\begin{aligned} &r^2\eta^2 + z^2\left(\eta^2+1\right) = a^2\left(\eta^2+1\right)\eta^2 \\ &\eta^2 = \frac{\left(-a^2+r^2+z^2\right)\pm\sqrt{\left(-a^2+r^2+z^2\right)^2+4a^2z^2}}{2a^2} \\ &\eta = \sqrt{\frac{\left(-a^2+r^2+z^2\right)\pm\sqrt{\left(-a^2+r^2+z^2\right)^2+4a^2z^2}}{2a^2}}. \end{aligned} \tag{3.65}$$

Since the range of η is $0 \le \eta < \infty$, therefore, from (3.65), η is obtained using:

$$\eta = \sqrt{\frac{\left(-a^2 + r^2 + z^2\right) + \sqrt{\left(-a^2 + r^2 + z^2\right)^2 + 4a^2 z^2}}{2a^2}}. \tag{3.66}$$

For a planar thin disc electrodes, with radius b, the oblate spheroid surface $\eta_0 \cong 0$ [106] and hence $a \cong b$. Therefore, from (3.63) and (3.66), the potential V of a point in the conductive medium that is induced by a point current source I in the prolate spheroidal coordinates is expressed as:

$$V = \frac{\rho I}{4\pi b} \tan^{-1}\left(\frac{1}{\eta}\right) \tag{3.67}$$

$$\text{with } \eta = \sqrt{\frac{\left(-b^2 + r^2 + z^2\right) + \sqrt{\left(-b^2 + r^2 + z^2\right)^2 + 4b^2 z^2}}{2b^2}}. \tag{3.68}$$

3.5 Concluding Remarks

In this chapter, the derivations of the fundamental expressions of the potential of a point in the conductive medium induced by a point current source, in the cylindrical and the spheroidal coordinates, which are available in the literature, are reviewed. These expressions are used in the derivations of the geometric factors for the resistivity measurements by means of both the four and the two-electrode methods, which are discussed in the subsequent chapters.

CHAPTER 4 - RESISTIVITY MEASUREMENT OF FINITE-VOLUME SAMPLES USING THE FOUR-ELECTRODE METHOD WITH CONSIDERATION OF THE FINITE DIMENSIONS OF THE ELECTRODES

4.1 Overview

The use of the four-electrode method for resistivity measurement in biomedical applications is studied in this chapter. Measurements of the tissue resistivities are important in the study of the biological systems and the four-electrode method, by means of the slender cylindrical electrodes, is commonly used for the *in situ* resistivity measurements [4, 12, 22, 26-31]. In the four-electrode method as shown in Fig. 4.1, which was proposed by Wenner [25], an array of four slender cylindrical electrodes, each of length l_c, was arranged in a straight line with equal inter-electrode spacing, s. It is to be noted that throughout this thesis, s and l_c denote the inter-electrode spacing and the length of the immersed electrode, respectively.

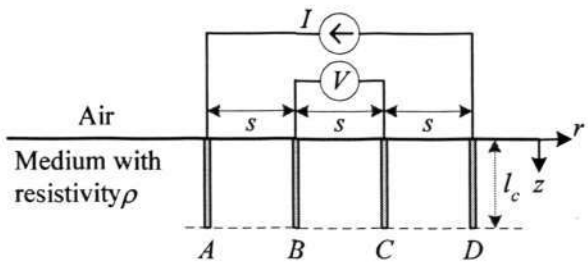

Figure 4.1 - Four-electrode method for *in situ* resistivity measurement using slender cylindrical electrodes.

It is worthwhile to note that besides the use of the slender cylindrical electrodes, *in situ* resistivity measurements have also been conducted using the planar disc electrodes [24], as shown in Fig. 4.2. It is to be noted that the radius of the disc electrode is denoted by b.

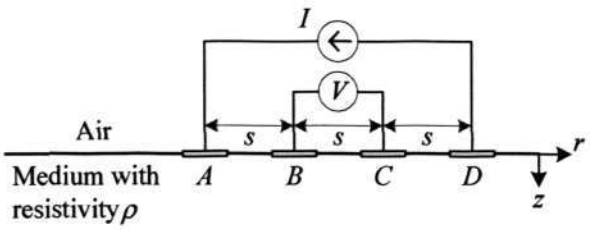

Figure 4.2 - Four-electrode method for *in situ* resistivity measurement using planar disc electrodes.

Referring to Fig. 4.1, the current stimulus electrodes *A* and *D* are modelled as point current source and sink, respectively, whereas the electrodes *B* and *C* are modelled as point potential electrodes. The potential difference *V* between the two non-current carrying inner electrodes *B* and *C* is measured using a precision instrumentation differential amplifier with a high input impedance when a current *I* flows between the two outer electrodes *A* and *D*. The effect of the electrode polarisation at the current source and sink electrodes, which have been shown to be dependent on the electrode material, current density, frequency of excitation signals, etc., is usually modelled by the Randles equivalent circuit [108]. By using separate pairs of electrodes for the flow of excitation current and voltage sensing, the problems associated with the effect of the electrode polarisation impedance at the measurement electrodes can be effectively eliminated [3, 12, 22, 23, 27, 28, 30, 47, 82-86]. The effects of the electrode polarisation impedance on the measurements were made negligible at the potential electrodes by the high input impedance of the measurement circuit that is used to measure the potential difference across the measurement electrodes, which are the potential electrodes [26].

Consider a four-electrode measurement system with the electrodes arranged such that the finite dimensions of the electrodes are small in comparison to *s*, i.e., either l_c is small in comparison to *s* in the case of the slender cylindrical electrodes, or *b* is small in comparison to *s* in the case of the planar disc electrodes. All the electrodes are immersed in a homogeneous, isotropic and semi-infinite medium, and the four electrodes are modelled as points. In the

circumstances, the resistivity of the medium is obtained from the following well-known expression [24, 26, 27, 37]:

$$\rho_{4E,pt} = \left(K_{4E,pt}\right)R \tag{4.1}$$

where $K_{4E,pt}$ is the geometric factor, $\rho_{4E,pt}$ is the resistivity determined using $K_{4E,pt}$. Here, $K_{4E,pt} = 2\pi s$ and R is the measured resistance $\left(R = V/I\right)$. The subscripts $4E$ and pt denote four-electrode and point, respectively. When the medium is non-homogenous, the apparent resistivity is determined. It is to be noted that the apparent resistivity, or the resistivity for a homogeneous medium, is a function of the s. The inverse of the electrical resistivity ρ is the electrical conductivity σ.

Due to the differences in the experimental set-up and the types of tissue tested, there exists a wide variation in the published values of the tissue resistivity, ranging from 1 $\Omega \cdot$m to 25 $\Omega \cdot$m [4, 12, 22, 26-28]. According to Geddes, other possible reasons for the wide range of resistivities include the frequency used and the nature of the tissue [32]. The wide variation in the reported resistivities have also been viewed from a measurement theoretical viewpoint and attributed to one or more of the following factors [2]:

(i) errors in the measurement set-up and the method applied to calculate the resistivity from the actual measured data,

(ii) differences in the tissue preparation and conditioning, and

(iii) inter-individual differences in the (patho-) physiological state of the tissue samples.

The calibrations of the experimental set-ups and the experiments pertaining to the biomedical analysis and applications have often been conducted by means of a saline solution and/or a layer of agar gel [12, 22, 28, 29, 35, 40, 46, 47, 50, 51, 109-117]. In particular, a physical

model consisting of air, a saline solution layer and an agar layer has also been used to demonstrate the dependence of apparent resistance of four-electrode probes on insertion depth [28]. Studies based on computer simulation and experimental results have shown that in situations whereby the slender cylindrical electrodes are used and l_c is not small in comparison to s, the measured tissue resistivity, which is obtained using $K_{4E,pt}$ in (4.1), is affected by the geometry of the four-electrode probes [27]. In practice, the measurements of many tissue samples would require a small s in comparison to l_c, for example, s = 1.5 mm and l_c = 6 mm [12]. In [12], the measurement set-up was calibrated with a saline solution of known resistivity.

The subject of using the slender cylindrical or plunge electrodes for the resistivity measurement is of particular concern. It is noted that in the event that l_c is not small in comparison to s for the resistivity measurement, the condition for which (4.1) is applicable will be violated. As such, electrodes A and D can no longer be modelled simply as point current source and sink. In the circumstances, it becomes necessary to consider the dimensions of the source and sink electrodes in the model to derive the geometric factor for resistivity measurement. The modelling of the slender cylindrical electrodes in the cylindrical coordinates for the determination of the resistivity in the four-electrode method has been presented by Baishiki *et al.* [37], and the Baishiki's geometric factor is expressed as follows:

$$\rho_{4E,cyl} = (K_{4E,cyl})R \tag{4.2}$$

where $K_{4E,cyl}$ is the geometric factor and the subscripts $4E$ and *cyl* denote four-electrode and cylindrical, respectively. $\rho_{4E,cyl}$ is the resistivity determined using $K_{4E,cyl}$ and

$$K_{4E,cyl} = \frac{2\pi l_c}{2\ln\left[\frac{2+\sqrt{4+(s/l_c)^2}}{1+\sqrt{1+(s/l_c)^2}}\right] + 2\sqrt{1+(s/l_c)^2} - \sqrt{4+(s/l_c)^2} - \left(\frac{s}{l_c}\right)}.$$

It is worthwhile to note that (4.2) is derived in the cylindrical coordinates by assuming that the current distribution is uniform along the electrode except at the end of the electrode [37], as shown in Fig. 4.3(a). The stimulus source or the sink electrode is represented by a line current source or sink of constant current density and the potential of a point in the medium is not a function of the diameter of the stimulus electrode.

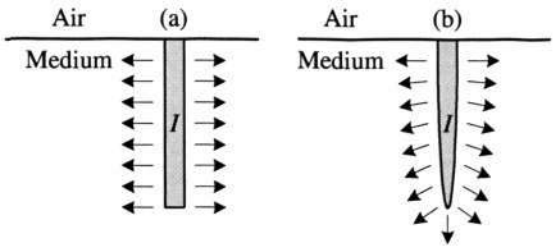

Figure 4.3 - Current distribution of a current source electrode modelled in (a) the cylindrical coordinates and (b) the prolate spheroidal coordinates.

In this chapter, the slender cylindrical source and sink electrodes are modelled in the prolate spheroidal coordinates. The spheroidal coordinates are in consideration as the general ellipsoidal form covers, as an approximation, almost the whole variety of possible shapes for particles and segregates of physical interest [100]. Furthermore, the spheroids are examples of objects that have continuously varying surface curvatures [101]. The prolate spheroids are of fundamental interest because the prolate spheroids are good approximation to the cylinders [101-105]. In addition, when the stimulus source electrode is modelled in the prolate spheroidal coordinates, the current distribution is emanating all round the surface of the electrode, as shown in Fig. 4.3(b), and the diameter of the stimulus electrode is also taken into consideration. The modelling of a single cylindrical electrode in the prolate spheroidal coordinates has been explored and an expression for the resistance of such an electrode has been presented [99].

The contributions of this chapter are the theoretical derivation and the experimental validation of a new geometric factor, derived in the prolate spheroidal coordinates, for resistivity measurement using four slender cylindrical electrodes. The theoretical geometric factor took the shape and dimensions of the electrodes and the spacing between them into account in order to obtain the dependence of the resistance between the electrodes on the resistivity of the medium. The evaluation of the experimental results showed that the saline resistivities obtained using the derived geometric factor were accurate and consistent in a wider range of cases, even when l_e was either comparable to or larger than s. The evaluation also showed the effect of the relative size of the sample volume when the limitation to the semi-infinite volume began to result in poor accuracy.

This chapter is organised as follows. A new geometric factor for the resistivity measurement using the four-electrode method is derived in the prolate spheroidal coordinates as described in Section 4.2 The numerical simulations results conducted using the derived geometric factor are shown in Section 4.3. The measurement system is described in Section 4.4. The experimental set-up and the experimental procedures are described in sections 4.5 and 4.6, respectively. The measurements were taken in the laboratory using slender cylindrical silver (Ag) electrodes immersed in the saline solutions. The experimental results are presented, evaluated and discussed in Section 4.7. The concluding remarks are given in Section 4.8.

4.2 The Theoretical Geometric Factor for Resistivity Measurement with Slender Cylindrical Electrodes Modelled using the Prolate Spheroidal Coordinates

The theoretical geometric factor for the resistivity measurement using the four-electrode method with slender cylindrical electrodes modelled using the prolate spheroidal coordinates

is shown hereafter. Consider the four-electrode method as shown in Fig. 4.1, which uses four slender cylindrical electrodes. The terms "slender" and "cylindrical" are used to describe a cylindrical rod electrode which has a circumference that is small in proportion to its length.

4.2.1 Potential of a point

The current source and sink electrodes, A and D, respectively, are modelled in the prolate spheroidal coordinates as shown in Fig. 4.4.

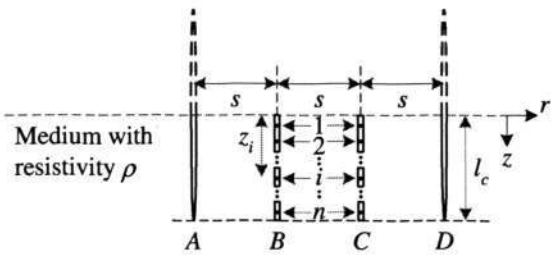

Figure 4.4 - Application of the image method for currents to the current source and sink electrodes A and D, respectively, with the electrodes modelled in the prolate spheroidal coordinates.

A brief description of the prolate spheroidal coordinates system has been given in Section 3.4.2. Consider a half-prolate spheroid source electrode with current I in a conductive, homogeneous, isotropic and semi-infinite medium. Applying the image method for currents [118], the result is a prolate spheroid with a current of $2I$ emanating from its surface into an infinite medium of resistivity ρ. Making use of (3.49), the potential of a point P in the medium induced by the source electrode with current $2I$ is given by [99]:

$$\begin{aligned} V &= \frac{\rho(2I)}{8\pi l_c}\ln\left(\frac{\eta+1}{\eta-1}\right) \\ &= \frac{\rho I}{4\pi l_c}\ln\left(\frac{\eta+1}{\eta-1}\right) \end{aligned} \tag{4.3}$$

with η defined in (3.50).

4.2.2 Potential of an electrode

The problem of determination of the resistivity using the four-electrode method in the prolate spheroidal coordinates is now addressed. It is assumed that the presence of the potential sensing electrodes do not affect the electric field lines generated by the current source and sink electrodes. Referring to Fig. 4.4, each potential sensing electrode is divided into n segments with each segment i located at a depth z_i. It is to be noted that all the electrodes in Fig. 4.4 have the same l_c. The potential of the i^{th} segment of the electrode B, which is induced by the current source and its image at the electrode A, is determined using (4.3). This potential of the electrode B, which is denoted as $V_{B,A}$, is then determined by averaging the total potential of every segment along the length of the electrode B and expressed as:

$$V_{B,A} = \frac{\rho I}{4\pi l_c}\left(\frac{1}{n}\right)\sum_{i=1}^{n}\ln\left(\frac{\eta_{1,i}+1}{\eta_{1,i}-1}\right). \tag{4.4}$$

The value of $\eta_{1,i}$ in (4.4) is obtained from (3.50) by substituting $r = s$ as shown below:

$$\eta_{1,i} = \sqrt{\frac{\left(l_c^{\,2}+s^2+z_i^{\,2}\right)+\sqrt{\left(l_c^{\,2}+s^2+z_i^{\,2}\right)^2-4l_c^{\,2}z_i^{\,2}}}{2l_c^{\,2}}} \tag{4.5}$$

where $z_i = [l_c(2i-1)]/2n$.

Similarly, the potential of the i^{th} segment of the electrode B, which is induced by the current sink and its image at the electrode D, is determined using (4.3). This potential of the electrode B, which is denoted as $V_{B,D}$, is then determined by averaging the total potential of every segment along the length of the electrode B and expressed as:

$$V_{B,D} = \frac{-\rho I}{4\pi l_c}\left(\frac{1}{n}\right)\sum_{i=1}^{n}\ln\left(\frac{\eta_{2,i}+1}{\eta_{2,i}-1}\right). \tag{4.6}$$

The value of $\eta_{2,i}$ in (4.6) is obtained from (3.50) by substituting $r = 2s$ as shown below:

$$\eta_{2,i} = \sqrt{\frac{\left(l_c^{\,2} + 4s^2 + z_i^{\,2}\right) + \sqrt{\left(l_c^{\,2} + 4s^2 + z_i^{\,2}\right)^2 - 4l_c^{\,2} z_i^{\,2}}}{2l_c^{\,2}}}. \tag{4.7}$$

The overall potential of the electrode B, which is denoted as V_B, is obtained by adding $V_{B,A}$ and $V_{B,D}$, i.e., adding (4.4) and (4.6), respectively and expressed as:

$$V_B = \frac{\rho I}{4\pi l_c}\left(\frac{1}{n}\right)\sum_{i=1}^{n} \ln\left[\left(\frac{\eta_{1,i}+1}{\eta_{1,i}-1}\right)\left(\frac{\eta_{2,i}-1}{\eta_{2,i}+1}\right)\right]. \tag{4.8}$$

Next, the potential of the i^{th} segment of the electrode C, which is induced by the current source and its image at the electrode A, is determined using (4.3). This potential of the electrode C, which is denoted as $V_{C,A}$, is then determined by averaging the total potential of every segment along the length of the electrode C and expressed as:

$$V_{C,A} = \frac{\rho I}{4\pi l_c}\left(\frac{1}{n}\right)\sum_{i=1}^{n} \ln\left(\frac{\eta_{2,i}+1}{\eta_{2,i}-1}\right). \tag{4.9}$$

Similarly, the potential of the i^{th} segment of the electrode C, which is induced by the current sink and its image at the electrode D, is determined using (4.3). This potential of the electrode C, which is denoted as $V_{C,D}$, is then determined by averaging the total potential of every segment along the length of the electrode C and expressed as:

$$V_{C,D} = \frac{-\rho I}{4\pi l_c}\left(\frac{1}{n}\right)\sum_{i=1}^{n} \ln\left(\frac{\eta_{1,i}+1}{\eta_{1,i}-1}\right). \tag{4.10}$$

The overall potential of the electrode C, which is denoted as V_C, is obtained by adding $V_{C,A}$ and $V_{C,D}$, i.e., adding (4.9) and (4.10), respectively and expressed as:

$$V_C = \frac{-\rho I}{4\pi l_c}\left(\frac{1}{n}\right)\sum_{i=1}^{n}\ln\left[\left(\frac{\eta_{1,i}+1}{\eta_{1,i}-1}\right)\left(\frac{\eta_{2,i}-1}{\eta_{2,i}+1}\right)\right]. \tag{4.11}$$

4.2.3 Potential difference between electrodes B and C

The potential difference between the two inner electrodes B and C, which is denoted as V, is obtained by subtracting V_C (4.11) from V_B (4.8), and expressed as:

$$V = \frac{\rho I}{2\pi l_c}\left(\frac{1}{n}\right)\sum_{i=1}^{n}\ln\left[\left(\frac{\eta_{1,i}+1}{\eta_{1,i}-1}\right)\left(\frac{\eta_{2,i}-1}{\eta_{2,i}+1}\right)\right]. \tag{4.12}$$

4.2.4 Theoretical geometric factor for resistivity measurement using the four-electrode method in the prolate spheroidal coordinates

Therefore, with regards to the four-electrode method using slender cylindrical electrodes in the prolate spheroidal coordinates, rearranging (4.12) and denoting the resistivity measured as $\rho_{4E,ps}$, we get:

$$\rho_{4E,ps} = \left(K_{4E,ps}\right)R_{4E} \tag{4.13}$$

where $R_{4E} = V/I$. The subscripts $4E$ and ps denote four-electrode and prolate spheroidal, respectively. The theoretical geometric factor $K_{4E,ps}$ is expressed as [119]:

$$K_{4E,ps} = \frac{2\pi l_c}{\left(\frac{1}{n}\right)\sum_{i=1}^{n}\ln\left[\left(\frac{\eta_{1,i}+1}{\eta_{1,i}-1}\right)\left(\frac{\eta_{2,i}-1}{\eta_{2,i}+1}\right)\right]} \tag{4.14}$$

with $\eta_{1,i}$ and $\eta_{2,i}$ defined in (4.5) and (4.7), respectively.

In the event that electrodes B and C are considered as points on the surface of the medium, the expression (4.14) is simplified to:

$$K_{4E,ps} = \frac{2\pi l_c}{\ln\left[\left(\frac{\eta_1+1}{\eta_1-1}\right)\left(\frac{\eta_2-1}{\eta_2+1}\right)\right]} \tag{4.15}$$

where from (4.5) and (4.7),

$$\eta_1 = \sqrt{(s/l_c)^2+1}\text{, and} \tag{4.16}$$

$$\eta_2 = \sqrt{(2s/l_c)^2+1}\text{, respectively.} \tag{4.17}$$

4.3 Numerical Simulations of the Derived Geometric Factor

Using numerical simulations, the effects of s, l_c and n on $K_{4E,ps}$ in (4.14) were investigated, and the results were tabulated in Table 4.I. The effects of s and l_c on $K_{4E,pt}$ in (4.1) and $K_{4E,cyl}$ in (4.2) were also simulated and tabulated in Table 4.I.

Table 4.I - Numerical values of the geometric factors for different inter-electrode spacing, immersed electrode length and number of segments.

l_c (mm)	s (mm)	$K_{4E,pt}$	$K_{4E,cyl}$	$K_{4E,ps}$ $n=1$	$K_{4E,ps}$ $n=5$	$K_{4E,ps}$ $n=10$	$K_{4E,ps}$ $n=100$
5	1	0.006	0.026	0.025	0.032	0.034	0.036
	2	0.013	0.030	0.029	0.033	0.034	0.035
	3	0.019	0.034	0.033	0.036	0.037	0.037
	4	0.025	0.03	0.038	0.040	0.040	0.041
	5	0.031	0.044	0.043	0.045	0.045	0.045
	10	0.063	0.071	0.070	0.071	0.071	0.071
	20	0.126	0.130	0.130	0.130	0.130	0.130
	30	0.189	0.192	0.191	0.191	0.192	0.192
	40	0.251	0.254	0.253	0.254	0.254	0.254

10	1	0.006	0.049	0.046	0.064	0.076	0.093
	2	0.013	0.052	0.049	0.063	0.068	0.073
	3	0.019	0.056	0.053	0.064	0.067	0.069
	4	0.025	0.060	0.057	0.066	0.068	0.069
	5	0.031	0.064	0.061	0.069	0.070	0.071
	10	0.063	0.088	0.085	0.089	0.900	0.900
	20	0.126	0.142	0.140	0.142	0.142	0.142
	30	0.189	0.200	0.199	0.200	0.200	0.200
	40	0.251	0.260	0.259	0.260	0.260	0.260

The plots of $K_{4E,pt}$, $K_{4E,cyl}$, and $K_{4E,ps}$ for l_c of 5 mm and 10 mm as s was varied are shown in Fig. 4.5(a). In the numerical simulations of $K_{4E,ps}$ in (4.14), n was set at 100.

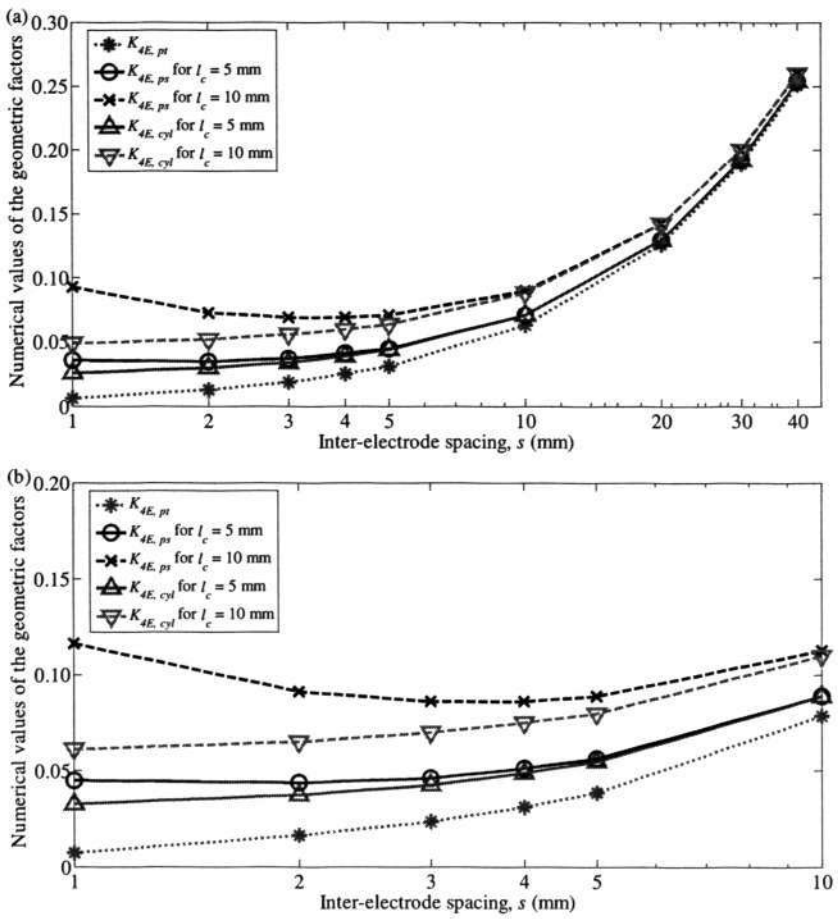

Figure 4.5 - Numerical values of the geometric factors as the inter-electrode spacing was varied from (a) 1 mm to 40 mm, and (b) 1 mm to 10 mm, with the number of segments used to compute the derived geometric factor $K_{4E,ps}$ in (4.14) set at 100.

Figure 4.5(b) showed the difference between $K_{4E,pt}$, $K_{4E,cyl}$ and $K_{4E,ps}$ at small s $(1\,\text{mm} \le s \le 10\,\text{mm})$. Although the finite dimensions of the electrode were considered in the derivation of both $K_{4E,cyl}$ and $K_{4E,ps}$, there was a significant difference in $K_{4E,cyl}$ and $K_{4E,ps}$ when s was small in comparison to l_c, e.g., $s \le 5\,\text{mm}$ and $l_c = 10\,\text{mm}$. The simulation results also showed that the numerical values of $K_{4E,pt}$, $K_{4E,cyl}$, and $K_{4E,ps}$ were close to each other when s was large in comparison to l_c, e.g., when $s \ge 5l_c$.

4.4 Measurement System

The derived geometric factor was validated through experiments conducted. The measurement system consists of three distinct components:

(i) square wave generator,

(ii) current source unit, and

(iii) voltage measurement unit.

4.4.1 Square wave generator

The functions of the square wave generator are to provide a square wave voltage to the dual Operational Transconductance Amplifier (OTA), which is a voltage-to-current converter, and to control the frequency of the current source. The operational amplifier used for the square wave generator was the LM7171 from National Semiconductor. The square wave generator was designed using a resistor-capacitor (RC) network and a Schmitt trigger. A 50% duty cycle square wave was realised and the frequency of the square wave can be varied by

varying the RC time-constant of the RC network. It is worthwhile to note that biomedical experiments were often conducted using a periodically-reversed source [5, 26, 27, 36, 41, 45] and the use of a square pulse as the measuring signal permitted detection of unusual polarisation or other effects that might have been associated with the measurement errors [26].

4.4.2 Current source unit

A square wave current was generated from the square wave voltage by means of the OTA, the LM13700N from National Semiconductor. There are two OTAs inside each LM13700N. The input of each OTA was a differential voltage and the output was a current that is determined by the ratio of the input voltage and a gain resistor. The transconductance, which is the ratio of the output current to the input differential voltage, was controlled by means of the amplifier bias current. The current I was passed through a resistor R_I of known value, and the value of I was then determined by taking the ratio of V_{R_I} and R_I, where V_{R_I} denotes the potential difference across R_I.

4.4.3 Voltage measurement unit

The voltage difference V between two electrodes which was induced by the current I injected was measured using a precision instrumentation differential amplifier with an input impedance of $10^{10}\,\Omega$, the INA128 from Burr-Brown Products, Texas Instruments. Both V and V_{R_I} were observed using an oscilloscope (LeCroy model WaveSurfer 424) as shown in Fig. 4.6, with a resolution of 8 bits. It is worthwhile to note that both V and V_{R_I} were observed with a precision of 4 significant figures.

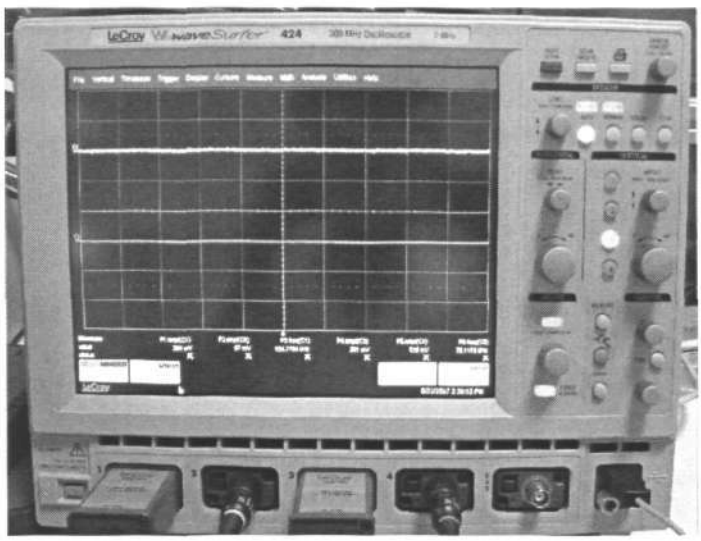

Figure 4.6 - The oscilloscope (LeCroy model WaveSurfer 424).

4.5 Experimental Set-Up

Using the measurement system, the experiments were conducted to validate the proposed geometric factor using the four-electrode method, as shown in Fig. 4.7. The functions of the various components of the measurement system have been discussed in Section 4.4.

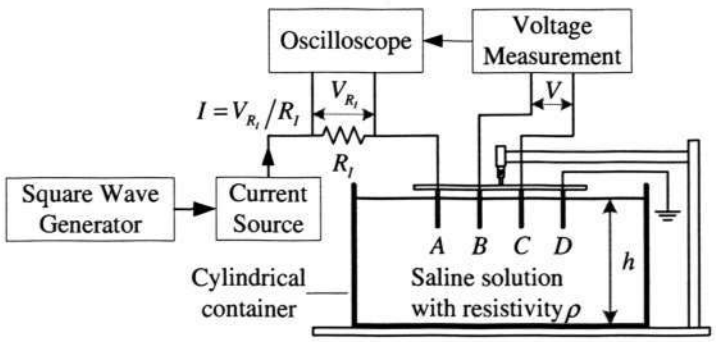

Figure 4.7 - The measurement system for experiments using the four-electrode method with slender cylindrical electrodes. The current was injected into the electrode *A* while the electrode *D* was grounded.

The test model consisted of a saline solution in a cylindrical metallic container, with a diameter of 400 mm. Saline solutions with resistivities similar to that of biological tissues have been widely used for biomedical experiments, as described in Chapter 2. The maximum s used in the experiments was 30 mm. Since the current I was only injected through the electrode A while the electrode D is grounded, as shown in Fig. 4.7, only one of the two OTAs inside the LM13700N was used to convert the square wave voltage into a constant alternating current. The magnitude of the current was determined by controlling the ratio of the input voltage and a gain resistor. The measured R was taken as the ratio of V to I and the calculated resistivities obtained using the derived geometric factor were compared with the resistivities measured using the commercial conductivity meter (YSI model EC300).

4.5.1 Saline solutions

The saline solution was prepared by mixing common salt (sodium chloride) and water. Two saline solutions, $4X$ and $4Y$, were prepared. The saline solutions were prepared in a metallic cylindrical container. The salt concentration of the saline solutions $4X$ and $4Y$ were 0.0427 mol/litre and 0.00114 mol/litre, respectively; these concentrations were chosen to approximate that of biological tissues. The resistivities of the saline solutions were measured to serve as a reference for comparison, using a commercial conductivity meter (YSI model EC300) as shown in Fig. 4.8, with a resolution of 0.01 mS/cm .

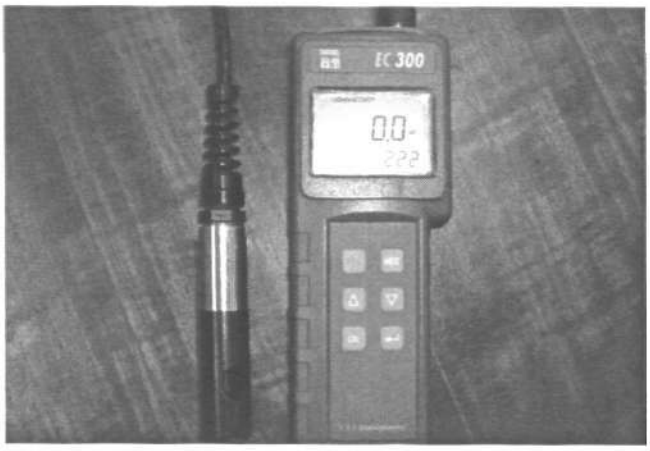

Figure 4.8 - The commercial conductivity meter (YSI model EC300).

The detailed description of the commercial conductivity meter is given in [120]. The commercial conductivity meter uses a test cell, which is located inside a probe, to measure and determines the conductivity or its inverse, the resistivity of the saline solution. For resistivity measurement using the commercial conductivity meter, the probe was immersed into the saline solution. The resistivity obtained using the conductivity meter is denoted as ρ_{cm}, where the subscript *cm* denotes conductivity meter.

The temperature of the saline solution was measured using a thermometer (Fluke model FLU65) as shown in Fig. 4.9, with a resolution of 0.1 °C. The saline solutions were measured to be 21 °C and all measurements were conducted when the saline solutions were at 21 °C. Unless otherwise stated, the depth h of the saline solution was maintained at 60 mm throughout the experiments.

Figure 4.9 - The thermometer (Fluke model FLU65).

4.5.2 Electrodes

The experiments were conducted using the four-electrode method, where four slender cylindrical Ag wires were used. The Ag wires used in the experiments were purchased from A-M Systems, Inc., Carlsborg, USA. The diameter of the Ag wire was measured using a digimatic calliper (Mitutoyo model CD-6" CsX) as shown in Fig. 4.10, with a resolution of 0.01 mm. The diameter of the Ag wire was measured to be 0.38 mm.

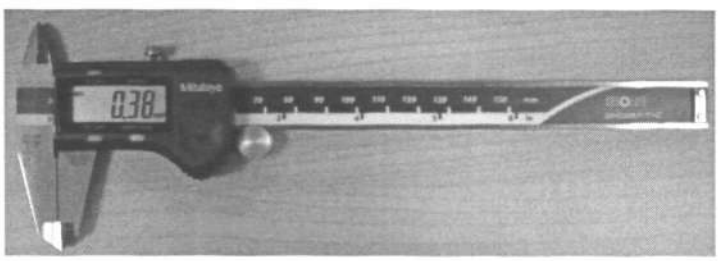

Figure 4.10 - The digimatic calliper (Mitutoyo model CD-6" CsX).

4.6 Experimental Procedures

4.6.1 Effect of the frequency on the measured resistance

Experiments were first conducted to study the effect of the frequency of the current source f on the measured resistance R with s and l_c both fixed at 5 mm. f was varied from 10 Hz to 10 kHz.

4.6.2 Effects of s, l_c and h on the measured resistance and the calculated resistivity

Subsequently, experiments were conducted to study the effects of varying s, l_c and h on the measured variable R and the calculated resistivity. With h of 60 mm, the electrodes were first fixed at a particular s and then lowered into the saline solution by rotating a micrometer. The electrodes were immersed to the required l_c, and measurements were taken for the particular s and l_c. The above procedure was repeated as s was varied from 5 mm to 30 mm, and l_c was varied from 2 mm to 5 mm.

Next, the measurements were taken with s and l_c both fixed at 5 mm and h decreased in steps of 10 mm from 60 mm. The above procedure was repeated with l_c fixed at 5 mm and s varied from 5 mm to 30 mm. The experiments described above in this section are conducted for both saline solutions 4X and 4Y.

4.7 Experimental Results and Discussions

4.7.1 Shape of typical waveforms of V and V_{R_t}

The shape of the typical voltage waveforms of V and V_{R_t} were observed using the oscilloscope as shown in Fig. 4.11. The amplitude function of the oscilloscope, which measures the difference between the upper and lower levels in two-level signals, was used to determine V and V_{R_t}. The amplitude function differs from measurement of the peak-to-peak in that the noise, overshoot, undershoot and ringing do not affect the measurement [121].

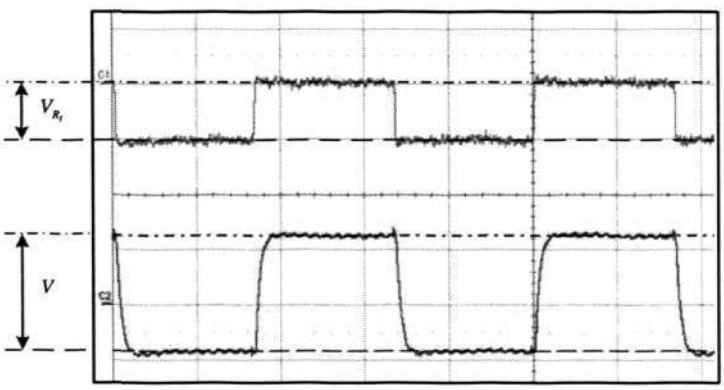

Figure 4.11 - Typical waveforms of V and V_{R_t}.

From each set of measured V and V_{R_t}, the corresponding measured resistance R was determined. ρ_{pt}, $\rho_{4E,cyl}$ and $\rho_{4E,ps}$ were calculated using $K_{4E,pt}$ in (4.1), $K_{4E,cyl}$ in (4.2) and $K_{4E,ps}$ in (4.14), respectively.

Table 4.I showed that for the range of s (5 mm and above) and l_c (2 mm and 5 mm) used in the experiments, $K_{4E,ps}$ remained relatively constant when the number of segments n used was 10 and above. Hence for the calculation of $K_{4E,ps}$ in this section, the n used was 10.

The following percentage differences are defined:

$$|\%\ \text{Diff}|_1 = \left(\frac{\rho_{4E,pt} - \rho_{cm}}{\rho_{cm}} \right) \times 100\% \tag{4.18}$$

$$|\%\ \text{Diff}|_2 = \left(\frac{\rho_{4E,cyl} - \rho_{cm}}{\rho_{cm}} \right) \times 100\% \tag{4.19}$$

$$|\%\ \text{Diff}|_3 = \left(\frac{\rho_{4E,ps} - \rho_{cm}}{\rho_{cm}} \right) \times 100\% \tag{4.20}$$

in order to determine the percentage deviation of the calculated resistivities $\rho_{4E,pt}$, $\rho_{4E,cyl}$ and $\rho_{4E,ps}$ from ρ_{cm}. Using the commercial conductivity meter, ρ_{cm} for saline solutions $4X$ and $4Y$ were found to be 2.066 $\Omega \cdot$m and 40.58 $\Omega \cdot$m, respectively.

4.7.2 Effect of the frequency on the measured resistance

As the frequency f of the current source was varied, the measured resistance R of saline solutions $4X$ and $4Y$ were tabulated in Table 4.II.

Table 4.II - Measured resistances of saline solutions $4X$ and $4Y$ as the frequency was varied.

	Saline solution $4X$	Saline solution $4Y$
f (Hz)	R (Ω)	R (Ω)
10	45.2	905
20	45.4	910
30	45.6	899
40	45.5	908
50	45.2	902
100	45.1	906
200	45.2	906
300	45.2	902
1000	45.4	908
2000	45.1	914
3000	45.5	899
5000	45.7	903
10000	45.7	907

The evaluation of the experimental results showed that the measured R remained fairly constant and was not affected by the frequency as the frequency was varied from 10 Hz to 10 kHz. Henceforth, the frequency used to investigate the effects of s, l_c and h on the measured R and the calculated ρ was 3 kHz. It is also worthwhile to note that the tissue impedance is considered mostly resistive in the low frequency range [4, 122].

4.7.3 Effects of s, l_c and h on the measured resistance and the calculated resistivity

The measured R for saline solutions 4X and 4Y, which were obtained as s and l_c were varied, were tabulated in Tables 4.III and 4.IV, respectively. From the measured R, the resistivities were calculated using the geometric factors $K_{4E,pt}$ in (4.1), $K_{4E,cyl}$ in (4.2) and $K_{4E,ps}$ in (4.14) for different combinations of s and l_c.

Table 4.III - Measured resistances and calculated resistivities of saline solution 4X.

s (mm)	l_c (mm)	R (Ω)	$\rho_{4E,pt}$ (Ω·m)	$\lvert\%\ \mathrm{Diff}\rvert_1$	$\rho_{4E,cyl}$ (Ω·m)	$\lvert\%\ \mathrm{Diff}\rvert_2$	$\rho_{4E,ps}$ (Ω·m)	$\lvert\%\ \mathrm{Diff}\rvert_3$
5	2	59.8	1.85	10.5	2.03	1.74	2.03	1.74
	3	54.9	1.70	17.7	2.03	1.74	2.03	1.74
	4	49.9	1.55	25.0	2.00	3.19	2.05	0.77
	5	45.4	1.41	31.8	2.00	3.19	2.04	1.26
	6	40.7	1.26	39.0	1.95	5.61	1.99	3.68
	7	37.3	1.16	43.9	1.94	6.10	2.01	2.71
	8	34.2	1.06	48.7	1.92	7.07	2.02	2.23
	9	31.5	0.98	52.6	1.89	8.52	2.05	0.77
	10	29.2	0.91	56.0	1.87	9.49	2.04	1.26
10	2	31.3	1.97	4.65	2.00	3.19	2.00	3.19
	3	30.8	1.94	6.10	2.03	1.74	2.03	1.74
	4	29.6	1.86	9.97	2.01	2.71	2.01	2.71
	5	28.2	1.78	13.8	2.00	3.19	2.00	3.19
20	2	16.1	2.03	1.74	2.03	1.74	2.03	1.74
	3	16.0	2.02	2.23	2.03	1.74	2.03	1.74
	4	15.7	1.98	4.16	2.03	1.74	2.03	1.74
	5	15.5	1.95	5.61	2.02	2.23	2.02	2.23
30	2	10.8	2.04	1.26	2.04	1.26	2.04	1.26
	3	10.8	2.04	1.26	2.05	0.77	2.05	0.77
	4	10.6	2.00	3.19	2.01	2.71	2.01	2.71
	5	10.6	2.00	3.19	2.04	1.26	2.04	1.26

Table 4.IV - Measured resistances and calculated resistivities of saline solution 4*Y*.

s (mm)	l_c (mm)	R (Ω)	$\rho_{4E,pt}$ ($\Omega \cdot$ m)	$\lvert\%\ \mathrm{Diff}\rvert_1$	$\rho_{4E,cyl}$ ($\Omega \cdot$ m)	$\lvert\%\ \mathrm{Diff}\rvert_2$	$\rho_{4E,ps}$ ($\Omega \cdot$ m)	$\lvert\%\ \mathrm{Diff}\rvert_3$
5	2	1160	36.0	11.3	39.5	2.66	39.5	2.66
	3	1070	33.1	18.4	39.5	2.66	39.5	2.66
	4	991	30.7	24.4	39.6	2.41	40.6	0.05
	5	886	27.5	32.2	39.0	3.89	39.9	1.68
	6	798	24.8	38.9	38.3	5.62	39.1	3.65
	7	735	22.8	43.8	38.2	5.86	39.7	2.17
	8	673	20.9	48.5	37.7	7.10	39.7	2.17
	9	617	19.1	52.9	37.0	8.82	40.1	1.18
	10	573	17.8	56.1	36.7	9.56	40.1	1.18
10	2	637	40.1	1.18	40.8	0.54	40.8	0.54
	3	604	38.0	6.36	39.8	1.92	39.8	1.92
	4	591	37.2	8.33	40.2	0.94	40.2	0.94
	5	569	35.8	11.8	40.4	0.44	40.4	0.44
20	2	318	40.1	1.18	40.1	1.18	40.1	1.18
	3	316	39.8	1.92	40.1	1.18	40.1	1.18
	4	318	40.0	1.43	41.0	1.03	41.0	1.03
	5	309	38.9	4.14	40.1	1.18	40.1	1.18
30	2	211	39.9	1.68	39.9	1.68	39.9	1.68
	3	210	39.7	2.17	39.9	1.68	39.9	1.68
	4	213	40.3	0.69	40.6	0.05	40.6	0.05
	5	214	40.4	0.44	41.0	1.03	41.0	1.03

The evaluation of the experimental results showed that when $l_c \le s$, ρ_{cm} was in good agreement with both $\rho_{4E,ps}$ and $\rho_{4E,cyl}$, with a percentage difference of less than 5%. For the range of l_c tested such that $s < l_c \le 2s$, ρ_{cm} and $\rho_{4E,ps}$ were still in good agreement, where $\lvert\%\ \mathrm{Diff}\rvert_3 < 5\%$. In contrast, $\lvert\%\ \mathrm{Diff}\rvert_2 > 5\%$. In addition, $\lvert\%\ \mathrm{Diff}\rvert_2$ increased as l_c is increased while s was fixed.

The experimental results for saline solutions 4*X* and 4*Y*, which were obtained as h was varied, were tabulated in Tables 4.V and 4.VI, respectively. From the measured R, the resistivities were calculated using the geometric factors $K_{4E,pt}$ in (4.1), $K_{4E,cyl}$ in (4.2) and $K_{4E,ps}$ in (4.14) for different combinations of s and h of the saline solutions with l_c fixed at 2 mm.

Table 4.V - Measured resistances and calculated resistivities of saline solution 4*X*.

s (mm)	h (mm)	R (Ω)	$\rho_{4E,pt}$ (Ω·m)	$\lvert\%\ \mathrm{Diff}\rvert_1$	$\rho_{4E,cyl}$ (Ω·m)	$\lvert\%\ \mathrm{Diff}\rvert_2$	$\rho_{4E,ps}$ (Ω·m)	$\lvert\%\ \mathrm{Diff}\rvert_3$
5	10	39.1	1.21	41.4	1.72	16.8	1.76	14.8
	20	43.8	1.36	34.2	1.93	6.58	1.97	4.65
	30	44.7	1.38	33.2	1.97	4.65	2.01	2.71
	40	44.9	1.39	32.7	1.98	4.16	2.02	2.23
	50	45.0	1.40	32.2	1.98	4.16	2.03	1.74
	60	44.9	1.39	32.7	1.98	4.16	2.02	2.23
10	10	17.4	1.09	47.2	1.23	40.5	1.23	40.5
	20	26.1	1.65	20.1	1.86	9.97	1.86	9.97
	30	28.1	1.77	14.4	2.00	3.19	2.00	3.19
	40	28.6	1.80	12.9	2.03	1.74	2.03	1.74
	50	28.8	1.81	12.4	2.04	1.26	2.04	1.26
	60	28.8	1.82	11.9	2.05	0.77	2.05	0.77
20	10	3.42	0.43	79.2	0.44	78.7	0.44	78.7
	20	10.1	1.28	38.0	1.32	36.1	1.32	36.1
	30	12.9	1.62	21.6	1.67	19.2	1.67	19.2
	40	14.5	1.83	11.4	1.89	8.52	1.89	8.52
	50	15.1	1.90	8.03	1.96	5.13	1.96	5.13
	60	15.4	1.94	6.10	2.00	3.19	2.00	3.19
30	10	0.42	0.08	96.1	0.08	96.1	0.08	96.1
	20	4.77	0.90	56.4	0.92	55.5	0.92	55.5
	30	7.39	1.40	32.2	1.42	31.3	1.42	31.3
	40	8.65	1.64	20.6	1.66	19.7	1.66	19.7
	50	9.91	1.87	9.49	1.90	8.03	1.90	8.03
	60	10.3	1.95	5.61	1.98	4.16	1.98	4.16

Table 4.VI - Measured resistances and calculated resistivities of saline solution 4*Y*.

s (mm)	h (mm)	R (Ω)	$\rho_{4E,pt}$ (Ω·m)	$\lvert\%\ \mathrm{Diff}\rvert_1$	$\rho_{4E,cyl}$ (Ω·m)	$\lvert\%\ \mathrm{Diff}\rvert_2$	$\rho_{4E,ps}$ (Ω·m)	$\lvert\%\ \mathrm{Diff}\rvert_3$
5	10	763	23.7	41.6	33.6	17.2	34.3	15.5
	20	880	27.3	32.7	38.7	4.63	39.6	2.41
	30	896	27.8	31.5	39.4	2.91	40.3	0.69
	40	900	27.9	31.3	39.6	2.41	40.5	0.20
	50	904	28.0	31.0	39.8	1.92	40.7	0.30
	60	901	27.9	31.3	39.6	2.41	40.5	0.20
10	10	333	21.0	48.3	23.6	41.8	23.6	41.8
	20	491	30.9	23.9	34.9	14.0	34.9	14.0
	30	547	34.4	15.2	38.8	4.39	38.8	4.39
	40	548	34.5	15.0	38.9	4.14	38.9	4.14
	50	558	35.2	13.3	39.6	2.41	39.6	2.41
	60	569	35.8	11.8	40.4	0.44	40.4	0.44
20	10	58.3	7.35	81.9	7.58	81.3	7.58	81.3
	20	188	23.7	41.6	24.4	39.9	24.4	39.9
	30	249	31.4	22.6	32.4	20.2	32.4	20.2
	40	273	34.3	15.5	35.4	12.8	35.4	12.8
	50	288	36.3	10.6	37.4	7.84	37.4	7.84
	60	306	38.6	4.88	39.8	1.92	39.8	1.92

30	10	2.58	0.49	98.8	0.50	98.8	0.50	98.8
	20	71.7	13.6	66.5	13.8	66.0	13.8	66.0
	30	128	24.2	40.4	24.5	39.6	24.5	39.6
	40	166	31.3	22.9	31.9	21.4	31.9	21.4
	50	186	35.2	13.3	35.8	11.8	35.8	11.8
	60	210	39.7	2.17	40.3	0.69	40.3	0.69

As l_c, s, and h were varied, the experimental results of the following test cases were also plotted:

Figure 4.12: $s = 5\,\text{mm}$ and $2\,\text{mm} \le l_c \le 10\,\text{mm}$.

Figure 4.13: $l_c = 5\,\text{mm}$ and $5\,\text{mm} \le s \le 30\,\text{mm}$.

Figure 4.14: $l_c = 5\,\text{mm}$ and $10\,\text{mm} \le h \le 60\,\text{mm}$ for different s (s fixed at 5 mm, 10 mm, 20 mm, and 30 mm).

As shown in Section 4.3, there was a significant difference in $K_{4E,cyl}$ and $K_{4E,ps}$ only when s was small in comparison to l_c, e.g., $s \le 5\,\text{mm}$ and $l_c = 10\,\text{mm}$. As such, the plot of $\rho_{4E,cyl}$ was included in Fig. 4.12 only. Furthermore, only the plots of resistivity for the saline solution 4*X* were presented. Similar plots were obtained for the saline solution 4*Y*.

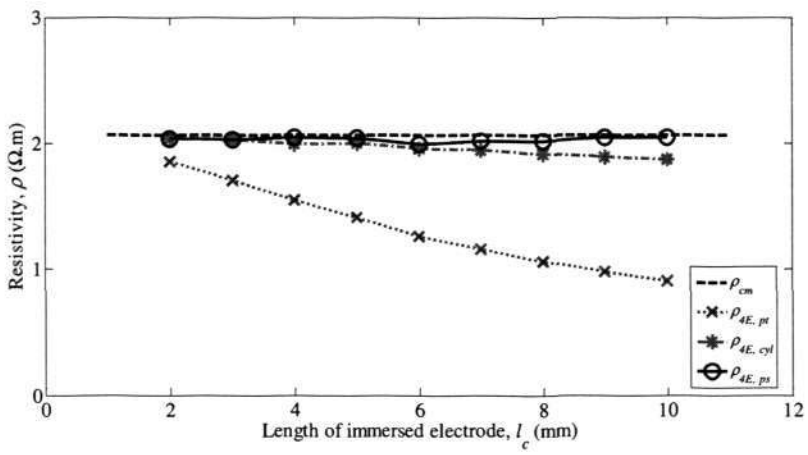

Figure 4.12 - The plots of resistivity ρ for saline solution 4*X* as $s = 5\,mm$ and $2\,mm \le l_c \le 10\,mm$. The resistivities were obtained using a commercial conductivity meter and the geometric factors $K_{4E,pt}$, $K_{4E,cyl}$, and $K_{4E,ps}$.

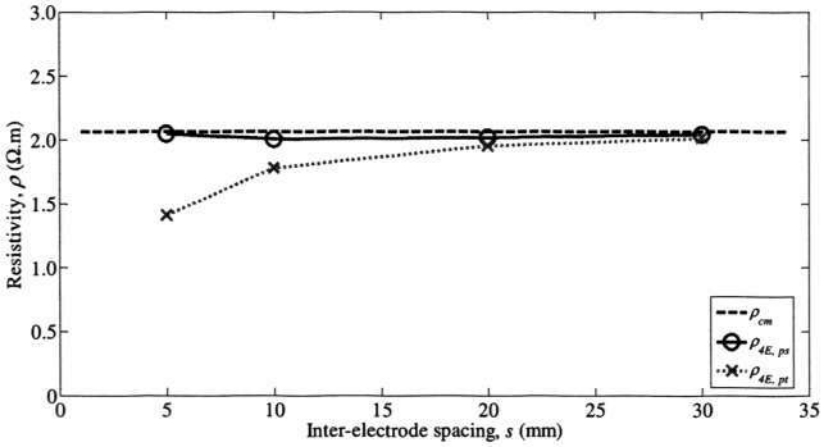

Figure 4.13 - The plots of resistivity ρ for saline solution 4X as $l_c = 5\,mm$ and $5\,mm \le s \le 30\,mm$. The resistivities were obtained using a commercial conductivity meter and the geometric factors $K_{4E,\,pt}$ and $K_{4E,\,ps}$.

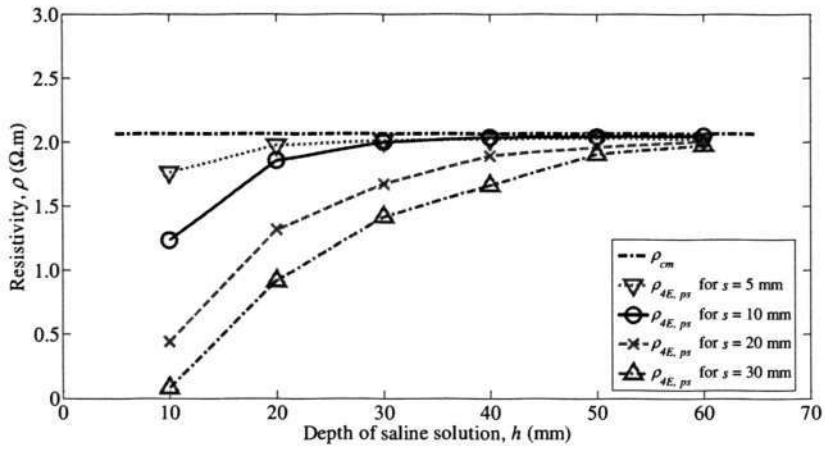

Figure 4.14 - The plots of resistivity ρ for saline solution 4X as $l_c = 5\,mm$ and $10\,mm \le h \le 60\,mm$ for different s (s fixed at 5 mm, 10 mm, 20 mm, and 30 mm). The resistivities were obtained using a commercial conductivity meter and the geometric factor $K_{4E,\,ps}$.

Our main findings from the experiments conducted on the finite-volume samples, as well as a comparison with the measurements obtained using the commercial conductivity meter, are summarised below. It is to be noted that the findings were based on the evaluation of the experimental results for which the minimum s was 5 mm.

(i) Measurements using $K_{4E,pt}$ in (4.1):

$|\%\ \text{Diff}|_1 < 5\%$ if $s \geq 5l_c$.

$|\%\ \text{Diff}|_1 > 30\%$ if $s \leq l_c$.

$\rho_{4E,pt}$ became smaller if l_c was fixed and s was decreased.

(ii) Measurements using $K_{4E,cyl}$ in (4.2):

$|\%\ \text{Diff}|_2 < 5\%$ if $s \geq l_c$.

$|\%\ \text{Diff}|_2 > 5\%$ if $s < l_c \leq 2s$.

(iii) Measurements using $K_{4E,ps}$ in (4.14):

$|\%\ \text{Diff}|_3 < 5\%$ if $s \geq l_c$.

$|\%\ \text{Diff}|_3 < 5\%$ if $s < l_c \leq 2s$. In addition, a higher accuracy in the determination of $\rho_{4E,ps}$ can be achieved by computing for $K_{4E,ps}$ in (4.14) with n selected in excess of 10. For example, when s = 3 mm and l_c = 5 mm, a higher accuracy can be achieved by selecting n = 100.

Our findings also revealed that the percentage differences in (4.18), (4.19) and (4.20) were less than 5% if $h \geq 4s$. In summary, as the measurements on many tissue samples would require small s in comparison to l_c, the derived geometric factor $K_{4E,ps}$ in (4.14) would be necessary in order to obtain an accurate measurement with a percentage difference of less than 5%. Even though resistivity measurement using the *in situ* four-electrode method has been experimentally verified to be independent of the source frequency in the low frequency range from 10 Hz to 10 kHz, the measured resistivity was still affected by the depth of the sample.

4.8 Concluding Remarks

In this chapter, a geometric factor, which was derived in the prolate spheroidal coordinates, for the *in situ* resistivity measurement of conductive media by means of four slender cylindrical electrodes has been presented. The evaluation of the experimental results showed that the resistivities of saline solutions that were obtained using the commercial conductivity meter and the derived geometric factor were both in good agreement, and a percentage error of less than 5% was achieved, even when l_c was comparable with or larger than s. In conclusion, a useful improvement to the four-electrode method for measuring tissue resistivities using the different experimental configurations and set-ups has been developed and validated through experiments. The techniques for the derivation of the geometric factor for the *in situ* resistivity measurement using the four-electrode method by means of four slender cylindrical electrodes modelled in the prolate spheroidal coordinates form the groundwork for further research work which are presented in the subsequent chapters. The work pertaining to *in situ* resistivity measurement using the four-electrode method with the geometric factor modelled in the prolate spheroidal coordinates, which is reported in this chapter, has been accepted for publication in *IEEE Trans. Biomed. Eng.* [119].

CHAPTER 5 - THE DETERMINATION OF THE PARAMETERS OF A TWO-LAYER MODEL BASED ON THE FOUR ELECTRODE RESISTIVITY MEASUREMENTS

5.1 Overview

The use of the four-electrode resistivity measurement technique in power system grounding applications is studied in this chapter. The measurement of the soil resistivity and the knowledge of the soil structure are imperative in the design and analysis of a grounding system. Although it is common for a soil to have several layers, with each layer having its own resistivity, the representation of an equivalent two-layer soil model is sufficient for designing a safe grounding system. Two-layer soil models are frequently used as an approximation of many soil structures and are, in general, accepted as a representation of non-homogeneous soil for grounding system design [19, 20]. The four-electrode [25], as shown in Fig. 4.1, is one of the more commonly used tests [19] for measuring the soil resistivity.

In the case of a two-layer soil model, the objective of the resistivity measurements and associated interpretative techniques is to establish the soil model with the parameters, ρ_1, ρ_2 and h which are the resistivity of the first and second layers and the depth of the first layer, respectively. Some of the common techniques in the interpretation of the soil resistivity for determining the parameters of a two-layer soil model are:

(i) optimization techniques based on least square-fitting criterion [15, 69, 71, 123, 124]; and

(ii) curve matching method [19, 74, 87, 125, 126].

Optimization of the soil parameters, in the least squares sense, with computer techniques have been recently used to determine the parameters of a two-layer soil model [15, 69, 71, 123, 124]. Curve matching against standard normalised theoretical curves is given in references [74, 125], where the soil parameters are determined by comparing standard curves and the curves obtained from the apparent resistivity values. The graphical method for determining the soil parameters has also been described in the literature [19, 87, 126]. Recently, Calixto [127] proposed to predict a two-layer soil model using a revised graphical method, which is a simplification of the Sunde's method [126]. The graphical method of using standard normalised curves is comparatively straightforward and its usefulness has constantly been recognised [125].

The aims of this chapter are to propose and experimentally validate a technique, which is an improvement to the conventional Sunde's graphical method for a more accurate determination of the parameters of a two-layer soil model without the need to refer to standard curves or tables. In the proposed method, the apparent resistivity at small inter-electrode spacing, denoted by s, is determined using the theoretical geometric factor (4.14) proposed in Chapter 4 [119] in order to obtain a more accurate measurement of the first layer resistivity. The results of this work, which are obtained using the proposed method, are more accurate than those obtained using the Sunde's method even in the presence of experimental errors and local finite heterogeneities. The short-coming of the Sunde's method is also presented and discussed.

This chapter is organised as follows. The two-layer soil model is described in Section 5.2. The proposed methodology for determining the parameters of a two-layer soil model is discussed in Section 5.3. The experimental set-up and procedures are described in Section 5.4. The experimental results are presented and discussed in Section 5.5. The concluding remarks are given in Section 5.6.

5.2 Theory

A two-layer soil model is shown in Fig. 5.1 where the apparent resistivities of the soil are obtained using the four-electrode method with four slender cylindrical electrodes.

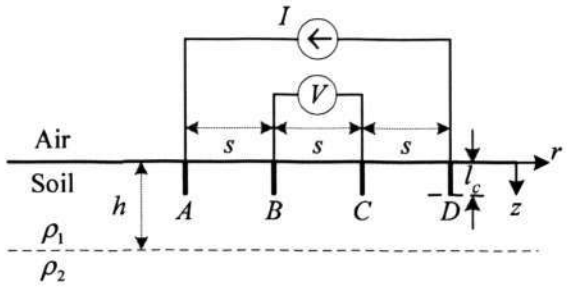

Figure 5.1 - Four-electrode method for determination of the two-layer soil model.

The current I enters at the source electrode A and leaves at the sink electrode D. Electrodes B and C are the potential electrodes. When the inter-electrode spacing s is much larger than the length of the immersed electrode l_e, the slender cylindrical electrodes are approximated as points and the apparent resistivity ρ_a is expressed as follows [20, 71, 87]:

$$\frac{\rho_a}{\rho_1} = 1 + 4\sum_{n=1}^{n=\infty}\left[\frac{k^n}{\sqrt{1+[2n(h/s)]^2}} - \frac{k^n}{\sqrt{4+[2n(h/s)]^2}}\right] \tag{5.1}$$

where ρ_1 denotes the resistivity of the first layer of the soil; h denotes the depth of the first layer of the soil; s denotes the inter-electrode spacing; and k denotes the reflection coefficient between the first and second layer of the soil. The reflection coefficient is obtained as follows [87]:

$$k = \frac{(\rho_2/\rho_1)-1}{(\rho_2/\rho_1)+1} \tag{5.2}$$

where ρ_2 denote the resistivity of the second layer of the soil.

As is already known, every theoretical standard curve for a two-layer soil model has a point of inflection, although the exact point is not easily determined by visual inspection [87]. With respect to the ρ_a curve, the point of inflection will occur when the second derivative of the ρ_a curve changes sign. The point of inflection will occur when:

$$\frac{d^2}{ds^2}\left(\frac{\rho_a}{\rho_1}\right)=0. \tag{5.3}$$

Performing the second derivative on (5.1), and letting:

$$f\left(\frac{h}{s}\right)=\frac{d^2}{ds^2}\left(\frac{\rho_a}{\rho_1}\right), \text{ then}$$

$$f(h/s)=48h^2s^{-4}\sum_{n=1}^{n=\infty}k^n n^2\left\{4^{-3/2}\left[1+n^2(h/s)^2\right]^{3/2}-\left[1+4n^2(h/s)^2\right]^{3/2}\right\}. \tag{5.4}$$

Equation (5.4) shows that for a particular two-layer soil model, there is a unique s for which the point of inflection occurs – this s can be obtained from (5.4), which is independent of the ρ_a.

5.3 Methodology

5.3.1 The Sunde's method

The Sunde's method is based on the implicit assumption that the plot of measured ρ_a versus s for a particular two-layer model matches the theoretical Sunde's curve, which is obtained using (5.1) and (5.2).

5.3.2 Determination of the resistivity of the first and second layers

Using the four-electrode method as shown in Fig. 5.1, the $\rho_{a,pt}$ is calculated using the following expression [19, 20]:

$$\rho_{a,pt} = 2\pi sR \tag{5.5}$$

where $R = V/I$. The subscripts a and pt denote apparent and point, respectively.

Equation (5.5) is not applicable when $s < 10l_c$ [20]. As described in Chapter 4, when $s < 10l_c$, the apparent resistivity, as denoted by $\rho_{a,ps}$, is more accurately determined based on the formula presented in (4.14) [119]:

$$\rho_{a,ps} = \frac{2\pi l_c R}{\left(\frac{1}{n}\right)\sum_{i=1}^{n} \ln\left[\left(\frac{\eta_{1,i}+1}{\eta_{1,i}-1}\right)\left(\frac{\eta_{2,i}-1}{\eta_{2,i}+1}\right)\right]} \tag{5.6}$$

where from (4.5) and (4.7)

$$\eta_{1,i} = \sqrt{\frac{\left(l_c^2 + s^2 + z_i^2\right) + \sqrt{\left(l_c^2 + s^2 + z_i^2\right)^2 - 4l_c^2 z_i^2}}{2l_c^2}},$$

$$\eta_{2,i} = \sqrt{\frac{\left(l_c^2 + 4s^2 + z_i^2\right) + \sqrt{\left(l_c^2 + 4s^2 + z_i^2\right)^2 - 4l_c^2 z_i^2}}{2l_c^2}} \quad \text{and} \quad z_i = \frac{l_c(2i-1)}{2n}.$$

The subscripts a and ps denote apparent and prolate spheroidal, respectively. ρ_1 and ρ_2 are to be estimated from the plots of the ρ_a curve versus s. The ρ_a curve can be extended at both ends to obtain the extreme resistivity values if the field data are insufficient. The ρ_a corresponding to the smaller and larger s is taken to be ρ_1 and ρ_2, respectively [19].

5.3.3 Determination of the depth of the first layer

Next, a point on the plot of the ρ_a curve is selected for the determination of the depth h of the first layer of the soil. In theory, if the plot of ρ_a curve matches the theoretical Sunde's curve, any point on the ρ_a curve can be used to determine h. In the proposed method, the choice of the point to be used for the determination of h is based on the following considerations:

(i) since there is not much difference in the ρ_a of the soil for different values of s near the extreme ends of the ρ_a curve, these points are avoided;

(ii) a good point for the determination of the h is the point on the ρ_a curve where the change in ρ_a is very significant – this corresponds to the point of inflection of the curve. The point of inflection is a point where the sign of the rate of change of the gradient changes – this is obtained by solving (5.4). A strong advantage of using the point of inflection is that the s at this point is independent of the ρ_a for a particular two-layer soil model.

Therefore, in this work, the proposed method for the determination of the h for a two-layer soil model is based on solving for the point of inflection of the theoretical ρ_a curve. In order to solve for the point of inflection, (5.4) is equated to zero. The parameters h, s and k cannot be zero values for a two-layer soil model with different resistivity values; therefore, in order for (5.4) to be equal to zero, there exists a unique combination of h/s for every value of k such that (5.4) is equal to zero. The h is determined as follows. Firstly, the s at the point of inflection is found by determining the turning point of the gradient of the measured ρ_a curve. Next, the particular combination of h/s for a specific value of reflection coefficient k, is solved by searching for the roots of (5.4). Now that the particular s and the factor h/s at which the point of inflection occurs have been determined, the h can be obtained.

5.3.4 Procedure of the proposed method

The steps for determining the parameters of a two-layer soil model are described below:

(i) user input the resistivity data obtained from the field tests;

(ii) a best-fit curve of measured ρ_a of the soil versus s is obtained and plotted using the field data;

(iii) ρ_1 and ρ_2 are estimated from the two ends of the plot of ρ_a versus s;

(iv) k is determined using (5.2);

(v) s at the point of inflection is determined from the plot in step (ii);

(vi) h/s where the point of inflection occurs is determined from (5.4); and

(vii) h is obtained.

The above procedures for the determination of the parameters were implemented using the computer simulation software MATLAB [128] and the curve fitting software CurveExpert [129]. From the resistivity data inputted by the user in step (i), the curve fitting software CurveExpert is used to fit the resistivity data. The CurveExpert program sifts through all the possible curve fit and the best ranked fit is chosen as the best-fit curve

5.4 Experimental Set-Up

Two sets of experiments, 5*X* and 5*Y*, were conducted in order to replicate for soil conditions with two different values of k; i.e., negative and positive values of k, which correspond to situations where $\rho_1 > \rho_2$ and $\rho_1 < \rho_2$, respectively. Using the measurement system, the experiments were conducted to validate the proposed measurement technique using the four-

electrode method, as shown in Fig. 5.2. The functions of the various components of the measurement system have been discussed in Section 4.4.

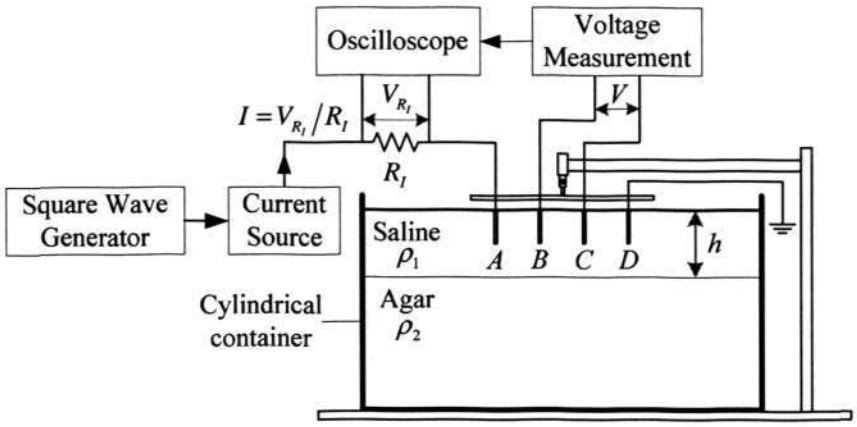

Figure 5.2 - The experimental set-up. The upper layer was a saline solution with resistivity ρ_1, while the lower layer was agar with resistivity ρ_2. (Note: The figure was not drawn to scale).

The test model consisted of a first layer of saline solution and a second layer of agar in a metallic tank, with the following dimensions: 600 mm (length) by 300 mm (breadth) by 360mm (depth). The maximum s used in the experiments was 100 mm. Since the current I was only injected through the electrode A while the electrode D was grounded, as shown in Fig. 5.2, only one of the two OTAs inside the LM13700N was used to convert the square wave voltage into a constant alternating current. The magnitude of the current was determined by controlling the ratio of the input voltage and a gain resistor. The frequency of the current was set at 3 kHz.

5.4.1 Electrodes

The experiments were conducted using the four-electrode method, where four Ag wires were used. The Ag wires were purchased from A-M Systems, Inc., Carlsborg, USA. The diameter

of the Ag wire was measured using a digimatic calliper (Mitutoyo model CD-6" CsX), which is shown in Fig.4.10, and found to be 0.38 mm. In the experiments, l_c of 2 mm was used.

5.4.2 Preparation of the agar and the saline solution

The second layer of the agar was prepared by mixing agar powder, common salt and water. Adjusting the concentration of the salt in the agar controlled the resistivity of the agar mixture. The agar mixture was then cooked, allowed to be cooled and hardened in the metallic tank. The first layer of the saline solution was prepared by mixing common salt and water. The salt concentration of the saline solutions for experiments 5*X* and 5*Y* were prepared so as to conduct the experiments for negative and positive values of k, respectively. The resistivity of the agar ρ_2 was measured using the four-electrode method. The resistivity of the saline solution ρ_1 was measured using a commercial conductivity meter (YSI model EC300), which is shown in Fig. 4.8. The depth of the agar layer was fixed at 260 mm. The depth of the first layer of the saline solution h was maintained at 20 mm throughout the experiments. Using a thermometer (Fluke model FLU65), which is shown in Fig. 4.9, the temperature of the saline solution was measured to be 21 °C. All measurements were conducted when the saline solutions were at 21 °C.

The experiments were conducted with and without local finite heterogeneities in the first layer. The heterogeneities were introduced by placing pebbles, which were completely submerged in the saline solutions, on the surface of the agar layer. In Experiment 5*X*, two sets of tests were conducted, i.e., in the absence and presence of the local heterogeneities, which were denoted as 5*X1* and 5*X2*, respectively. Similarly, two sets of tests were conducted in Experiment 5*Y*, i.e., in the absence and presence of the local heterogeneities, which were denoted as 5*Y1* and 5*Y2*, respectively.

5.5 Results and Discussions

5.5.1 Measured parameters

The measured parameters for both the experiments $5X$ and $5Y$ were tabulated in Table 5.I. ρ_1 of the saline solution was determined using the commercial conductivity meter. ρ_2 of the agar was determined using (4.1), where s and l_c were 20 mm and 2 mm, respectively.

Table 5.I - Measured parameters for experiments $5X$ $(\rho_1 > \rho_2)$ and $5Y$ $(\rho_1 < \rho_2)$.

	Experiment $5X$	Experiment $5Y$
ρ_1 $(\Omega \cdot \mathrm{m})$	87.2	30.0
ρ_2 $(\Omega \cdot \mathrm{m})$	58.1	61.6
h (mm)	20.0	20.0

5.5.2 Measured resistances

The measured resistance R was obtained as s was varied for all the experiments conducted, and the results were tabulated in Table 5.II.

Table 5.II - Measured resistances R for experiments $5X$ $(\rho_1 > \rho_2)$ and $5Y$ $(\rho_1 < \rho_2)$ as the inter-electrode spacing is varied from 5 mm to 100 mm.

	Measured resistances R $(\mathrm{k}\Omega)$			
s (mm)	*5X1*	*5X2*	*5Y1*	*5Y2*
5	2.56	2.58	0.88	0.91
10	1.36	1.38	0.49	0.50
15	0.90	0.92	0.34	0.35
20	0.64	0.65	0.28	0.29
25	0.51	0.51	0.27	0.27
30	0.41	0.42	0.24	0.24
40	0.29	0.29	0.20	0.20
50	0.21	0.22	0.17	0.17
60	0.17	0.18	0.15	0.16
70	0.13	0.15	0.14	0.14
80	0.12	0.13	0.12	0.12
90	0.10	0.11	0.11	0.11
100	0.09	0.09	0.10	0.10

From the measured R shown in Table 5.II, the corresponding calculated ρ_a were tabulated in Table 5.III. The apparent resistivities $\rho_{a,pt}$ and $\rho_{a,ps}$ were calculated using (5.5) and (5.6), respectively.

Table 5.III - Calculated resistivities $\rho_{a,pt}$ and $\rho_{a,ps}$ were calculated using (5.5) and (5.6), respectively, for experiments $5X$ $(\rho_1 > \rho_2)$ and $5Y$ $(\rho_1 < \rho_2)$.

	5X1		5X2		5Y1		5Y2	
s (mm)	$\rho_{a,pt}$ $(\Omega\cdot\mathrm{m})$	$\rho_{a,ps}$ $(\Omega\cdot\mathrm{m})$	$\rho_{a,pt}$ $(\Omega\cdot\mathrm{m})$	$\rho_{a,ps}$ $(\Omega\cdot\mathrm{m})$	$\rho_{a,pt}$ $(\Omega\cdot\mathrm{m})$	$\rho_{a,ps}$ $(\Omega\cdot\mathrm{m})$	$\rho_{a,pt}$ $(\Omega\cdot\mathrm{m})$	$\rho_{a,ps}$ $(\Omega\cdot\mathrm{m})$
5	79.3	87.0	79.9	87.6	27.3	30.0	28.3	31.0
10	85.5	86.9	86.8	88.2	30.7	31.2	31.2	31.7
15	84.5	85.4	86.9	87.8	31.9	32.2	33.0	33.3
20	80.9	80.9	82.2	82.2	34.7	34.7	36.8	36.8
25	79.3	79.8	79.3	79.8	42.0	42.2	42.2	42.5
30	76.7	76.7	78.7	78.7	44.8	44.8	44.9	44.9
40	71.4	71.4	72.5	72.5	49.0	49.0	49.2	49.2
50	66.4	66.6	67.9	68.1	52.2	52.4	52.9	53.1
60	64.2	64.2	67.6	67.6	58.0	58.0	58.7	58.7
70	58.7	58.7	63.6	63.6	59.7	59.7	60.2	60.2
80	59.5	59.5	62.6	62.6	60.6	60.6	59.1	59.1
90	58.1	58.1	60.9	60.9	60.5	60.5	60.3	60.3
100	58.2	58.2	59.2	59.3	61.6	61.7	61.3	61.4

5.5.3 Estimation of the resistivities of the first and second layers

Using the curve-fitting program, the best-fit curve of ρ_a versus s was obtained. ρ_1 and ρ_2 of the two-layer model were estimated from the two extreme ends of the best-fit curve, i.e., ρ_1 was estimated at $s = 0$ mm and ρ_2 was estimated at $s = 500$ mm. It is to be noted that there was no significant change in the value of ρ_a from $s = 500$ mm onwards. The estimated resistivities for both the experiments $5X$ and $5Y$ based on the ρ_a calculated using (5.5) and (5.6), were given in Tables 5.IV and 5.V, respectively. With $l_c = 2$ mm and $10l_c = 20$ mm, the readings for $s < 20$ mm were not included when (5.5) was used.

Table 5.IV - Estimated resistivities of the first and second layer based on apparent resistivities calculated using (5.5) only.

	5X1	*5X2*	*5Y1*	*5Y2*
ρ_1 $(\Omega \cdot \mathrm{m})$	82.6	98.7	16.4	21.9
ρ_2 $(\Omega \cdot \mathrm{m})$	50.8	49.7	62.6	61.9

Table 5.V - Estimated resistivities of the first and second layer based on apparent resistivities calculated using (5.6) only.

	5X1	*5X2*	*5Y1*	*5Y2*
ρ_1 $(\Omega \cdot \mathrm{m})$	87.0	88.4	29.4	30.4
ρ_2 $(\Omega \cdot \mathrm{m})$	52.0	53.5	63.9	63.3

The results in Tables 5.IV and 5.V showed that when the resistivities were estimated based on ρ_a calculated using (5.6) instead of (5.5), a better estimate of the resistivities was obtained. Henceforth, the ρ_a was calculated using (5.6). Only the plots of ρ_a versus s for experiments *5X2* and *5Y2* were shown in Figs. 5.3(a) and 5.3(b), respectively. It is to be noted that the plots of ρ_a versus s for experiments *5X1* and *5Y1* were similar in shape to Figs. 5.3(a) and 5.3(b), respectively.

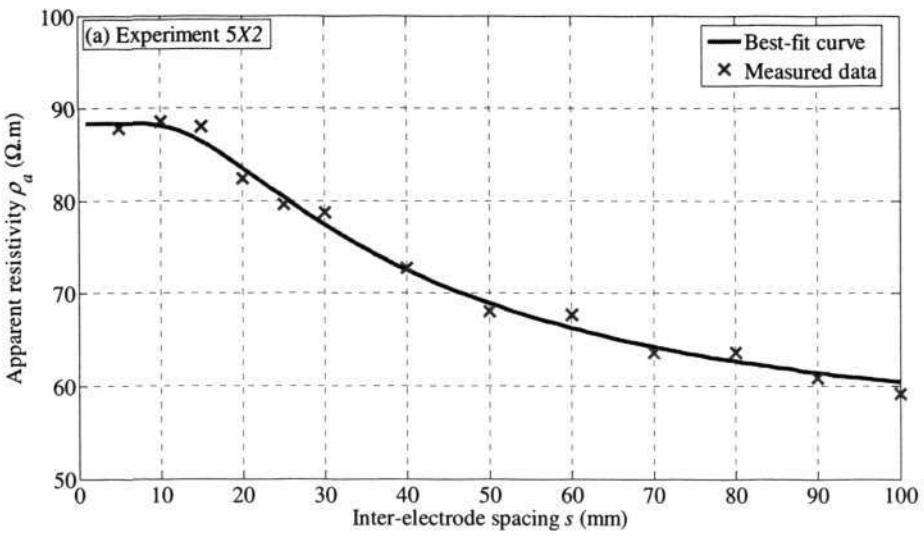

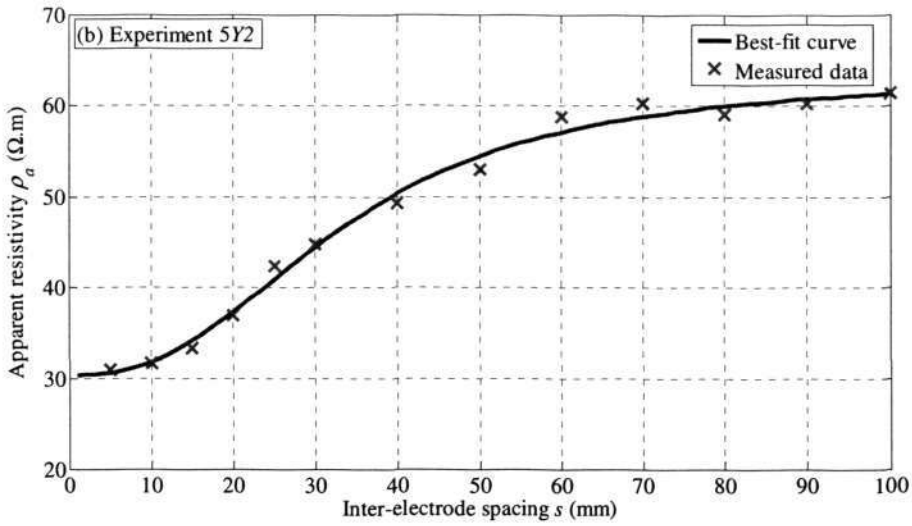

Figure 5.3 - The plots of the measured apparent resistivity versus inter-electrode for experiments (a) 5*X*2 and (b) 5*Y*2.

5.5.4 Estimation of the depth of the first layer using the Sunde's method

The depth h of the first layer of the two-layer model pertaining to experiments 5*X* and 5*Y* were estimated using the Sunde's method as described in IEEE Std [19]. The ratio of ρ_2/ρ_1 for experiments 5*X*2 and 5*Y*2 were determined and the Sunde's curves, which correspond to the specific ratio of ρ_2/ρ_1, were generated using (5.1) and shown in Fig. 5.4. The number of terms n in (5.1) that was used to generate the Sunde's curve was 100.

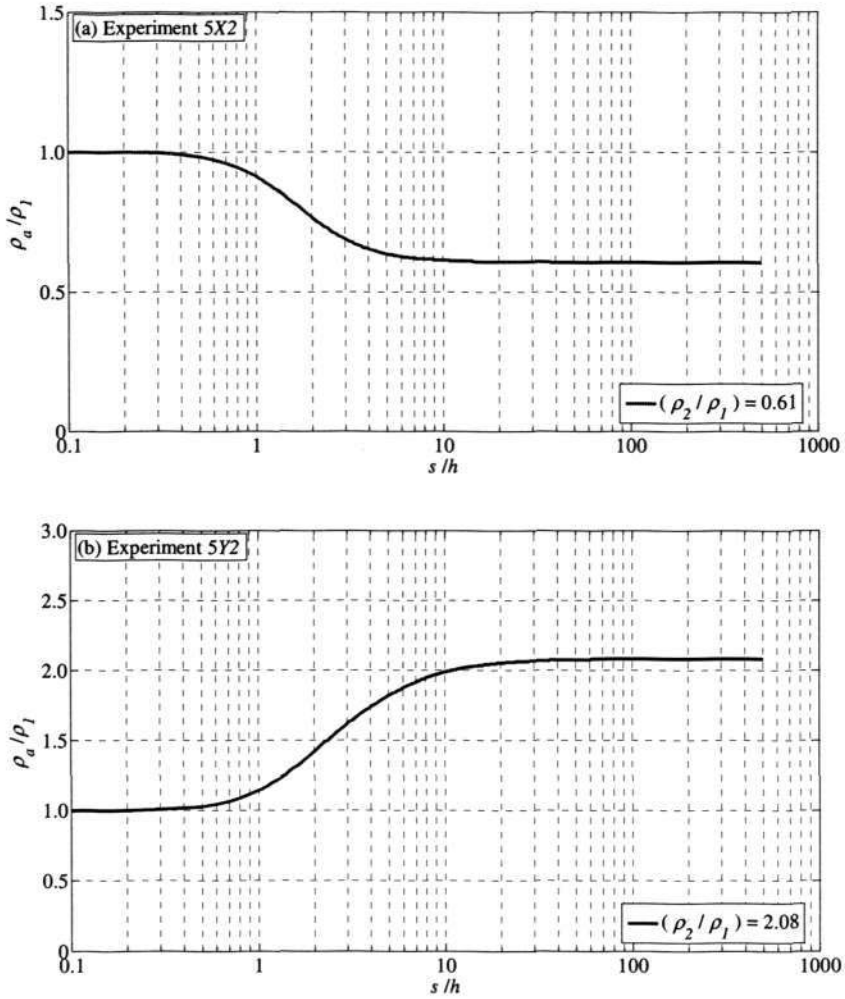

Figure 5.4 - Sunde's curve for the case where ρ_2/ρ_1 was (a) 0.61 and (b) 2.08.

According to the instructions given in IEEE Standard [19], any value of ρ_a/ρ_1 on the y-axis within the sloped region of the Sunde's curve can be selected to estimate the h of the first layer. The effect of the different selected values of ρ_a/ρ_1 on the estimated h for experiments 5*X* and 5*Y* were shown in Table 5.VI. It is obvious from the results shown in Table 5.VI that the choice of ρ_a/ρ_1 affected the estimate of the h in the Sunde's method. In addition, the estimated h was not in good agreement with the measured h of 20 mm.

Table 5.VI - Effect of ρ_a/ρ_1 on estimated h for experiments $5X$ $(\rho_1 > \rho_2)$ and $5Y$ $(\rho_1 < \rho_2)$ using the Sunde's method. Measured h was 20 mm.

Experiment	ρ_a/ρ_1	s/h	ρ_a $(\Omega \cdot \mathrm{m})$	s (mm)	h (mm)
5X1	0.65	3.81	56.6	103	27.1
	0.75	2.09	65.3	54.2	25.9
	0.85	1.35	74.0	33.6	24.9
	0.95	0.75	82.7	19.9	26.4
5X2	0.65	4.11	57.5	131	31.8
	0.75	2.15	66.3	60.1	28.0
	0.85	1.38	75.2	34.8	25.3
	0.95	0.76	84.0	19.3	25.4
5Y1	1.10	0.82	32.3	13.3	16.1
	1.25	1.32	36.7	20.3	15.4
	1.50	2.22	44.1	30.5	13.7
	1.75	3.67	51.4	43.1	11.8
5Y2	1.10	0.84	33.4	13.6	16.1
	1.25	1.37	38.0	20.9	15.2
	1.50	2.37	45.6	31.7	13.4
	1.75	4.14	53.2	46.4	11.2

5.5.5 Short-coming of the Sunde's method

The results above showed that the various estimates of h using the Sunde's method were not in good agreement with the measured h. An investigation into the cause of these discrepancies is in order. The plots of the measured and theoretical ρ_a versus s for both the experiments *5X2* and *5Y2* were compared as shown in Fig. 5.5. The theoretical model was obtained using (5.1) based on the measured h and the estimated ρ_1 and ρ_2.

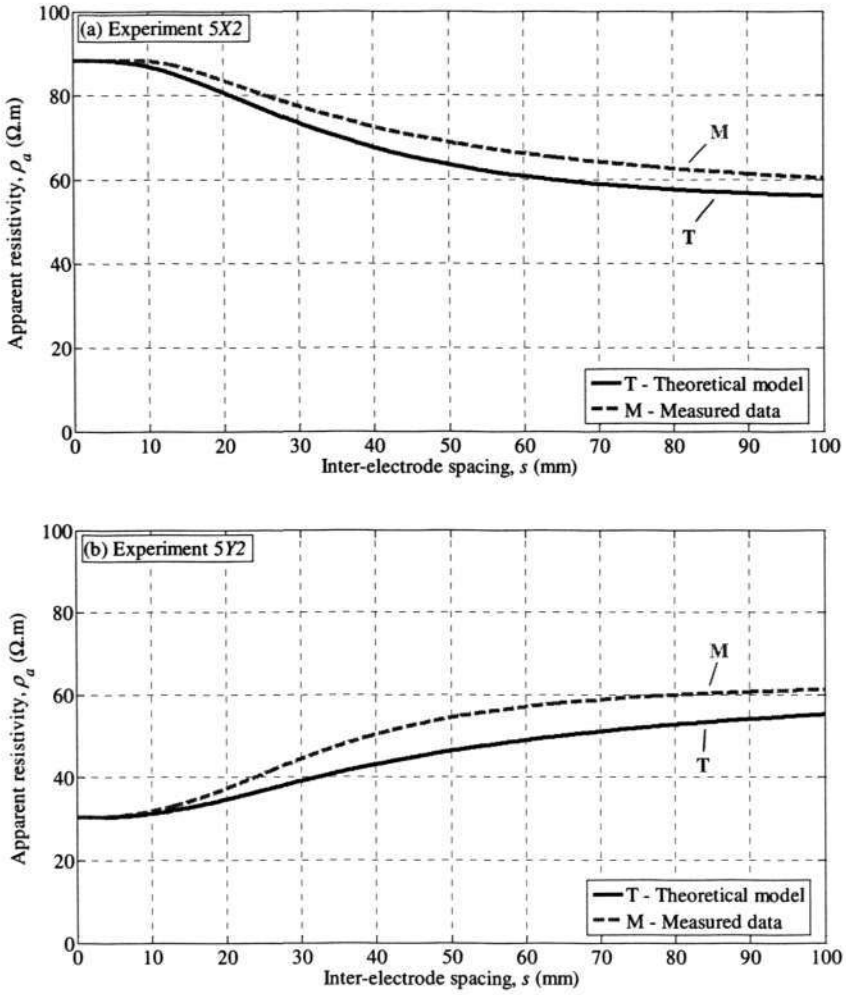

Figure 5.5 - The plots of measured and theoretical apparent resistivity versus inter-electrode spacing for experiments (a) 5*X*2 and (b) 5*Y*2.

Figure 5.5 showed that the plots of measured and theoretical ρ_a versus s do not match. Since the two plots do not match, it follows that the estimate of h cannot be accurate and different selected values of ρ_a/ρ_1 will lead to different estimated values of the h.

5.5.6 Point of inflection

Even though the plots of measured and theoretical ρ_a versus s do not match, it was noted that the s at which the point of inflection of the two plots occurred to be in good agreement. The s where the point of inflection occurs for the four cases under consideration was given in Table 5.VII. The s at the point of inflection of the plots of measured and theoretical ρ_a versus s was used in the proposed method for the estimation of the h.

Table 5.VII - Inter-electrode spacing where the point of inflection occurred

	5X1	*5X2*	*5Y1*	*5Y2*
Theoretical Model	22.0	22.0	25.0	24.8
Measured Data	21.0	21.9	24.5	24.1

5.5.7 Estimation of the depth of the first layer using the proposed method

From the estimate of ρ_1 and ρ_2, the reflection coefficient k was determined using (5.2) for all the cases in the experiments $5X$ and $5Y$, and the values were given in Table 5.VIII. Using the value of k determined, the unique combination of the factor h/s where the point of inflection occurs was determined by solving (5.4) and the results were tabulated in Table 5.VIII. The number of terms n that was used to solve (5.4) was 100. Using the calculated theoretical factor h/s and the s, which was obtained from the measured data where the point of inflection occurs, the depth h was then estimated as shown in Table 5.VIII.

Table 5.VIII - Estimated h using the proposed method. Measured h was 20 mm.

	5X1	*5X2*	*5Y1*	*5Y2*
k	-0.25	-0.25	0.37	0.35
h/s	0.91	0.91	0.80	0.81
s (mm)	21.0	21.9	24.5	24.1
h (mm)	19.1	19.9	19.6	19.5

The h, which was estimated using the proposed method, was found to be in good agreement with the measured h of 20 mm. Therefore, based on the proposed method, a good estimate of ρ_1, ρ_2 and h, which was more accurate than those obtained using the Sunde's method even in the presence of experimental errors and local finite heterogeneities was obtained.

5.6 Concluding Remarks

A technique for the determination of the parameters of a two-layer soil model has been presented. Experiments were conducted on scale model tests in an electrolytic tank where the resistivities of the saline solutions and the agar were chosen to approximate that of the soil. The evaluation of the experimental results validated the proposed technique for the determination of the parameters for a two-layer soil model. The proposed technique allows the user to determine a more accurate two-layer model compared to the Sunde's method.

CHAPTER 6 - RESISTIVITY MEASUREMENT OF SMALL-VOLUME SAMPLES USING TWO SLENDER CYLINDRICAL ELECTRODES

6.1 Overview

In this chapter, the use of the two-electrode method for resistivity measurement in biomedical applications is studied. Resistivity measurement of conductive media obtained using the four-electrode method has been known to be affected by the small sample size or the effect of the boundary, where such small-volume samples are often encountered in biomedical applications. Steendijk *et al.* reported that when the thickness of the sample was more than 1.95 times the inter-electrode spacing, the difference between the measured apparent resistivity and the actual resistivity of the medium was less than 10% [22]. In a study by Kun and Peura, it was reported that the measured resistivity of the tissue decreased as the thickness of the tissue was decreased while the inter-electrode spacing was maintained constant [4]. In addition, it was reported in [119] and Chapter 4 that the resistivity measured using the four-electrode method decreased when the sample thickness was reduced.

The resistivities of the biological tissue have been measured either *in vivo* [12, 22, 26, 29, 47, 130] or *in vitro* [4, 5, 27, 28, 36, 40, 41, 43, 45] using the four-electrode method [25], where plunge or needle electrodes have often been used for the resistivity measurements [26, 28, 47]. The plunge or needle electrode is similar to a cylindrical rod electrode which has a circumference that is small in proportion to its length. Alternatively, the two-electrode method has the advantage of being a smaller electrochemical sensor [84], despite it being affected by the effect of the electrode polarisation [131, 132]. As a result of the smaller sensor size of the

two-electrode method and since the four-electrode method requires a large sample size for the resistivity measurement, the miniaturization of the two-electrode method for the resistivity measurement of small-volume sample in biomedical application is much more feasible. However, the use of the two-electrode method depends largely on how the effect of the electrode polarisation, which results in electrode-electrolyte interface impedances [133] in series with the bulk resistance of the electrolyte, is controlled. The effect of the electrode polarisation is due to the build-up of the charges on the surfaces off the electrodes and the creation of the electrical double layers [86, 134, 135]. The polarisation impedance is known to be a function of the excitation frequency, current density, geometry of the electrode-electrolyte interface, electrode material, and electrolyte concentration [136]. Recently, the polarisation impedance behaviour of several common polarizable metals in diluted sodium chloride solution has been characterised as a reference to calculate the electrode polarisation impedance [84]. In [84], it was reported that the materials silver, gold, platinum, aluminium and stainless-steel were affected by the effect of the electrode polarisation.

The effect of the electrode polarisation is significant and its correction is a major complexity encountered in the measurements of the conductive biological samples [86]. An excellent review of the techniques used to correct the effect of the electrode polarisation is given in [86]. Various approaches used to control the electrode polarisation effect have been described [137, 138] and silver-silver chloride (Ag/AgCl) electrodes, which are relatively non-polarizable electrodes [75, 133], can also be used to minimize this effect. Ag/AgCl electrodes have small charge transfer resistance due to its large exchange current density. Hence, when current is injected using the Ag/AgCl electrodes, current is transferred across the electrode-electrolyte interface easily and small amount of voltage is dropped across the interface [133]. Some of the other techniques for the correction of the electrode polarisation effect include the distance variation technique [139-141], which included the use of the variable-length conductivity cell [142-145], and conducting measurements using the four-electrode method

[146-148]. The effect of the polarisation impedance can also be controlled by measuring over a range of frequencies, plotting a graph of the resistance as a function of the inverse frequency and extrapolating to obtain the bulk resistance at infinite frequency [138].

The contributions of this chapter are the theoretical derivation and the experimental validation of new geometric factors, derived in the cylindrical and the prolate spheroidal coordinates, for resistivity measurement using two slender cylindrical electrodes. The theoretical geometric factors took the shape and dimensions of the electrodes and the spacing between them into account in order to obtain the dependence of the resistance between the electrodes on the resistivity of the medium. Experiments were conducted to validate the theoretical geometric factors using saline solutions in an insulator container and an electronic circuit. As noted in Chapter 2, experiments pertaining to biomedical analysis and applications were commonly conducted using the saline solutions. Using relatively non-polarizable Ag/AgCl electrodes and by conducting the experiments at an excitation frequency of 3 kHz, the problems associated with electrode polarisation were minimised. The evaluation of the experimental results that will be presented later in this chapter showed that the resistivities of the saline solutions obtained using the derived geometric factors and those obtained using a commercial conductivity meter were both in good agreement even when the inter-electrode spacing, the length of the immersed electrode or the depth of the sample was varied. The two-electrode method for the resistivity measurement described above was also shown to be independent of the current density of the source of excitation. In addition, the measurements remained relatively stable when tests are conducted over a duration of one (1) hour. The temperature dependence of the measured resistivity of the saline solution using the two-electrode method was also presented. This two-electrode method also produced consistent results even at small sample depths thereby making it suitable for biomedical applications where small-volume samples are often encountered.

This chapter is organised as follows. Novel geometric factors for the resistivity measurement using the two-electrode method are derived in the prolate spheroidal and the cylindrical coordinates in Section 6.2. The numerical simulations results conducted using the derived geometric factors are shown in Section 6.3. The experimental set-up and procedures are described in sections 6.4 and 6.5, respectively. The experimental results are presented and discussed in Section 6.6. The concluding remarks are given in Section 6.7.

6.2 Theoretical Derivation

6.2.1 Polarisation impedance

In the two-electrode method shown in Fig. 6.1, two slender cylindrical electrodes are immersed in the conductive medium, both the conduction and the displacement currents flow between the electrode and the medium. It is to be noted that throughout this chapter, d and l_c denotes the inter-electrode spacing and the length of the immersed electrode, respectively.

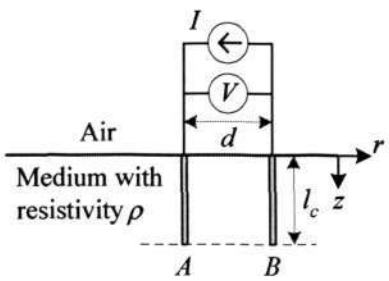

Figure 6.1 - Two-electrode method for *in situ* resistivity measurement using slender cylindrical electrodes.

A simplified equivalent circuit model, which can be used to represent the flow of such currents, is shown in Fig. 6.2. In general, the polarisation impedance of the electrode-electrolyte interface comprises a faradaic impedance Z_f in parallel with a capacitance C_d

whereas the bulk electrolyte resistance is represented by R_Ω. Z_f can be represented by a charge transfer resistance R_{ct} in series with the mass transfer impedance Z_w, also known as Warburg impedance [133].

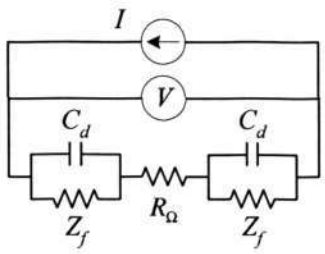

Figure 6.2 - Simplified equivalent circuit model.

R_{ct} is resistance encountered by charge leakage which took place at the electrode-electrolyte interface, as a result of the electrochemical reaction taking place at the interface [133]. Z_w is an impedance to current flow through the electrode system at low frequencies [133]. When an electrode is immersed in an electrolyte, a potential is induced as a result of the unequal distribution of charges across the electrode-electrolyte interface [133]. There will be a layer of charge at the surface of the electrode and another equal and opposite charge just inside the electrolyte, which results in the 'double layer' of charge that exists at the electrode-electrolyte interface. The 'double layer' of charge behaves much like a capacitor represented by C_d [108, 133, 149].

Some of the factors that affect the polarisation impedance include the electrode area, the excitation frequency and the current density [14]. The magnitude of the series resistance decreases and that of the capacitance increases with increasing electrode area. A high electrode-electrolyte capacitance value is indicative of a low reactive component for the polarisation impedance. The series-equivalent capacitance decreases with increasing frequency. The capacitance of an electrode-electrolyte interface varies inversely with the square root of the frequency. For a given frequency, the equivalent resistance decreases and

the capacitance increases as current density is increased. The largest change occurs in the low-frequency region. Therefore, the low-frequency magnitude of the series impedance of an electrode-electrolyte interface decreases markedly by an increase in current density. It is worthwhile to note that the model for the representation of the electrode-electrolyte interface is still being studied by researchers and other models for the interface can be found in [14].

In the case of an ideal polarizable electrode, no charge transfer can occur between the electrode-electrolyte interface [108]. Examples of nearly ideal polarised electrodes are gold and platinum [150]. Stainless steel and aluminium electrode materials are also polarizable [84, 136]. In order to minimize chemical reactions associated with the conduction currents, nearly polarised electrodes are often utilised for conductivity measurements with alternating current excitations to generate a displacement current across the electrode-electrolyte interface. However, the effect of the polarisation impedance, along with others, continues to affect the results of conductivity measurements [150].

On the other hand, an ideal non-polarizable electrode has an electrode potential that does not change upon the passage of current within a certain range. When two ideal non-polarizable electrodes are used in the two-electrode method, the characteristics of the direct current versus potential across the electrodes would look like that of a pure resistance because the only limitation on the current flow is imposed by the resistance of the medium between the electrodes [108], which depends on the geometric factor and the resistivity of the medium. Relatively non-polarizable electrodes such as Ag/AgCl electrodes [75, 133] have been widely used for biomedical purposes, in particular microfluidics applications [151-156]. When using a pair of chlorided electrodes to pass currents through an electrolyte solution, as the current flows, the chloride ions will gather at the positive electrode (the anode), but the chloride ions will be depleted from the negative electrode (the cathode) [157]. At high frequencies, the polarisation impedance is very small and the charge-transfer resistance is effectively shorted

out, i.e., the measured value of R, $R=(V/I)$ represents the resistance of the electrolyte solution between the two electrodes, i.e., R_Ω.

6.2.2 Relationship between the measured resistance, the electrical resistivity and the geometric factor in the cylindrical coordinates

The theoretical geometric factor for resistivity measurement using the two-electrode method with slender cylindrical electrodes modelled using the cylindrical coordinates is shown hereafter. Consider the two-electrode method by means of two slender cylindrical electrodes, as shown in Fig. 6.3. The current source and sink electrodes, A and B, respectively, are modelled using the cylindrical coordinates.

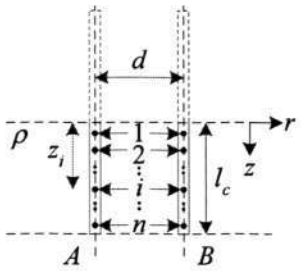

Figure 6.3 - Application of the image method for currents to the current source and sink electrodes A and B, respectively, with the electrodes modelled in the cylindrical coordinates.

6.2.2.1 Potential of a point

Consider a slender cylindrical source electrode with current I in a conductive, homogeneous, isotropic and semi-infinite medium. The potential of a point P in the conductive medium that is induced by a point current source, derived in the cylindrical coordinates, is derived in (3.26) and shown below:

$$V(r,z)=\frac{\rho I}{4\pi}\left[\frac{1}{\sqrt{r^2+(z-z_s)^2}}+\frac{1}{\sqrt{r^2+(z+z_s)^2}}\right]. \tag{6.1}$$

6.2.2.2 *Potential of a point due to a current emanating from a slender cylindrical electrode*

Next, consider one slender cylindrical electrode with known dimensions as a current source. The source electrode is made up of infinitesimal current sources. It is assumed that the current density along the current carrying electrodes is uniform and symmetrical with respect to the axis of the electrode. Making use of the potential of a point shown in (6.1), the principle of superposition and neglecting electrode effects, the potential at $P(r,z)$ is the sum of the potentials resulting from all the sources and their respective images; this potential is expressed as follow:

$$\begin{aligned} V &= \int_0^{l_c} \frac{\rho I}{4\pi l_c}\left[\frac{1}{\sqrt{r^2+(z-z_s)^2}}+\frac{1}{r^2+\sqrt{(z+z_s)^2}}\right]dz_s \\ &= \frac{\rho I}{4\pi l_c}\ln\left[\frac{(z+l_c)+\sqrt{(z+l_c)^2+r^2}}{(z-l_c)+\sqrt{(z-l_c)^2+r^2}}\right]. \end{aligned} \tag{6.2}$$

6.2.2.3 *Self-potential*

With reference to Fig. 6.3, making use of (6.2) and let $r = r_c$, where r_c is the radius of the slender cylindrical electrode, the potential of a point on the electrode *A* due to a current source and its images at the electrode *A*, denoted by $V_{1,A}$, is:

$$V_{1,A} = \frac{\rho I}{4\pi l_c}\ln\left[\frac{(z_1+l_c)+\sqrt{(z_1+l_c)^2+r_c^2}}{(z_1-l_c)+\sqrt{(z_1-l_c)^2+r_c^2}}\right]. \tag{6.3}$$

The self-potential of the electrode A due to current source and its images at the electrode A, denoted by $V_{A,A}$, is then obtained by integrating (6.3) and averaging the infinitesimal potentials over l_c, and expressed as:

$$V_{A,A} = \frac{1}{l_c}\int_0^{l_c} V_{1,A}\,dz_1 = \frac{\rho I}{4\pi l_c}\left[2\ln\left(\frac{2+\sqrt{4+(r_c/l_c)^2}}{r_c}\right) - \sqrt{4+(r_c/l_c)^2} + \frac{r_c}{l_c}\right]. \tag{6.4}$$

Similarly, the self-potential of the electrode B from the current sink and its images at the electrode B, denoted by $V_{B,B}$, is expressed as:

$$V_{B,B} = \frac{-\rho I}{4\pi l_c}\left[2\ln\left(\frac{2+\sqrt{4+(r_c/l_c)^2}}{r_c}\right) - \sqrt{4+(r_c/l_c)^2} + \frac{r_c}{l_c}\right]. \tag{6.5}$$

6.2.2.4 Mutual potential

By referring to Fig. 6.3, making use of (6.5) and letting $r = d$, the potential of a point on the electrode B due to a current source and its images at the electrode A, denoted by $V_{2,A}$, is:

$$V_{2,A} = \frac{\rho I}{4\pi l_c}\ln\left[\frac{(z_2+l_c)+\sqrt{(z_2+l_c)^2+d^2}}{(z_2-l_c)+\sqrt{(z_2-l_c)^2+d^2}}\right]. \tag{6.6}$$

The mutual potential of the electrode B from current source and its images at the electrode A, denoted by $V_{B,A}$, is then obtained by integrating (6.6) and averaging the infinitesimal potentials over l_c, and expressed as:

$$V_{B,A} = \frac{1}{l_c}\int_0^{l_c} V_{2,A}\,dz_2 = \frac{\rho I}{4\pi l_c}\left[2\ln\left(\frac{2+\sqrt{4+(d/l_c)^2}}{d}\right) - \sqrt{4+(d/l_c)^2} + \frac{d}{l_c}\right]. \tag{6.7}$$

Similarly, the mutual potential of the electrode A from the current sink and its images at the electrode B, denoted by $V_{A,B}$, is expressed as:

$$V_{A,B} = \frac{-\rho I}{4\pi l_c}\left[2\ln\left(\frac{2+\sqrt{4+(d/l_c)^2}}{d}\right)-\sqrt{4+(d/l_c)^2}+\frac{d}{l_c}\right]. \tag{6.8}$$

6.2.2.5 Potential difference between electrodes A and B

Adding (6.4) and (6.8), the overall potential of the electrode A due to the current source and sink, and their respective images, at electrodes A and B, respectively, denoted by V_A, is:

$$V_A = \frac{\rho I}{4\pi l_c}\left\{2\ln\left[\left(\frac{2+\sqrt{4+(r_c/l_c)^2}}{2+\sqrt{4+(d/l_c)^2}}\right)\left(\frac{d}{r_c}\right)\right]+\sqrt{4+(d/l_c)^2}-\sqrt{4+(r_c/l_c)^2}+\left(\frac{r_c-d}{l_c}\right)\right\}. \tag{6.9}$$

In the same way, adding (6.5) and (6.7), the overall potential of the electrode B due to the current source and sink, and their respective images, at electrodes A and B, respectively, denoted by V_B, is:

$$V_B = \frac{-\rho I}{4\pi l_c}\left\{2\ln\left[\left(\frac{2+\sqrt{4+(r_c/l_c)^2}}{2+\sqrt{4+(d/l_c)^2}}\right)\left(\frac{d}{r_c}\right)\right]+\sqrt{4+(d/l_c)^2}-\sqrt{4+(r_c/l_c)^2}+\left(\frac{r_c-d}{l_c}\right)\right\}. \tag{6.10}$$

The potential difference between the two electrodes A and B, denoted by V, is then obtained from the difference between (6.9) and (6.10):

$$V = \frac{\rho I}{2\pi l_c}\left\{2\ln\left[\left(\frac{2+\sqrt{4+(r_c/l_c)^2}}{2+\sqrt{4+(d/l_c)^2}}\right)\left(\frac{d}{r_c}\right)\right]+\sqrt{4+(d/l_c)^2}-\sqrt{4+(r_c/l_c)^2}+\left(\frac{r_c-d}{l_c}\right)\right\}. \tag{6.11}$$

6.2.2.6 The theoretical geometric factor

Rearranging (6.11), the resistivity of the medium, $\rho_{2E,cyl}$, which is determined using the two-electrode method, when the slender cylindrical electrodes are modelled in the cylindrical coordinates is given by:

$$\rho_{2E,cyl} = \left(K_{2E,cyl}\right)R \tag{6.12}$$

where $R = V/I$. The subscripts $2E$ and *cyl* denote two-electrode and cylindrical, respectively. The geometric factor $K_{2E,cyl}$ is expressed as:

$$K_{2E,cyl} = \frac{2\pi l_c}{2\ln\left[\left(\frac{2+\sqrt{4+(r_c/l_c)^2}}{2+\sqrt{4+(d/l_c)^2}}\right)\left(\frac{d}{r_c}\right)\right] + \sqrt{4+(d/l_c)^2} - \sqrt{4+(r_c/l_c)^2} + \left(\frac{r_c-d}{l_c}\right)}. \tag{6.13}$$

6.2.3 Relationship between the measured resistance, the electrical resistivity and the geometric factor in the prolate spheroidal coordinates

The theoretical geometric factor for resistivity measurement using the two-electrode method with slender cylindrical electrodes modelled using the prolate spheroidal coordinates is shown hereafter. Consider the two-electrode method using slender cylindrical electrodes, as shown in Fig. 6.4. Electrodes *A* and *B*, which are the source and sink of the stimulus current, respectively, are modelled in the prolate spheroidal coordinates. A brief description of the prolate spheroidal coordinates system is in order. The relationship between the prolate spheroidal coordinates (η, δ, ϕ) and the cylindrical coordinates (r, ϕ, z) [99] is shown in Fig. 3.1. η_0 denotes the surface of the prolate spheroid and a is the semifocal distance of the prolate spheroid.

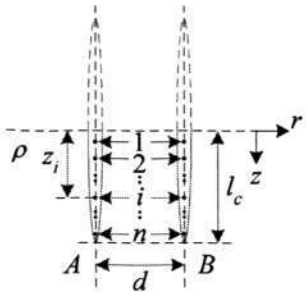

Figure 6.4 - Application of the image method for currents to the current source and sink electrodes A and B, respectively, with the electrodes modelled in the prolate spheroidal coordinates.

6.2.3.1 Potential of a point

Consider a half-prolate spheroid source electrode with current I in a conductive, homogeneous, isotropic and semi-infinite medium. The potential of a point P in the conductive medium that is induced by a point current source, derived in the prolate spheroidal coordinates, has already been derived in (4.3).

6.2.3.2 Self-potential

Making use of (4.3), the self-potential of the electrode A, denoted as $V_{A,A}$, which is induced by the current source and its images at the electrode A, is determined and expressed as:

$$V_{A,A} = \frac{\rho I}{4\pi l_c} \ln\left(\frac{\eta_0 + 1}{\eta_0 - 1}\right). \tag{6.14}$$

η_0 is obtained by equating the volume of the electrode in the cylindrical and prolate coordinate systems, and expressed as:

$$\eta_0 = \sqrt{1 + 1.5(r_c / l_c)^2}\,. \tag{6.15}$$

Similarly, the self-potential of the electrode *B*, denoted as $V_{B,B}$, which is induced by the current sink and its images at the electrode *B*, is expressed as:

$$V_{B,B} = \frac{-\rho I}{4\pi l_c} \ln\left(\frac{\eta_0 + 1}{\eta_0 - 1}\right). \tag{6.16}$$

6.2.3.3 Mutual potential

Each electrode is divided into *n* segments with each segment *i* located at a depth z_i. The potential of the i^{th} segment of the electrode *B* that is induced by the current source and its image at the electrode *A* is obtained using (4.3). This mutual potential, which is denoted as $V_{B,A}$, is then determined by averaging the total potential of every segment along the length of the electrode *B* and expressed as:

$$V_{B,A} = \frac{\rho I}{4\pi l_c}\left(\frac{1}{n}\right)\sum_{i=1}^{n} \ln\left(\frac{\eta_{1,i} + 1}{\eta_{1,i} - 1}\right) \tag{6.17}$$

$$\text{with } \eta_{1,i} = \sqrt{\frac{\left(l_c^{\,2} + d^2 + z_i^{\,2}\right) + \sqrt{\left(l_c^{\,2} + d^2 + z_i^{\,2}\right)^2 - 4 l_c^{\,2} z_i^{\,2}}}{2 l_c^{\,2}}}$$

where $z_i = l_c(2i-1)/2n$.

Similarly, the potential of the electrode *A* induced by current sink and its image at the electrode *B*, denoted as $V_{A,B}$, is expressed as:

$$V_{A,B} = \frac{-\rho I}{4\pi l_c}\left(\frac{1}{n}\right)\sum_{i=1}^{n} \ln\left(\frac{\eta_{1,i} + 1}{\eta_{1,i} - 1}\right). \tag{6.18}$$

6.2.3.4 Overall potential

Adding (6.14) and (6.18), the overall potential of the electrode A, denoted as V_A, that is induced by the current source and sink, and their particular images at electrodes A and B, respectively, can be expressed as:

$$V_A = \frac{\rho I}{4\pi l_c}\left[\ln\left(\frac{\eta_0+1}{\eta_0-1}\right)\left(\frac{1}{n}\right)\sum_{i=1}^{n}\ln\left(\frac{\eta_{1,i}-1}{\eta_{1,i}+1}\right)\right]. \tag{6.19}$$

Correspondingly, the overall potential of the electrode B, denoted as V_B, can be expressed as:

$$V_B = \frac{-\rho I}{4\pi l_c}\left[\ln\left(\frac{\eta_0+1}{\eta_0-1}\right)\left(\frac{1}{n}\right)\sum_{i=1}^{n}\ln\left(\frac{\eta_{1,i}-1}{\eta_{1,i}+1}\right)\right]. \tag{6.20}$$

6.2.3.5 Potential difference between electrodes A and B

The potential difference between the two electrodes A and B, which is denoted as V, is obtained by taking the difference between (6.19) and (6.20), and expressed as:

$$V = \frac{\rho I}{2\pi l_c}\left[\ln\left(\frac{\eta_0+1}{\eta_0-1}\right)\left(\frac{1}{n}\right)\sum_{i=1}^{n}\ln\left(\frac{\eta_{1,i}-1}{\eta_{1,i}+1}\right)\right]. \tag{6.21}$$

6.2.3.6 The theoretical geometric factor

Rearranging (6.21), the resistivity of the medium, $\rho_{2E,ps}$, which is determined using the two-electrode method, when the slender cylindrical electrodes are modelled in the prolate spheroidal coordinates is given:

$$\rho_{2E,ps} = \left(K_{2E,ps}\right)R \tag{6.22}$$

where $R = V/I$. The subscripts $2E$ and ps denote two-electrode and prolate spheroidal, respectively. The geometric factor $K_{2E,ps}$ is expressed as:

$$K_{2E,ps} = \frac{2\pi l_c}{\ln\left(\frac{\eta_0+1}{\eta_0-1}\right)\left(\frac{1}{n}\right)\sum_{i=1}^{n}\ln\left(\frac{\eta_{1,i}-1}{\eta_{1,i}+1}\right)} \tag{6.23}$$

with $\eta_0 = \sqrt{1+1.5(r_c/l_c)^2}$, $\eta_{1,i} = \sqrt{\frac{\left(l_c^2+d^2+z_i^2\right)+\sqrt{\left(l_c^2+d^2+z_i^2\right)^2-4l_c^2z_i^2}}{2l_c^2}}$,

$z_i = l_c(2i-1)/2n$ and n is the number of segments.

6.3 Numerical Simulations of the Derived Geometric Factors

Using numerical simulations, the effects of d, l_c and n on $K_{2E,ps}$ in (6.23) were investigated, and the results were tabulated in Table 6.I. The effects of d and l_c on $K_{2e,cyl}$ in (6.13) were also simulated and tabulated in Table 6.I.

Table 6.I - Numerical values of the geometric factors for different inter-electrode spacing, immersed electrode length and number of segments.

l_c (mm)	d (mm)	$K_{2e,cyl}$ $(\times 10^{-3})$	$K_{2E,ps}$ $(\times 10^{-3})$ $n=1$	$K_{2E,ps}$ $(\times 10^{-3})$ $n=5$	$K_{2E,ps}$ $(\times 10^{-3})$ $n=10$	$K_{2E,ps}$ $(\times 10^{-3})$ $n=100$
5	1	12.1	12.2	11.8	11.8	11.7
	2	8.29	8.15	8.03	8.01	8.00
	3	7.10	6.94	6.88	6.87	6.87
	4	6.50	6.34	6.30	6.30	6.30
	5	6.13	5.97	5.95	5.95	5.95
	10	5.38	5.24	5.24	5.24	5.24
	20	5.00	4.88	4.88	4.88	4.88
	30	4.88	4.76	4.76	4.76	4.76
	40	4.81	4.70	4.70	4.70	4.70

10	1	23.6	24.1	23.2	23.0	22.9
	2	15.9	15.9	15.5	15.4	15.4
	3	13.5	13.3	13.1	13.1	13.0
	4	12.2	12.0	11.9	11.8	11.8
	5	11.4	11.2	11.1	11.1	11.1
	10	9.69	9.46	9.43	9.43	9.43
	20	8.72	8.52	8.51	8.51	8.51
	30	8.39	8.19	8.19	8.19	8.19
	40	8.22	8.03	8.03	8.03	8.03

The plots of $K_{2e,cyl}$, and $K_{2E,ps}$ for two different l_c (l_c of 5 mm and 10 mm) as d was varied were shown in Fig. 6.5. In the numerical simulations of $K_{2E,ps}$ in (6.23), n was set at 10.

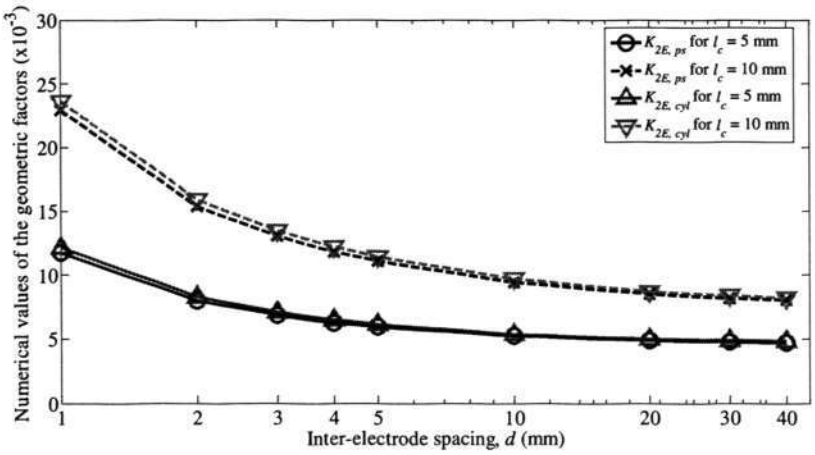

Figure 6.5 - Numerical values of the geometric factors as the inter-electrode spacing d was varied from 1 mm to 40 mm, with the number of segments n used to compute the derived geometric factor K_{ps} in (6.23) set at 10.

In Chapter 4, it was shown that $K_{4E,cyl}$ and $K_{4E,ps}$ were different at small inter-electrode spacing s $(1\,\text{mm} \le s \le 10\,\text{mm})$. Although the finite dimensions of the electrode were considered in the derivation of both $K_{4E,cyl}$ and $K_{4E,ps}$, there was a significant difference in $K_{4E,cyl}$ and $K_{4E,ps}$ when s was small in comparison to l_c, e.g., $s \le 5\,\text{mm}$ and $l_c = 10\,\text{mm}$. However, from the computation shown for $K_{2e,cyl}$ and $K_{2E,ps}$, there was no significant difference in $K_{2e,cyl}$ and $K_{2E,ps}$ as d was varied from 1 mm to 40 mm. The simulation results

showed that the numerical values of $K_{2e,cyl}$ and $K_{2E,ps}$ were close to each other as d was varied. Consequently, the evaluation of the simulation results showed that either $K_{2e,cyl}$ or $K_{2E,ps}$ can be utilised to determine the resistivity from the measured resistance values.

6.4 Experimental Set-Up

Using the measurement system, the experiments were conducted to validate the proposed geometric factors using the two-electrode method, as shown in Fig. 6.6. The functions of the various components of the measurement system have been discussed in Section 4.4.

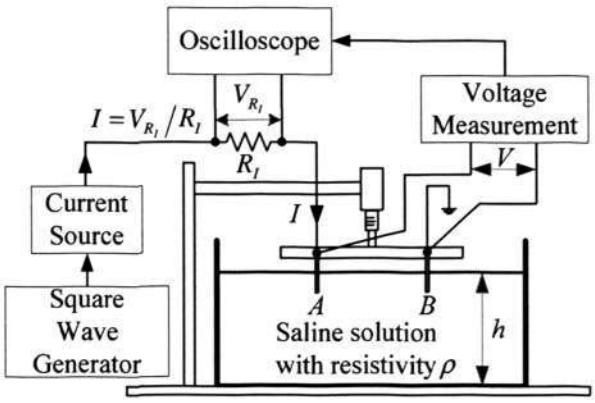

Figure 6.6 - The measurement system for experiments using the two-electrode method with slender cylindrical electrodes. The current was injected into the electrode *A* while the electrode *B* was grounded.

The test model consisted of a saline solution in a cylindrical container made of non-conducting material, with a diameter of 400 mm. The maximum d used in the experiments was 30 mm. Since the current I was only injected through electrode *A* while electrode *B* was grounded, as shown in Fig. 6.6, only one of the two OTAs inside the LM13700N was used to convert the square wave voltage into a constant alternating current. The magnitude of the

current was determined by controlling the ratio of the input voltage and a gain resistor. R was taken as the ratio of V to I, and the calculated resistivities obtained using the derived geometric factor were compared with the resistivities measured using the commercial conductivity meter.

6.4.1 Saline solutions

The saline solution was prepared by mixing common salt and water. Two saline solutions, $6X$ and $6Y$, were prepared. The salt concentration of saline solutions $6X$ and $6Y$ were 2.5 g/litre and 0.067 g/litre, respectively; these concentrations were chosen to approximate that of biological tissues. The saline resistivities were measured using a commercial conductivity meter (YSI model EC300), which is shown in Fig. 4.8, so as to act as a reference for comparison. The resistivity that was obtained using the commercial conductivity meter was denoted by ρ_{cm}. The operations of the commercial conductivity meter were described in Section 4.5.1.

Using a thermometer (Fluke model FLU65), which was shown in Fig. 4.9, the temperature of the saline solution was measured to be 21 °C. All measurements were conducted when the saline solutions were at 21 °C.

6.4.2 Electrodes

The experiments were conducted using the two-electrode method with two slender cylindrical Ag/AgCl electrodes. The Ag/AgCl electrodes used were purchased from A-M Systems, Inc., Carlsborg, USA. The Ag/AgCl electrodes were manufactured from Ag wires (with a diameter of 0.38 mm) using a sintering process. The diameters of the Ag/AgCl electrodes were

measured using a digimatic calliper (Mitutoyo model CD-6" CsX), which is shown in Fig.4.10, and the average diameter was found to be 0.51 mm.

6.5 Experimental Procedures

It is to be noted that for the experiments described hereafter in this section, unless otherwise stated, d, l_c and h were maintained at 5 mm, 2 mm and 60 mm, respectively, where h denotes the depth of the saline solution. The experiments were conducted for both saline solutions $6X$ and $6Y$.

6.5.1 Effect of the frequency on the measured resistance

The effect of varying the frequency of the current source f on the measured R was studied to determine a suitable frequency to conduct the experiments. f was varied from 10 Hz to 10 kHz.

6.5.2 Effect of the current density on the geometric factors

The effect of varying the current density J on the measured K_{2E} and the theoretical $K_{2E,cyl}$ and $K_{2E,ps}$ was studied in order to determine a suitable current to conduct the experiments. J was varied from about 17 A/m^2 to 300 A/m^2. The theoretical $K_{2E,cyl}$ and $K_{2E,ps}$ were determined using (6.13) and (6.23), respectively. From the experimental results, the measured K_{2E} was determined using the following expression:

$$K_{2E} = \rho_{cm}/R. \tag{6.24}$$

6.5.3 Effect of the time on the measured resistance and the calculated resistivity

The effect of the measurement time on the measured R and the calculated $\rho_{2E,cyl}$ and $\rho_{2E,ps}$ was studied to determine the stability of the measurement. The measurement was conducted for a period of 1 hour where R was measured every 5 minutes.

6.5.4 Effects of d, l_c and h on the calculated resistivity

The effects of varying d, l_c and h on the calculated $\rho_{2E,cyl}$ and $\rho_{2E,ps}$ were studied. With h of 60 mm, the electrodes were first fixed at a particular d and then lowered into the saline solution by rotating the micrometer. The electrodes were immersed to the required l_c, and measurements were taken for the particular d and l_c. The above procedure was repeated as d was varied from 5 mm to 30 mm, and l_c was varied from 2 mm to 5 mm.

Next, with d and l_c both fixed at 5 mm, the measurements were taken as h was decreased in steps of 1 mm from 10 mm downwards.

6.5.5 Effect of the temperature on the calculated resistivity

The effect of the temperature of the saline solution on the calculated $\rho_{2E,cyl}$ and $\rho_{2E,ps}$ was studied since the resistivity, which changes with temperature, was dependent on the temperature at which the measurement was conducted. The temperature tested varied from 21 °C to 55 °C.

6.6 Experimental Results and Discussions

Using the commercial conductivity meter, the ρ_{cm} obtained for saline solutions 6*X* and 6*Y* were tabulated are 2.066 $\Omega \cdot$ m and 40.58 $\Omega \cdot$ m, respectively. Table 6.I showed that for the range of d (5 mm and above) and l_c (2 mm and 5 mm) used in the experiments, $K_{2E,ps}$ remains relatively constant when the number of segments n used was 10 and above. Hence for the calculation of $K_{2E,ps}$, the n used was 10.

6.6.1 Shape of typical waveforms of V and V_{R_l}

Both the V and V_{R_l} were observed using the oscilloscope, and the shape of the typical voltage waveforms of V and V_{R_l} were similar to those that were shown in Fig. 4.11. From each set of measured V and V_{R_l}, the corresponding resistance R was determined. The saline resistivities $\rho_{2E,cyl}$ and $\rho_{2E,ps}$ were obtained using the geometric factors $K_{2E,cyl}$ in (6.13) and $K_{2E,ps}$ in (6.23), respectively.

6.6.2 Effect of the frequency on the measured resistance

As the frequency f of the current source was varied, the measured resistance R of saline solutions 6*X* and 6*Y* were tabulated in Table 6.II.

Table 6.II - Measured resistances of saline solutions $6X$ and $6Y$ as the frequency of the current source was varied.

f (Hz)	Saline solution $6X$ R (Ω)	Saline solution $6Y$ R (kΩ)
10	773	15.4
20	774	15.4
30	770	15.3
50	769	15.3
100	767	15.3
200	760	15.2
300	729	14.4
1000	715	14.3
2000	715	14.3
3000	715	14.3
5000	715	14.3
10000	715	14.3

The plots of the measured R for saline solutions $6X$ and $6Y$ were shown in Figs. 6.7 and 6.8, respectively. The experimental results shown in Figs. 6.7 and 6.8 inferred that as f tends towards infinity, the effect of the polarisation impedance tends to zero. Since R remained fairly constant from 1 kHz upwards, subsequent experiments were conducted at f of 3 kHz, whereby the effect of polarisation impedance was neglected and the measured R was equated to the bulk electrolyte resistance between the two electrodes. At this juncture, it was also worthwhile to note that the tissue impedance is considered mostly resistive in the low frequency range [4, 122].

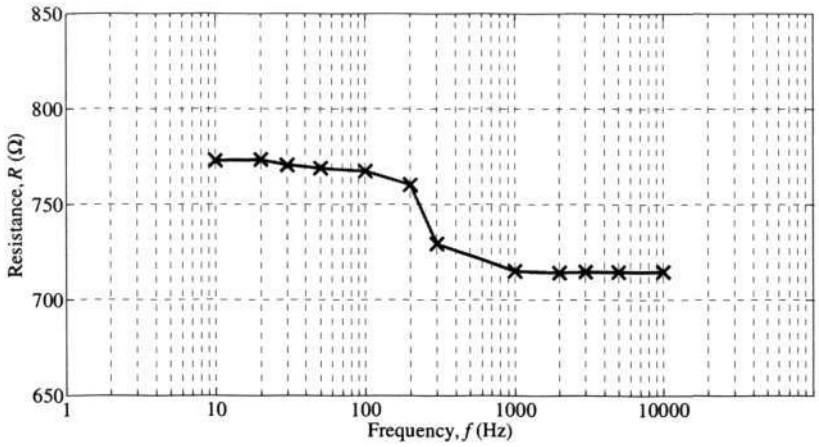

Figure 6.7 - Plot of measured resistance R versus frequency f for saline solution 6X.

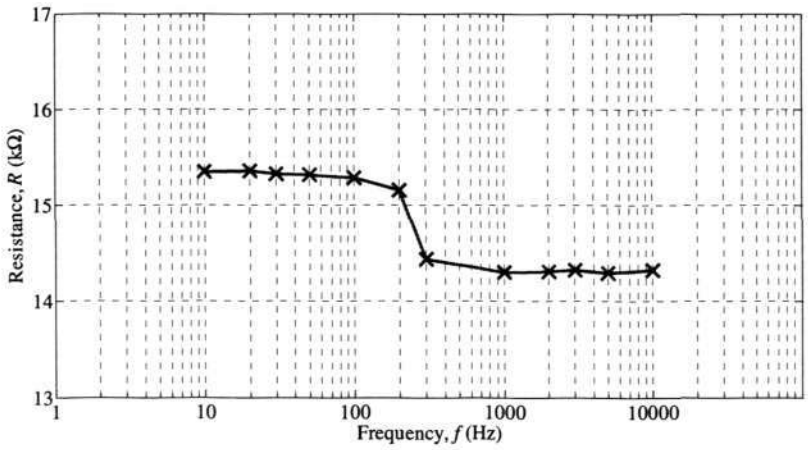

Figure 6.8 - Plot of measured resistance R versus frequency f for saline solution 6Y.

6.6.3 Effect of the current density on the geometric factors

As the current density J was varied, a comparison between the measured K_{2E}, obtained using (6.24), and the theoretical $K_{2E,cyl}$ and $K_{2E,ps}$, which were obtained using (6.13) and (6.23), correspondingly, was tabulated in Tables 6.III and 6.IV for saline solutions 6X and 6Y, respectively. The percentage differences $|\%\,\mathrm{Diff}|_4$ and $|\%\,\mathrm{Diff}|_5$ were obtained using:

$$|\%\ \text{Diff}|_4 = \left(\frac{\text{Measured } K_{2E} - \text{Theoretical } K_{2E,cyl}}{\text{Theoretical } K_{2E,cyl}} \right) \times 100\% . \tag{6.25}$$

$$|\%\ \text{Diff}|_5 = \left(\frac{\text{Measured } K_{2E} - \text{Theoretical } K_{2E,ps}}{\text{Theoretical } K_{2E,ps}} \right) \times 100\% . \tag{6.26}$$

Table 6.III - The theoretical and measured geometric factors as the current density J was varied for the saline solution 6X.

J (A/m^2)	ρ_{cm} $(\Omega \cdot \text{m})$	Measured K_{2E} $(\times 10^{-3})$	Theoretical $K_{2E,cyl}$ $(\times 10^{-3})$	$\lvert\%\ \text{Diff}\rvert_4$	Theoretical $K_{2E,ps}$ $(\times 10^{-3})$	$\lvert\%\ \text{Diff}\rvert_5$
17.8	2.066	2.96	2.95	0.339	2.89	2.42
35.6	2.066	2.96	2.95	0.339	2.89	2.42
163	2.066	2.95	2.95	0.000	2.89	2.08
293	2.066	2.93	2.95	0.678	2.89	1.38

Table 6.IV - The theoretical and measured geometric factors as the current density J was varied for the saline solution 6Y.

J (A/m^2)	ρ_{cm} $(\Omega \cdot \text{m})$	Measured K_{2E} $(\times 10^{-3})$	Theoretical $K_{2E,cyl}$ $(\times 10^{-3})$	$\lvert\%\ \text{Diff}\rvert_4$	Theoretical $K_{2E,ps}$ $(\times 10^{-3})$	$\lvert\%\ \text{Diff}\rvert_5$
17.8	2.066	2.90	2.95	1.69	2.89	0.346
35.6	2.066	2.89	2.95	2.03	2.89	0.000
163	2.066	2.91	2.95	1.36	2.89	0.692
293	2.066	2.89	2.95	2.03	2.89	0.000

The results in Tables 6.III and 6.IV showed that the measured K_{2E} remained fairly constant and in close agreement with the theoretical $K_{2E,cyl}$ and $K_{2E,ps}$. The evaluation of the experimental result showed that the measured K_{2E} was independent of the range of J tested.

6.6.4 Effect of the time on the measured resistance and the calculated resistivity

As the measurement was conducted, R was measured and the corresponding calculated $\rho_{2E,cyl}$ and $\rho_{2E,ps}$ were tabulated in Tables 6.V and 6.VI for saline solutions 6X and 6Y, respectively. The percentage differences $|\%\ \text{Diff}|_6$ and $|\%\ \text{Diff}|_7$ were obtained using:

$$\left|\%\ \text{Diff}\right|_6 = \left(\frac{\rho_{2E,cyl} - \rho_{cm}}{\rho_{cm}}\right) \times 100\% \,. \tag{6.27}$$

$$\left|\%\ \text{Diff}\right|_7 = \left(\frac{\rho_{2E,ps} - \rho_{cm}}{\rho_{cm}}\right) \times 100\% \,. \tag{6.28}$$

Table 6.V - The measured resistance and calculated resistivity over a measurement period of 1 hour for the saline solution 6*X*.

Time (s)	R (Ω)	$\rho_{2E,cyl}$ ($\Omega \cdot$m)	$\left\|\%\ \text{Diff}\right\|_6$	$\rho_{2E,ps}$ ($\Omega \cdot$m)	$\left\|\%\ \text{Diff}\right\|_7$
0	693	2.05	0.77	2.00	3.19
300	713	2.11	2.13	2.06	0.29
600	700	2.07	0.19	2.02	2.23
900	686	2.03	1.74	1.98	4.16
1200	705	2.11	2.13	2.07	0.19
1500	701	2.07	0.19	2.03	1.74
1800	702	2.08	0.68	2.03	1.74
2100	692	2.04	1.26	2.00	3.19
2400	696	2.05	0.77	2.01	2.71
2700	709	2.09	1.16	2.05	0.77
3000	712	2.10	1.65	2.06	0.29
3300	724	2.14	3.58	2.09	1.16
3600	701	2.07	0.19	2.03	1.74

Table 6.VI - The measured resistance and calculated resistivity over a measurement period of 1 hour for the saline solution 6*Y*.

Time (s)	R (kΩ)	$\rho_{2E,cyl}$ ($\Omega \cdot$m)	$\left\|\%\ \text{Diff}\right\|_6$	$\rho_{2E,ps}$ ($\Omega \cdot$m)	$\left\|\%\ \text{Diff}\right\|_7$
0	14.17	41.9	3.25	41.0	1.03
300	14.20	42.0	3.50	41.0	1.03
600	14.16	41.8	3.01	40.9	0.79
900	14.19	41.9	3.25	41.0	1.03
1200	14.19	41.9	3.25	41.0	1.03
1500	14.20	42.0	3.50	41.0	1.03
1800	14.18	41.9	3.25	41.0	1.03
2100	14.19	41.9	3.25	41.0	1.03
2400	14.24	42.1	3.75	41.3	1.77
2700	14.15	41.8	3.01	40.9	0.79
3000	14.20	42.0	3.50	41.0	1.03
3300	14.19	41.9	3.25	41.0	1.03
3600	14.20	42.0	3.50	41.0	1.03

Tables 6.V and 6.VI show that as the measurement was conducted over a period of 1 hour, the measured R remained fairly constant and the measured ρ_{cm} were in close agreement with both the calculated $\rho_{2E,cyl}$ and $\rho_{2E,ps}$. The evaluation of the experimental result showed that the measured R and subsequent calculated values of $\rho_{2E,cyl}$ and $\rho_{2E,ps}$ were independent of the duration tested, i.e., the measured R and the calculated $\rho_{2E,cyl}$ and $\rho_{2E,ps}$ were stable.

6.6.5 Effects of d, l_c and h on the calculated resistivity

The experimental results that were obtained as d and l_c were varied for saline solutions 6*X* and 6*Y* were tabulated in Tables 6.VII and 6.VIII, respectively. From the measured R, both $\rho_{2E,cyl}$ and $\rho_{2E,ps}$ were calculated and the percentage difference $|\%\,\mathrm{Diff}|_6$ and $|\%\,\mathrm{Diff}|_7$ were obtained using (6.27) and (6.28), respectively.

Table 6.VII - The measured resistance and calculated resistivity as the inter-electrode spacing and the length of immersed electrode were varied for the saline solution 6*X*.

d (mm)	l_c (mm)	R (Ω)	$\rho_{2E,cyl}$ (Ω·m)	$\lvert\%\,\mathrm{Diff}\rvert_6$	$\rho_{2E,ps}$ (Ω·m)	$\lvert\%\,\mathrm{Diff}\rvert_7$
5	2	719	2.12	2.61	2.08	0.68
	3	514	2.06	0.29	2.01	2.71
	4	420	2.13	3.10	2.07	0.19
	5	349	2.14	3.58	2.08	0.68
10	2	759	2.06	0.29	2.02	2.23
	3	571	2.07	0.19	2.02	2.23
	4	465	2.10	1.65	2.04	1.26
	5	397	2.13	3.10	2.08	0.68
20	2	799	2.08	0.68	2.04	1.26
	3	626	2.15	4.07	2.10	1.65
	4	500	2.11	2.13	2.06	0.29
	5	425	2.12	2.61	2.07	0.19
30	2	795	2.04	1.26	2.01	2.71
	3	634	2.14	3.58	2.09	1.16
	4	497	2.06	0.29	2.01	2.71
	5	437	2.13	3.10	2.08	0.68

Table 6.VIII - The measured resistance and calculated resistivity as the inter-electrode spacing and the length of immersed electrode were varied for the saline solution 6*Y*.

d (mm)	l_c (mm)	R (kΩ)	$\rho_{2E,cyl}$ (Ω·m)	$\lvert\%\ \mathrm{Diff}\rvert_6$	$\rho_{2E,ps}$ (Ω·m)	$\lvert\%\ \mathrm{Diff}\rvert_7$
5	2	14.2	42.1	3.75	41.2	1.53
	3	10.2	41.0	1.03	39.9	1.68
	4	8.11	41.2	1.53	40.0	1.43
	5	6.85	42.0	3.50	40.8	0.54
10	2	15.2	41.4	2.02	40.6	0.05
	3	11.7	42.2	3.99	41.2	1.53
	4	9.37	42.2	3.99	41.1	1.28
	5	7.72	41.5	2.27	40.4	0.44
20	2	16.1	42.2	3.99	41.4	2.02
	3	12.2	42.0	3.50	41.1	1.28
	4	9.67	40.9	0.79	39.9	1.68
	5	8.45	42.2	3.99	41.2	1.53
30	2	16.0	41.1	1.28	40.3	0.69
	3	12.3	41.6	2.51	40.7	0.30
	4	10.1	41.7	2.76	40.7	0.30
	5	8.49	41.3	1.77	40.4	0.44

Tables 6.VII and 6.VIII show that as d and l_c were varied, the measured R remained fairly constant and the measured ρ_{cm} were in close agreement with both the calculated $\rho_{2E,cyl}$ and $\rho_{2E,ps}$. The evaluation of the experimental result showed that the theoretical $K_{2E,cyl}$ and $K_{2E,ps}$ were able to obtain an accurate resistivity value for different combinations of d and l_c.

Next, the experimental results obtained as h was decreased in steps of 1 mm from 10 mm, with d and l_c maintained at 5 mm and 2 mm, respectively, were tabulated in Tables 6.IX and 6.X for saline solutions 6*X* and 6*Y*, respectively.

Table 6.IX - The measured resistance and calculated resistivity as the depth of the saline solution 6*X* was varied.

h (mm)	R (Ω)	$\rho_{2E,cyl}$ (Ω·m)	$\lvert\%\ \mathrm{Diff}\rvert_6$	$\rho_{2E,ps}$ (Ω·m)	$\lvert\%\ \mathrm{Diff}\rvert_7$
10	703	2.08	0.68	2.03	1.74
9	714	2.11	2.13	2.06	0.29
8	708	2.09	1.16	2.05	0.77

7	708	2.09	1.16	2.05	0.77
6	714	2.11	2.13	2.06	0.29
5	705	2.08	0.68	2.04	1.26
4	752	2.22	7.45	2.17	5.03
3	774	2.29	10.8	2.24	8.42

Table 6.X - The measured resistance and calculated resistivity as the depth of the saline solution 6*Y* was varied.

h (mm)	R (kΩ)	$\rho_{2E,cyl}$ (Ω·m)	$\lvert\%\ \mathrm{Diff}\rvert_6$	$\rho_{2E,ps}$ (Ω·m)	$\lvert\%\ \mathrm{Diff}\rvert_7$
10	14.2	42.0	3.50	41.1	1.28
9	14.2	42.1	3.75	41.1	1.28
8	14.2	41.9	3.25	41.0	1.03
7	14.2	42.0	3.50	41.1	1.28
6	14.2	41.9	3.25	41.0	1.03
5	14.2	41.8	3.01	40.9	0.79
4	14.8	43.7	7.69	42.7	5.22
3	15.2	44.8	10.4	43.9	8.18

Tables 6.IX and 6.X showed that as h was decreased in steps of 1 mm from 10 mm to 5 mm, the measured R remained fairly constant the measured ρ_{cm} were in close agreement with both the calculated $\rho_{2E,cyl}$ and $\rho_{2E,ps}$. In addition, with d of 5 mm and l_c of 2 mm:

- both $\lvert\%\ \mathrm{Diff}\rvert_6$ and $\lvert\%\ \mathrm{Diff}\rvert_7 < 5\%$ if $h \geq 5\,\mathrm{mm}$;
- both $\lvert\%\ \mathrm{Diff}\rvert_6$ and $\lvert\%\ \mathrm{Diff}\rvert_7 > 5\%$ if $h < 5\,\mathrm{mm}$.

The evaluation of the result showed that when l_c was 2 mm and d was 5 mm, a consistent resistivity of the medium was obtained even at a shallow depth h of 5 mm.

6.6.6 Effect of the temperature on the calculated resistivity

As the temperature of the saline solution was varied, the temperature dependence of the $\rho_{2E,cyl}$ and $\rho_{2E,ps}$ for saline solutions 6*X* and 6*Y*, was tabulated in Tables 6.XI and 6.XII, respectively.

Table 6.XI - The measured resistance and calculated resistivity as the temperature of the saline solution 6*X* was varied.

Temp. (°C)	*R* (Ω)	$\rho_{2E,cyl}$ (Ω·m)	$\rho_{2E,ps}$ (Ω·m)
21	704	2.08	2.04
23	612	1.81	1.77
25	558	1.65	1.61
27	540	1.60	1.56
29	533	1.57	1.54
31	493	1.46	1.43
33	485	1.43	1.40
35	468	1.38	1.35
40	402	1.19	1.16
45	383	1.13	1.11
50	370	1.09	1.07
55	342	1.01	0.99

Table 6.XII - The measured resistance and calculated resistivity as the temperature of the saline solution 6*Y* was varied.

Temp. (°C)	*R* (kΩ)	$\rho_{2E,cyl}$ (Ω·m)	$\rho_{2E,ps}$ (Ω·m)
21	14.2	42.0	41.1
23	12.8	37.8	36.9
25	10.7	31.7	31.0
27	10.6	31.2	30.5
29	10.5	30.9	30.2
31	9.74	28.8	28.2
33	9.43	27.9	27.3
35	9.02	26.7	26.1
40	8.09	23.9	23.5
45	7.59	22.4	21.9
50	7.22	21.3	20.9
55	6.71	19.8	19.4

From the resistivity calculated as the temperature of the saline solution was varied, a best–fit curve was obtained from the experimental data. An example was provided where the best-fit curve for $\rho_{2E,ps}$ was shown in Figs. 6.9 and 6.10, for saline solutions 6*X* and 6*Y*, respectively. Similar best-fit curve can be obtained using $\rho_{2E,cyl}$ for saline solutions 6*X* and 6*Y*.

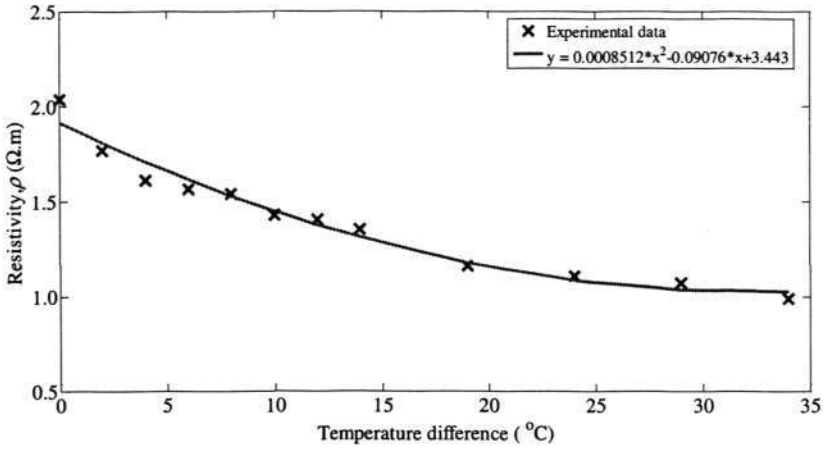

Figure 6.9 - Plot of resistivity versus temperature difference with respective to the lowest temperature measured $(21\,°C)$ for the saline solution 6*X*.

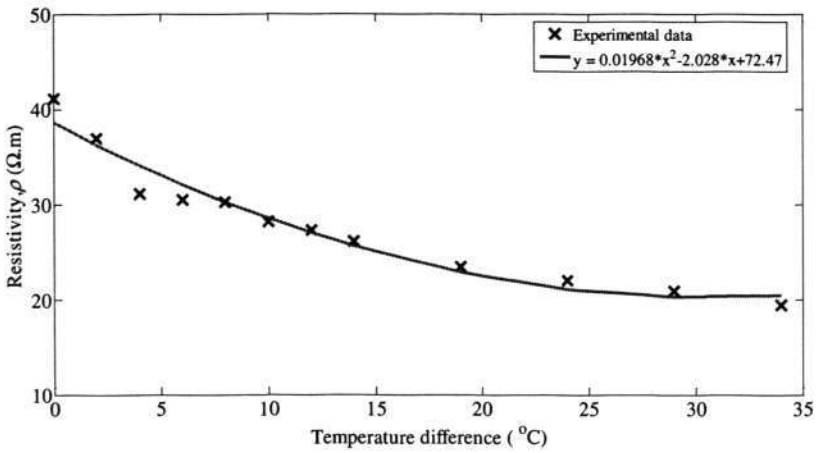

Figure 6.10 - Plot of resistivity versus temperature difference with respective to the lowest temperature measured $(21\,°C)$ for the saline solution 6*Y*.

The temperature dependence of $\rho_{2E,ps}$ for saline solutions 6*X* and 6*Y*, shown in Figs. 6.9 and 6.10, respectively, indicated the effect of the temperature on the resistivity. From the temperature dependence, it was shown that the resistivity decreases increased as the temperature increased. These results indicated the negative coefficient of resistivity with increasing temperature, which are consistent with other researchers' results [32]. Hence, the resistivity at a particular temperature can be obtained from the best-fit curve.

6.7 Concluding Remarks

In this chapter, new geometric factors for the *in situ* resistivity measurement of conductive media by means of two slender cylindrical electrodes have been presented. The geometric factors were derived in the prolate spheroidal and the cylindrical coordinates. The effects of frequency, current density, time, electrode geometry and temperature on the proposed two-electrode resistivity measurement technique using plunge electrodes were investigated. The evaluation of the experimental results showed that the proposed technique is suitable for the measurement of the resistivity of small-volume biological samples, where the resistivities of the saline solutions obtained using the derived geometric factors and those obtained using a commercial conductivity meter were both in good agreement even when the inter-electrode spacing, the length of the immersed electrode or the depth of the sample was varied.

In conclusion, the evaluation of the experimental results showed that the proposed two-electrode method is a promising measurement technique for biomedical applications where small-volume samples are often encountered. The ability of the two-electrode method in obtaining consistent resistivity even at small sample depth indicates its suitability for resistivity measurement of small-volume sample. The ratio of $l_e : d : h$ was approximately 0.4:1:1 and if this ratio is maintained constant, the dimensions can be drastically scaled down to values even much smaller than those conducted in the experiments. This is a significant improvement to the four-electrode method for measuring tissues resistivities, which is shown in Chapter 4, where the measured resistivities were affected by the small-volume samples.

CHAPTER 7 - RESISTIVITY MEASUREMENT OF ULTRA-SMALL-VOLUME SAMPLES USING TWO PLANAR DISC ELECTRODES WITH A VIEW TO MICROFLUIDICS APPLICATIONS

7.1 Overview

In Chapter 6, the geometric factors for the *in situ* resistivity measurement using the two-electrode method by means of two slender cylindrical electrodes were presented in (6.13) and (6.23). Equations (6.13) and (6.23) were derived in the cylindrical and the prolate spheroidal coordinates, respectively. It was shown that the resistivity measurement was accurate for small-volume sample, where the ratio of $l_c : d : h$ is approximately 0.4:1:1:1. Throughout this chapter, the length of the immersed electrode, the inter-electrode spacing and the depth of the sample were denoted by l_c, d and h, respectively. However, the evaluation of the experimental results in Chapter 6 also showed that as d and l_c were both fixed at 5 mm and $h < 5\,\text{mm}$, there was a derivation of more than 5% between the resistivities measured using the commercial conductivity meter and those that were obtained using the derived geometric factors $K_{2E,ps}$ and $K_{2e,cyl}$.

In this chapter, the use of the two-electrode method for resistivity measurement in microfluidic applications is studied. The aim is to derive a new geometric factor for an accurate resistivity measurement of ultra-small-volume sample of biofluids by means of two planar disc electrodes with a view to its application in a microfluidic channel. The new geometric factor is derived using the oblate spheroidal coordinates.

Due to the advances in micro-system fabrication processes, the use of the microfluidic devices to conduct biomedical research and create clinically useful technologies has been growing over the years. In addition, there has been a noticeable trend toward the use of microchips and microfluidic devices for biochemical analysis [158]. Rapid *in situ* analysis of biological cells and detection of ultra-small-volume samples, even single cell, are also in great demand since it covers a range of applications from environmental monitoring and bio-defence to disease diagnosis and point of care [159]. The possibility of focusing and separating blood cells based on their conductivity and shape characteristics has a great potential in studying the fundamental properties of the cells as well as in the medical diagnostics field [160].

The contributions of this chapter are the theoretical derivation and the experimental validation of a new geometric factor, derived in the oblate spheroidal coordinates, for resistivity measurement using two thin planar disc electrodes. The theoretical geometric factor took the shape and the dimensions of the electrodes and the spacing between them into account in order to obtain the dependence of the resistance between the electrodes on the resistivity of the medium. Experiments were conducted to validate the theoretical geometric factor using saline solutions in a grounded metallic container and an electronic circuit. By using relatively non-polarizable Ag/AgCl planar disc electrodes where the bottom part of the disc was just in contact with the saline solution and conducting the experiments at an excitation frequency of 3 kHz, the problems associated with the electrode polarisation were minimised. The evaluation of the experimental results that will be presented later in this chapter showed that the resistivities of the saline solutions obtained using the derived geometric factors and those obtained using a commercial conductivity meter were both in good agreement even when the inter-electrode spacing, the length of the immersed electrode or the depth of the sample was varied. The two-electrode method for the resistivity measurement described above was also shown to be independent of the current density of the source of excitation. In addition, the

measurement reading was shown to be consistent over the measurement period of 1 hour. The temperature dependence of the measured resistivity of saline solution using the two-electrode method was also presented. This two-electrode method also produced consistent results even at small sample depths thereby making it suitable for applications in microfluidic channels for the measurement of the resistivity of biofluids.

This chapter is organised as follows. New geometric factor for the resistivity measurement using the two-electrode method is derived in the oblate spheroidal coordinates in Section 7.2. The experimental set-up and procedures are described in sections 7.3 and 7.4, respectively. The experimental results are presented in Section 7.5. The concluding remarks are given in Section 7.6.

7.2 Theory

For the two-electrode method shown in Fig. 7.1, whereby two thin planar disc electrodes, each with radius b, are in contact with the medium, both conduction and displacement currents flow between the electrode and the medium. Details pertaining to the polarisation impedance and the approaches to control and minimize the effect of the polarisation impedance were discussed in Chapter 6.

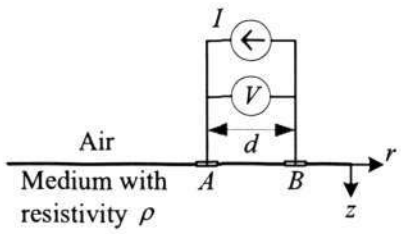

Figure 7.1 - Two-electrode method for resistivity measurement using planar disc electrodes.

7.2.1 Relationship between the measured resistance, the electrical resistivity and the geometric factor in the oblate spheroidal coordinates

Consider the two-electrode method using the planar disc electrodes, as shown in Fig. 7.2. The current source and sink electrodes, A and B, respectively, are modelled in the oblate spheroidal coordinates. As noted in Chapter 4, the spheroidal coordinates are considered as the general ellipsoidal form that covers, as an approximation, almost the whole variety of possible shapes for particles and segregates of physical interest [100] and spheroids are examples of objects that have continuously varying surface curvatures[101]. In this chapter, the oblate spheroids are of interest because the oblate spheroids are good approximation to the planar disc electrodes [103-105].

A brief description of the oblate spheroidal coordinates system is in order. The relationship between the oblate spheroidal coordinates (η, δ, ϕ) and the cylindrical coordinates (r, ϕ, z) is shown in Fig. 3.2. η_0 denotes the surface of the oblate spheroid and a is the semifocal distance of the oblate spheroid.

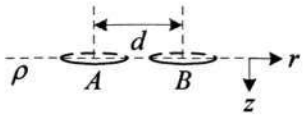

Figure 7.2 - Application of the image method for currents to the current source and sink electrodes A and B, respectively, with the electrodes modelled in the oblate spheroidal coordinates.

The theoretical geometric factor for resistivity measurement using the two-electrode method with planar disc electrodes modelled using the oblate spheroidal coordinates is shown hereafter.

7.2.1.1 Potential of a point

Consider a half-oblate spheroid source electrode with current I in a conductive, homogeneous, isotropic and semi-infinite medium. Applying the image method for currents [118], the result is an oblate spheroid with a current of $2I$ emanating from its surface into an infinite medium of resistivity ρ. Making use of (3.67), the potential of a point P in the medium induced by the source electrode with current $2I$ is given by:

$$\begin{aligned} V &= \frac{\rho(2I)}{4\pi b}\tan^{-1}\left(\frac{1}{\eta}\right) \\ &= \frac{\rho I}{2\pi b}\tan^{-1}\left(\frac{1}{\eta}\right) \end{aligned} \tag{7.1}$$

with η defined in (3.68).

7.2.1.2 Self-potential

Making use of (3.62) and since for planar thin disc electrodes, the oblate spheroid surface $\eta_0 \cong 0$ [106] and consequently $a \cong b$, the self-potential of the electrode A, denoted as $V_{A,A}$, which is induced by the current source and its images at the electrode A, is expressed as:

$$\begin{aligned} V_{A,A} &= \frac{\rho(2I)}{8b} \\ &= \frac{\rho I}{4b}. \end{aligned} \tag{7.2}$$

Similarly, the self-potential of the electrode B, denoted as $V_{B,B}$, which is induced by the current sink and its images at the electrode B, is expressed as:

$$V_{B,B} = \frac{-\rho I}{4b}. \tag{7.3}$$

7.2.1.3 Mutual potential

Making use of (7.1), the mutual potential of the electrode B, which is induced by the current source and its images at the electrode A, denoted as $V_{B,A}$, is determined and expressed as:

$$V_{B,A} = \frac{\rho I}{2\pi b} \tan^{-1}\left(\frac{1}{\eta_1}\right) \tag{7.4}$$

where $\eta_1 = \sqrt{(d/b)^2 - 1}$ by making use of (3.68), letting $r = b$ and $z = 0$.

Similarly, the mutual potential of the electrode A, which is induced by the current sink and its images at the electrode B, denoted as $V_{A,B}$, is expressed as:

$$V_{A,B} = \frac{-\rho I}{2\pi b} \tan^{-1}\left(\frac{1}{\eta_1}\right). \tag{7.5}$$

7.2.1.4 Overall potential

Adding (7.2) and (7.5), the overall potential of the electrode A, denoted as V_A, that is induced by the current source and sink, and their particular images at electrodes A and B, respectively, can be expressed as:

$$V_A = \frac{\rho I}{4\pi b}\left[\pi - 2\tan^{-1}\left(\frac{1}{\eta_1}\right)\right]. \tag{7.6}$$

Correspondingly, the overall potential of the electrode B, denoted as V_B, that is induced by the current source and sink, and their particular images at electrodes A and B, respectively,

can be expressed as:

$$V_B = \frac{-\rho I}{4\pi b}\left[\pi - 2\tan^{-1}\left(\frac{1}{\eta_1}\right)\right]. \tag{7.7}$$

7.2.1.5 Potential difference between electrodes A and B

The potential difference between the two electrodes A and B, which is denoted as V, is obtained by taking the difference between (7.6) and (7.7), and expressed as:

$$V = \frac{\rho I}{2\pi b}\left[\pi - 2\tan^{-1}\left(\frac{1}{\eta_1}\right)\right]. \tag{7.8}$$

7.2.1.6 The theoretical geometric factor

Rearranging (7.8), the resistivity of the medium, $\rho_{2E,os}$, which is determined using the two-electrode method, when the planar disc electrodes are modelled in the oblate spheroidal coordinates is given:

$$\rho_{2E,os} = \left(K_{2E,os}\right)R \tag{7.9}$$

where $R = V/I$. The subscripts $2E$ and os denote two-electrode and oblate spheroidal, respectively. The geometric factor $K_{2E,os}$ is expressed as:

$$K_{2E,os} = \frac{2\pi b}{\pi - 2\tan^{-1}(1/\eta_1)} \tag{7.10}$$

with $\eta_1 = \sqrt{(d/b)^2 - 1}$, and b is the radius of the planar disc electrode.

7.3 Experimental Set-Up

Using the measurement system, the experiments were conducted to validate the proposed geometric factor using the two-electrode method, as shown in Fig. 7.3. The functions of the various components of the measurement system have been discussed in Section 4.4.

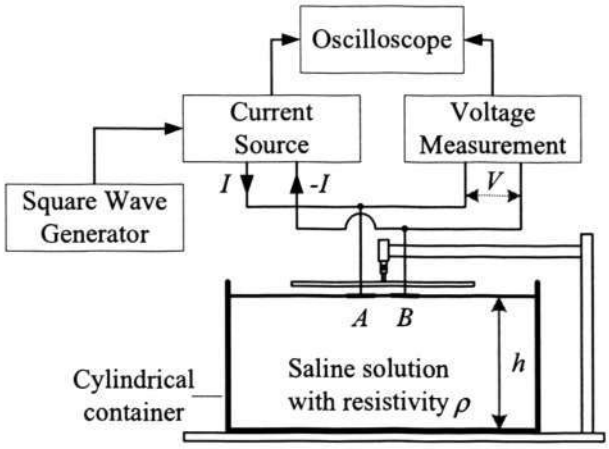

Figure 7.3 - The measurement system for experiments using the two-electrode method with planar disc electrodes. The current is injected into both electrodes *A* and *B*.

The test model consisted of a saline solution in a metallic grounded cylindrical container with a diameter of 400 mm. The maximum d used in the experiments was 30 mm. Since the current I was injected through both electrodes *A* and *B*, as shown in Fig. 7.3, both the OTAs inside the LM13700N were used to convert the square wave voltage into a two periodically-reversed direct currents, which were equal in magnitude but 180 degrees out of phase with each other, were generated. R was taken as the ratio of V to I, and the calculated resistivities obtained using the derived geometric factor were compared with the resistivities measured using the commercial conductivity meter.

7.3.1 Saline solutions

The saline solution was prepared by mixing common salt and water. Two saline solutions, 7*X* and 7*Y*, were prepared. The salt concentration of saline solutions 7*X* and 7*Y* were 5.0 g/litre and 0.5 g/litre, respectively; these concentrations are chosen to approximate that of resistivities of the blood. The resistivities of the saline solutions were measured using a commercial conductivity meter (YSI model EC300), which is shown in Fig. 4.8, so as to act as a reference for comparison. The resistivity that was obtained using the commercial conductivity meter is denoted by ρ_{cm}. The operations of the commercial conductivity meter were described in Section 4.5.1.

Using a thermometer (Fluke model FLU65), which is shown in Fig. 4.9, the temperature of the saline solution was measured to be 21 °C. All measurements were conducted when the saline solutions were at 21 °C.

7.3.2 Electrodes

The experiments were conducted using the two-electrode method, where two planar disc Ag/AgCl electrodes were used. The electrodes used in the experiments were purchased from A-M Systems, Inc., Carlsborg, USA. The diameter of the planar disc electrode was 4 mm. During the experiments, the bottom part of the disc electrode was just in contact with the saline solution, which was contained in a grounded metallic bath.

7.4 Experimental Procedures

Experiments were conducted for both saline solutions 7*X* and 7*Y*. Unless otherwise stated, *d* and *h* were maintained at 5 mm and 60 mm, respectively. It is worthwhile to note that in Chapter 6, the evaluation of the experimental results has shown that in experiments involving the two-electrode method with Ag/AgCl electrodes, a suitable frequency of the current source for the conduct of the experiments was 1 kHz upwards. In addition, the evaluation showed that the measured geometric factor was independent of the range of current density tested. The evaluation of the result showed that the measured resistance and subsequent calculated value of resistivity was independent of the period of time tested. The temperature dependence of the resistivity determined using the two-electrode method was also presented and discussed in Chapter 6.

Hence, for the experiments conducted in this chapter, they were conducted at a frequency of 3 kHz, whereby the effect of polarisation impedance was neglected and the measured *R* was equated to the bulk electrolyte resistance between the two electrodes. The effects of the current density, the measurement time and the temperature on the measured geometric factor, the measured resistance and the calculated resistivity will not be repeated in this Chapter as the results will be similar to those which have already been presented in Chapter 6. Nevertheless, the effects of the frequency, the current density and the temperature on the measured geometric factor, the measured resistance and the calculated resistivity using the two-electrode method with thin planar disc electrodes are reported in [161].

7.4.1 Effects of d and h on the calculated resistivity

The focus of the experiments in this chapter was the effects of varying d and h on $\rho_{2E,os}$. With h of 60 mm, the electrodes were first fixed at a particular d and then lowered into the saline solution by rotating the micrometer. The electrodes were immersed till the bottom part of the disc electrodes was just in contact with the saline solution and measurements were taken for the particular d. The above procedure was repeated as d was varied from 5 mm to 30 mm. Next, with d fixed at 5 mm, the measurements were taken as h was decreased in steps of 1 mm from 7 mm downwards.

7.5 Experimental Results and Discussion

Using the commercial conductivity meter, ρ_{cm} obtained for saline solutions 7X and 7Y were 1.211 $\Omega \cdot$m and 9.099 $\Omega \cdot$m, respectively.

7.5.1 Effects of d and h on the calculated resistivity

The measured R and the calculated $\rho_{2E,os}$ that were obtained as d was varied were tabulated in Tables 7.I and 7.II for saline solutions 7X and 7Y, respectively. The percentage difference $|\%\ \mathrm{Diff}|_8$ was obtained using

$$|\%\ \mathrm{Diff}|_8 = \left(\frac{\rho_{2E,os} - \rho_{cm}}{\rho_{cm}} \right) \times 100\% . \tag{7.11}$$

Table 7.I - The measured resistance and calculated resistivity as the inter-electrode spacing was varied for the saline solution 7*X*.

d (mm)	R (Ω)	$\rho_{2E,os}$ ($\Omega \cdot$ m)	$\lvert\%\ \mathrm{Diff}\rvert_8$
5	232	1.26	4.05
10	267	1.23	1.57
20	289	1.23	1.57
30	300	1.25	3.22

Table 7.II - The measured resistance and calculated resistivity as the inter-electrode spacing was varied for the saline solution 7*Y*.

d (mm)	R (kΩ)	$\rho_{2E,os}$ ($\Omega \cdot$ m)	$\lvert\%\ \mathrm{Diff}\rvert_8$
5	1.66	8.97	1.42
10	2.00	9.16	0.67
20	2.09	8.94	1.75
30	2.17	9.07	0.32

Tables 7.I and 7.II showed that as d was varied, the measured R remained fairly constant and both ρ_{cm} and the calculated $\rho_{2E,os}$ were in close agreement. The evaluation of the experimental results showed that the theoretical $K_{2E,os}$ was able to obtain an accurate value of resistivity for different combinations of d.

Next, the experimental results obtained as h was decreased in steps of 1 mm from 10 mm, with d maintained at 5 mm, were tabulated in Tables 7.III and 7.IV for saline solutions 7*X* and 7*Y*, respectively. The percentage difference $\lvert\%\ \mathrm{Diff}\rvert_8$ was obtained using (7.11).

Table 7.III - The measured resistance and calculated resistivity as the depth of the saline solution 7*X* was varied.

h (mm)	R (Ω)	$\rho_{2E,os}$ ($\Omega \cdot$ m)	$\lvert\%\ \mathrm{Diff}\rvert_8$
7	226	1.22	0.74
6	219	1.19	1.73
5	222	1.20	0.91
4	220	1.19	1.73
3	225	1.22	0.74

Table 7.IV - The measured resistance and calculated resistivity as the depth of the saline solution 7*Y* was varied.

h (mm)	R (kΩ)	$\rho_{2E,os}$ (Ω·m)	$\lvert\%\ \mathrm{Diff}\rvert_8$
7	1.68	9.10	0.01
6	1.67	9.03	0.76
5	1.69	9.14	0.45
4	1.67	9.04	0.65
3	1.68	9.10	0.01

Tables 7.III and 7.IV showed that as h was decreased in steps of 1 mm from 7 mm, the measured R remained fairly constant and both ρ_{cm} and $\rho_{2E,os}$ were in close agreement, where $\lvert\%\ \mathrm{Diff}\rvert_9 < 5\%$. The evaluation of the result showed that when b and d was 2 mm and 5 mm, respectively, a consistent resistivity of the medium was obtained even at a shallow h of 3 mm.

The ability of the proposed method in obtaining consistent resistivity even at small sample depth indicates its suitability for miniaturization. The ratio of $b:d:h$ is approximately 1:2.5:1.5 and if this ratio is maintained constant, the dimensions can be drastically scaled down to values even much smaller than those suggested in Fig. 7.4, even to the micrometer range for future fabrication of a microfluidic device for resistivity measurement of biofluids.

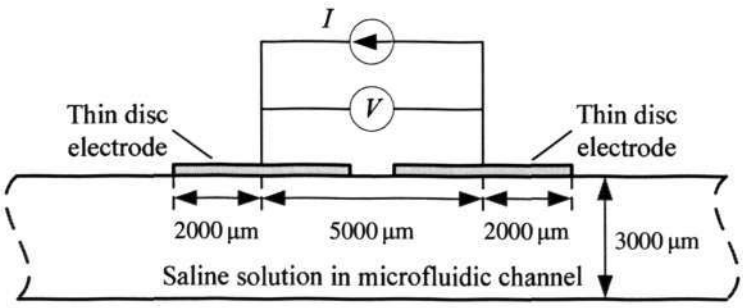

Figure 7.4 - Resistivity measurement of saline solution in an enlarged model of a microfluidic channel using two relatively non-polarizable planar disc electrodes.

It has been reported that there are variability in the impedance measurements of biological samples, when different electrode shapes were used for impedance spectroscopy

investigations [149, 162]. The observed variation in the impedance measurements can be attributed to, amongst others, the use of different electrode geometries. In order to complement the research work on impedance spectroscopy investigation of biofluids, the basic principle of the method and materials described in this work can be applied to microfluidic devices, which use planar interdigitated, parallel or circular electrodes [149, 162], so as to determine the resistivity of biofluids.

7.6 Concluding Remarks

In this chapter, a new geometric factor for resistivity measurement of ultra-small-volume sample using the two-electrode method by means of planar disc electrodes was derived and validated through experiments. The evaluation of the experimental results showed that consistent and accurate resistivity of the medium were obtained using relatively non-polarizable disc electrodes and the theoretically derived geometric factor when the inter-electrode spacing or the depth of the sample was varied. In particular, the resistivities of the saline solutions obtained using the derived geometric factors and those obtained using a commercial conductivity meter were both in good agreement even for small electrode radius, inter-electrode spacing and depth of sample, thus making it a promising technique for miniaturization for applications in microfluidic channels or devices. In addition, the proposed resistivity measurement technique presented in this chapter was able to obtain accurate resistivities even when the ratio of $d:h$ is 1:0.6, this is an improvement over the ratio of 1:1, which was achieved using the resistivity measurement technique presented in Chapter 6. The work pertaining to resistivity measurement using the two-electrode method with planar disc electrodes, which is reported in this chapter, has been accepted for publication in *IEEE Sensors J.* [161].

CHAPTER 8 - EFFECTS OF THE SET-UPS ON RESISTIVITY MEASUREMENT OF FINITE-VOLUME SAMPLES USING BOTH THE FOUR AND THE TWO-ELECTRODE METHODS

8.1 Overview

The use of both the four and the two-electrode methods for resistivity measurement in biomedical applications is studied in this chapter. It had been mentioned in Chapter 4 that currently, there exists a wide variation in the reported resistivities of the biological tissues in the literature and errors in the measurement set-ups is one of the reasons for the wide variation [2, 119]. The literature survey also revealed that for resistivity measurement using the four-electrode method [25], a number of different signals and measurement set-ups had been used in the past, such as:

(i) the waveform of the sources used, i.e., sinusoidal [4, 8, 22, 29, 40, 43] or periodically-reversed [5, 26, 27, 36, 41, 45, 119];

(ii) the method of storage of samples during the measurement process, i.e., in a Plexiglas/plastic/insulator container [4, 5, 28, 36, 40, 43, 45], in a metal container [119] or on a surgical table [47, 130]; and

(iii) the type of measurement, i.e., *in vivo* [12, 22, 26, 29, 47, 130] or *in vitro* [4, 5, 27, 28, 36, 40, 41, 43, 45].

In addition, the electrical property of the tissue that was being measured was provided with a ground reference in [26, 29]. In all the literature cited above, the current source was used as the stimulus. It is worthwhile to note that resistivity measurements were conducted using the

four-electrode method with the sample stored in a metal container [119] and a metallic tank in chapters 4 and 5, respectively. Resistivity measurements were also conducted using the two-electrode method in an insulator and a grounded metallic container in chapters 6 and 7, respectively. It is worthwhile to note that in the literature cited, measurements were conducted as the following parameters, i.e., the inter-electrode spacing [27, 29, 40, 45, 119] or the length of the immersed electrode [27, 28, 119] was varied. The effects of varying the inter-electrode spacing, the length of the immersed electrode and the depth of the medium on the measured resistivity obtained using both the four and the two-electrode methods were studied and reported in chapters 4 and 6, respectively. It is to be noted that throughout this chapter, the length of the immersed electrode is denoted by l_c and the inter-electrode spacing using both the four and the two-electrode methods is denoted by s and d, respectively.

The aim of the work in this chapter is to investigate the effects of the experimental set-ups on the measured resistivity, which is obtained using both the four and the two-electrode methods, with the derived $K_{4E,ps}$ in (4.14) and $K_{2E,ps}$ in (6.23), respectively, as the inter-electrode spacing or the length of the immersed electrode is varied.

This chapter is organised as follows. The various set-ups for resistivity measurement using both the four and the two-electrode methods, which are under investigation, are described in Section 8.2. Numerical simulations are conducted to study the potential plots obtained using the various set-ups in Section 8.3. The experimental set-up and procedures are presented in Section 8.4. The effects of the different set-ups on the measured resistivities are investigated. The experimental results on the calculated resistivity based on the different set-ups and the resistivity obtained using a commercial conductivity meter are then evaluated and compared in Section 8.5. The concluding remarks are given in Section 8.6.

8.2 Set-ups and Resistivity Calculations

8.2.1 The four-electrode method

8.2.1.1 Set-ups for resistivity measurement

Using the four-electrode method, six possible but different set-ups as shown in Table 8.I are first discussed. The conceptual representation of set-ups C_1, C_3 and C_5 is shown in Fig. 8.1(a) whereas the conceptual representation of set-ups C_2, C_4 and C_6 is shown in Fig. 8.1(b).

Table 8.I – Possible set-ups for the four-electrode method.

Set-up	V_A	V_D	I_A	I_D	$(V_B - V_C)$	Container
C_1	Float	Float	$+I$	$-I$	V	Grounded conductor
C_2	Float	Gnd*	$+I$	$-pI$**	V	Grounded conductor
C_3	Float	Float	$+I$	$-I$	V	Ungrounded conductor
C_4	Float	Gnd*	$+I$	$-I$	V	Ungrounded conductor
C_5	Float	Float	$+I$	$-I$	V	Insulator
C_6	Float	Gnd*	$+I$	$-I$	V	Insulator

Note: Gnd* – Electrode D is grounded, $-pI$** – $p < 1$.

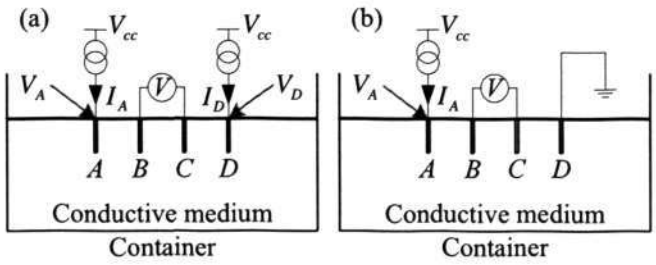

Figure 8.1 - Conceptual representation for set-ups (a) C_1, C_3 and C_5 and (b) C_2, C_4 and C_6 for the four-electrode method. (Note: V_{cc} is the supply voltage).

For set-ups C_1, C_3 and C_5, two periodically-reversed direct currents, which are equal in magnitude but 180 degrees out of phase with each other, are generated; the leads from these

generated currents are then connected to electrodes A and D, i.e., $+I$ and $-I$ are flowing in electrodes A and D, respectively. For set-ups C_2, C_4 and C_6, the electrode D is grounded and $+I$ is flowing in the electrode A. However, it is noted that in the set-up C_2, both the container and the electrode D are grounded, hence, the current is recollected at the container, as well as the electrode D. For set-ups C_4 and C_6, only the electrode D is grounded, hence all the current injected through the electrode A is recollected at the electrode D, i.e., $-I$ is flowing in the electrode D.

In the measurement system used by Rush *et al.* in [26], a controlled current flowed into and out of the sample under study by means of two outer electrodes. The sample that was being measured was grounded at points that were located far away from the measuring electrodes. Since the current at electrodes A and D were $+I$ and $-I$, respectively, and the sample was grounded at locations distant from the measuring electrodes, the set-up used by Rush *et al.* is similar to the set-up C_1. In the measurement system described in Chapter 4 and [119], a current was injected into the electrode A and the electrode D was grounded. Measurements were conducted on samples in an ungrounded metallic container. Since only the electrode D was grounded, hence all the current injected into the electrode A was recollected at the electrode D. Since $+I$ and $-I$ were flowing in electrodes A and D, respectively, and the measurements were conducted in an ungrounded conductor container, the set-ups described in Chapter 4 and [119] are similar to the set-up C_4. In the measurement systems used by Tsai *et al.* in [28] and Haemmerich *et al.* in [12], a current was injected into the electrode A and the electrode D was grounded. Measurements were conducted on samples in a plastic container. Since only the electrode D was grounded, all the current injected into the electrode A was recollected at the electrode D i.e., $+I$ and $-I$ were flowing in electrodes A and D, respectively. Measurements were also conducted in an insulator container, hence the set-ups used by Tsai *et al.* and Haemmerich *et al.* are similar to the set-up C_6.

At this juncture, it is worthwhile to note that not all the six possible set-ups are suitable for resistivity measurements using the four-electrode method. For set-ups C_3 and C_5, it was noted that there was no ground for the potential in the measurement set-ups. Consequently, the models for both set-ups C_3 and C_5 were not uniquely defined as the potential was not measured with reference to any specific ground. Hereafter, both set-ups C_3 and C_5 were considered as not suitable for the study.

8.2.1.2 Resistivity calculations

As noted in Chapter 4, using the four-electrode method, the resistivity can be calculated using (4.1), (4.2) or (4.13). Both the four and the two-electrode methods were used to measure the resistivity in this chapter. Hence, so as to ensure a consistency in the techniques used to calculate the resistivity, both the geometric factors used for the resistivity calculation using the two methods were based on those derived in the prolate spheroidal coordinates. Therefore, using the four-electrode method, the resistivity $\rho_{4E,\,ps}$ was calculated using (4.13) [119]:

$$\rho_{4E,\,ps} = \left(K_{4E,\,ps}\right)R$$

where $K_{4E,\,ps} = \dfrac{2\pi l_c}{\left(\dfrac{1}{n}\right)\sum_{i=1}^{n} \ln\left[\left(\dfrac{\eta_{1,i}+1}{\eta_{1,i}-1}\right)\left(\dfrac{\eta_{2,i}-1}{\eta_{2,i}+1}\right)\right]}$,

$$\eta_{1,i} = \sqrt{\frac{\left(l_c^{\,2}+s^2+z_i^{\,2}\right)+\sqrt{\left(l_c^{\,2}+s^2+z_i^{\,2}\right)^2-4l_c^{\,2}z_i^{\,2}}}{2l_c^{\,2}}},$$

$$\eta_{2,i} = \sqrt{\frac{\left(l_c^{\,2}+4s^2+z_i^{\,2}\right)+\sqrt{\left(l_c^{\,2}+4s^2+z_i^{\,2}\right)^2-4l_c^{\,2}z_i^{\,2}}}{2l_c^{\,2}}},$$

$z_i = l_c(2i-1)/2n$, the number of segments n was 10, and the measured resistance $R = V/I$. The subscripts $4E$ and ps denote four-electrode and prolate spheroidal, respectively.

8.2.2 The two-electrode method

8.2.2.1 Set-ups for resistivity measurement

Using the two-electrode method, where a simplified equivalent circuit model for the two-electrode method is shown in Fig. 6.2, six possible but different set-ups as shown in Table 8.II are first discussed. The conceptual representation of set-ups C_1, C_3 and C_5 is shown in Fig. 8.2(a) whereas the conceptual representation of set-ups C_2, C_4 and C_6 is shown Fig. 8.2(b).

Table 8.II – Possible set-ups for the two-electrode method.

Set-up	V_A	V_B	I_A	I_B	$(V_A - V_B)$	Container
C_1	Float	Float	$+I$	$-I$	V	Grounded conductor
C_2	Float	Gnd*	$+I$	$-pI$**	V	Grounded conductor
C_3	Float	Float	$+I$	$-I$	V	Ungrounded conductor
C_4	Float	Gnd*	$+I$	$-I$	V	Ungrounded conductor
C_5	Float	Float	$+I$	$-I$	V	Insulator
C_6	Float	Gnd*	$+I$	$-I$	V	Insulator

Note: Gnd* – Electrode B is grounded, $-pI$** – $p < 1$.

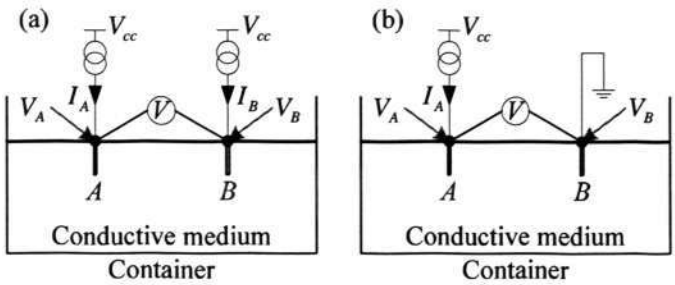

Figure 8.2 - Conceptual representation for set-ups (a) C_1, C_3 and C_5 and (b) C_2, C_4 and C_6 for the two-electrode method. (Note: V_{cc} is the supply voltage).

As discussed earlier, not all the six possible set-ups are suitable for resistivity measurements

using the two-electrode method. It was noted that both set-ups C_3 and C_5 had no ground for the potential in the measurement set-ups. Consequently, both set-ups C_3 and C_5 were considered as not suitable for the study. Applications where the current I was injected to the electrode A and recollected at the electrode B were given in Chapter 6; these are applicable for set-ups C_2, C_4 and C_6. For set-ups C_1, C_3 and C_5, two periodically-reversed direct currents, which are equal in magnitude but 180 degrees out of phase with each other, are generated; the leads from these generated currents are then connected to electrodes A and B, i.e., $+I$ and $-I$ are supplied to electrodes A and B, respectively, as applied in Chapter 7. For set-ups C_2, C_4 and C_6, the electrode B is grounded.

8.2.2.2 Resistivity calculations

As noted in Chapter 6, using the two-electrode method, the resistivity can be calculated using (6.12) or (6.22). It has been described in Section 8.2.1.2 that the resistivities are to be calculated using geometric factors which were derived in the prolate spheroidal coordinates. Hence, using the two-electrode method, the resistivity $\rho_{2E,\,ps}$ was calculated using (6.22):

$$\rho_{2E,\,ps} = \left(K_{2E,\,ps}\right)R$$

$$\text{where : } K_{2E,\,ps} = \frac{2\pi l_c}{\left(\frac{1}{n}\right)\sum_{i=1}^{n}\ln\left[\left(\frac{\eta_0+1}{\eta_0-1}\right)\left(\frac{\eta_{1,i}-1}{\eta_{1,i}+1}\right)\right]},$$

$$\eta_0 = \sqrt{1+1.5\left(r_c/l_c\right)^2}\,,\quad \eta_{1,i} = \sqrt{\frac{\left(l_c^{\,2}+d^2+z_i^{\,2}\right)+\sqrt{\left(l_c^{\,2}+d^2+z_i^{\,2}\right)^2-4l_c^{\,2}z_i^{\,2}}}{2l_c^{\,2}}},$$

$z_i = l_c(2i-1)/2n$, r_c is the radius of the slender cylindrical electrode, the number of segments n was 10, and $R = V/I$. The subscripts $2E$ and ps denote two-electrode and prolate spheroidal, respectively.

8.3 Numerical Simulations on the Different Set-ups

From the analytical analysis described in Section 8.2, the set-ups, which are suitable for both the four and the two-electrode methods, are set-ups C_1, C_2, C_4 and C_6. Using the simulation software Maxwell SV from Ansoft Corporation [163], the potential distributions obtained using set-ups C_1, C_2, C_4 and C_6 were simulated and shown in Figs. 8.3(a), 8.3(b), 8.3(c) and 8.3(d), respectively.

In the numerical simulations, the potential of electrodes A and D is +1 V and -1 V, respectively. In set-ups C_1 and C_2, the containers were grounded conductors. In set-ups C_4 and C_6, the container was an ungrounded conductor and an insulator, respectively.

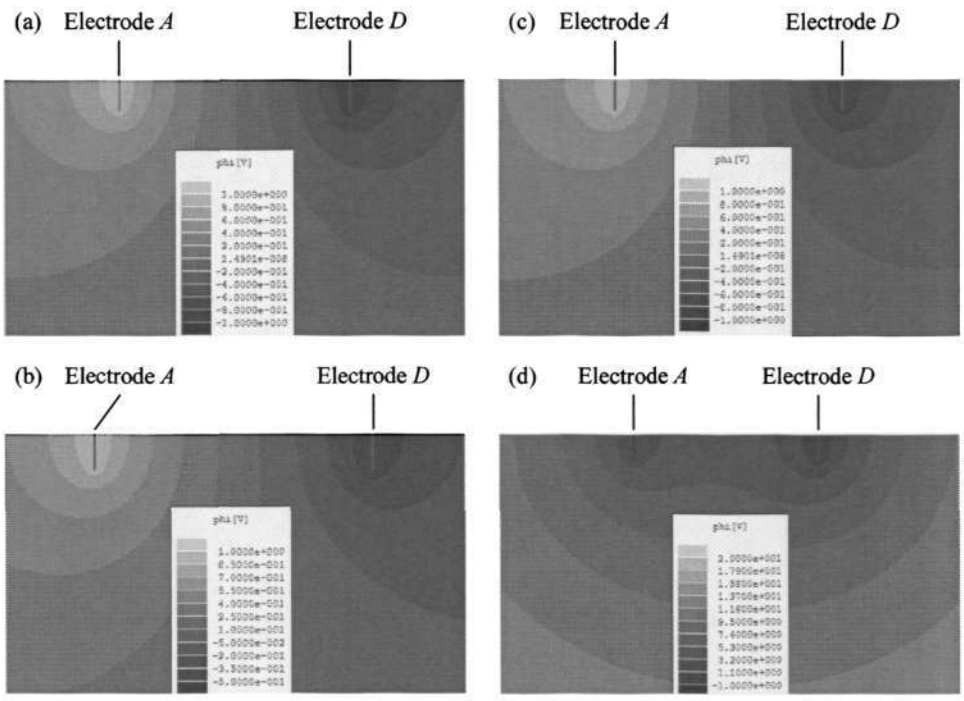

Figure 8.3 - Plots of potential distribution simulated using the set-ups (a) C_1, (b) C_2, (c) C_4 and (d) C_6, for both the four and the two-electrode methods. For the two-electrode method, the text "Electrode D" is replaced by the text "Electrode B".

In set-ups C_1, C_4 and C_6 for resistivity measurements using the four-electrode method, the currents flowing through electrodes A and D were $+I$ and $-I$, respectively. In the set-up C_2, as the current was recollected at the grounded container, as well as at the grounded electrode D, it was assumed that equal amount of current flowed through the container and the electrode D. Hence, in the set-up C_2, the currents flowing through electrodes A and D were $+I$ and $-0.5I$, respectively. It is to be noted that the above analysis is also applicable for set-ups C_1, C_2, C_4 and C_6 for resistivity measurements using the two-electrode method, with the electrode D replaced by the electrode B.

The simulation results showed that the potential distributions obtained for set-ups C_1 and C_4 were the same in terms of the flow pattern and the absolute values. In contrast, the potential distribution obtained using the set-up C_2 was different from those obtained using set-ups C_1 and C_4 in terms of the absolute values. The potential distribution obtained using the set-up C_6 was also different from those obtained using set-ups C_1 and C_4 in terms of both the flow pattern and the absolute values. In addition, it is noted that the potential that was induced on the surface of the electrodes were the same for set-ups C_1, C_4 and C_6.

From the evaluation of the simulation results, it is inferred that for resistivity measurement using the four-electrode method, the resistivities obtained using set-ups C_1 and C_4 are expected to be the same, whereas the resistivities obtained using set-ups C_2 and C_6 are expected to be different from those that are obtained using set-ups C_1 and C_4. The reason is that the resistivity determined using the four-electrode method is dependent on the voltage differences between electrodes B and C, which are located in between electrodes A and D. The voltages of electrodes B and C are in turn dependent on the potential distribution in the regions between electrodes A and D.

In addition, from the evaluation of the simulation results, it is also inferred that for resistivity measurement using the two-electrode method, the resistivities obtained using set-ups C_1, C_4 and C_6 are expected to be the same, whereas the resistivities obtained using the set-up C_2 is expected to be different from those that are obtained using set-ups C_1, C_4 and C_6. The reason is that the resistivity determined using the two-electrode method is dependent on the voltages that are induced on electrodes A and B, which are independent of the potential distribution in the regions between electrodes A and B.

8.4 Experimental Set-Up and Procedures

From the numerical simulations performed in Section 8.3, it is expected that for the four-electrode method, the resistivities obtained using set-ups C_1 and C_4 are expected to be the same, whereas the resistivities obtained using set-ups C_2 and C_6 are expected to be different from those obtained using set-ups C_1 and C_4. For the two-electrode method, the resistivities obtained using set-ups C_1, C_4 and C_6 are expected to be the same, whereas the resistivity obtained using the set-up C_2 is expected to be different from those obtained using set-ups C_1, C_4 and C_6.

In this section, the experiments were conducted on a test model to validate the results obtained from the numerical simulations and also to determine the proper set-ups for accurate resistivity measurement using both the four and the two-electrode methods. The experiments were conducted using a measurement system, as the inter-electrode spacing or the length of the immersed electrode was varied using both the four and the two-electrode methods. The test model consisted of a saline solution in a cylindrical container with a diameter of 400 mm. The functions of the various components of the measurement system have been discussed in Section 4.4. The maximum s and d used in the experiments were both 30 mm.

8.4.1 Saline solutions

The saline solution was prepared by mixing common salt and water. Two saline solutions, 8*X* and 8*Y*, were prepared. The salt concentration of saline solutions 8*X* and 8*Y* were 2.5 g/litre, and 0.067 g/litre, respectively; these concentrations were chosen to approximate that of biological tissues. The resistivities of the saline solutions were measured using the commercial conductivity meter (YSI model EC300), which is shown in Fig. 4.8, so as to act as a reference for comparison. The resistivity that was obtained using the commercial conductivity meter was denoted by ρ_{cm}. The operations of the commercial conductivity meter were described in Section 4.5.1.

All measurements were conducted when the saline solutions were at 21 °C, measured using a thermometer (Fluke model FLU65), which is shown in Fig. 4.9. Unless otherwise stated, the depth h of the saline solution was maintained at 60 mm throughout the experiments.

8.4.2 Electrodes

The experiments were conducted using both the four and the two-electrode methods, with four slender cylindrical Ag and two slender cylindrical Ag/AgCl electrodes, respectively. The electrodes were purchased from A-M Systems, Inc., Carlsborg, USA. The diameters of the Ag and Ag/AgCl electrodes were measured using a digimatic calliper (Mitutoyo model CD-6" CsX), which is shown in Fig.4.10, and found to be 0.38 mm and 0.51 mm, respectively.

8.4.3 Experimental procedures

The experiments described hereafter in this section were conducted for both saline solutions $8X$ and $8Y$. Both the four and the two-electrode methods were used to determine the resistivities of the saline solutions. The measurements were conducted using the four set-ups, C_1, C_2, C_4 and C_6, which were considered suitable for the study. First, using the four-electrode method, the electrodes with s first fixed at 5 mm, were lowered into the saline solution by means of a micrometer until l_c was 2 mm. Measurements were then taken for this particular combination of s and l_c. The measurement was repeated as l_c was varied from 2 mm to 5 mm and s was varied from 5 mm to 30 mm.

Next, the above procedures were repeated using the two-electrode method as l_c was varied from 2 mm to 5 mm and d was varied from 5 mm to 30 mm.

8.5 Experimental Results and Discussion

Using the commercial conductivity meter, ρ_{cm} obtained for saline solutions $8X$ and $8Y$ were 2.066 $\Omega \cdot$ m and 40.58 $\Omega \cdot$ m, respectively.

8.5.1 Experimental results for the four-electrode method

As l_c was fixed at 2 mm and s was varied from 5 mm to 30 mm, the resistivities for saline solutions $8X$ and $8Y$ under the different set-ups were calculated and tabulated as shown in Table 8.III. In addition, the calculated resistivities for saline solutions $8X$ and $8Y$ were plotted as shown in Figs. 8.4(a) and 8.4(b), respectively.

Table 8.III - Calculated resistivities of saline solutions 8*X* and 8*Y* using the different set-ups as the inter-electrode spacing was varied.

	$\rho\ (\Omega \cdot \mathrm{m})$							
	Saline solution 8*X*				Saline solution 8*Y*			
s (mm)	C_1	C_2	C_4	C_6	C_1	C_2	C_4	C_6
5	2.03	1.10	2.01	2.01	39.9	21.4	39.7	39.6
10	2.01	1.13	2.00	2.03	40.8	20.7	40.8	41.2
20	2.02	1.15	2.03	2.39	40.0	23.1	40.1	43.0
30	2.05	1.26	2.04	2.70	40.4	23.7	39.9	48.4

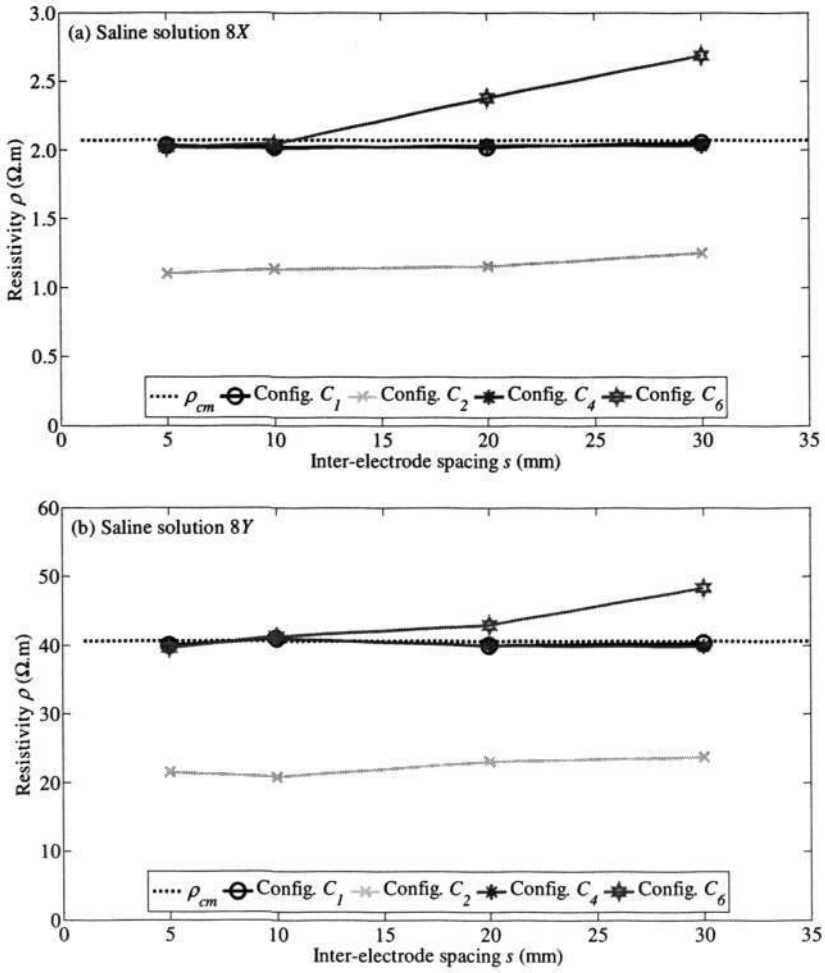

Figure 8.4 - Plot of the calculated resistivity using the four-electrode method as the inter-electrode spacing was varied for saline solutions (a) 8*X* and (b) 8*Y*.

The evaluation of the experimental results showed that when s was small, e.g., 5 mm, the calculated resistivities of the saline solutions remained fairly constant and were in agreement with ρ_{cm} for all the set-ups except the set-up C_2. However, as s was varied, the calculated saline resistivities remained fairly constant and were in good agreement with ρ_{cm} only for set-ups C_1 and C_4. For the set-up C_2, the calculated resistivities do not agree with ρ_{cm}, whereas for the set-up C_6, the calculated resistivities deviated from ρ_{cm} when s was varied.

As s was fixed at 20 mm and l_c was varied from 2 mm to 5 mm, the resistivities for saline solutions 8X and 8Y under the different set-ups were calculated and tabulated as shown in Table 8.IV. In addition, the calculated resistivities for saline solutions 8X and 8Y were plotted as shown in Figs. 8.5(a) and 8.5(b), respectively.

Table 8.IV - Calculated resistivities of saline solutions 8X and 8Y using the different set-ups as the length of the immersed electrode was varied.

	ρ (Ω·m)							
	Saline solution 8X				Saline solution 8Y			
l_c (mm)	C_1	C_2	C_4	C_6	C_1	C_2	C_4	C_6
2	2.02	1.15	2.03	2.39	40.0	23.1	40.1	43.0
3	2.04	1.09	2.03	2.38	39.7	23.2	40.1	42.3
4	2.03	1.09	2.02	2.34	41.2	23.1	41.0	42.1
5	2.03	1.08	2.02	2.31	39.8	22.7	40.1	41.5

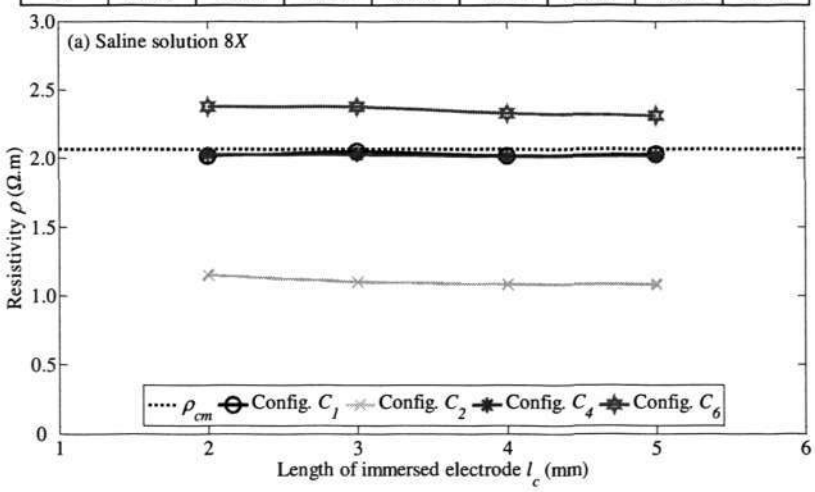

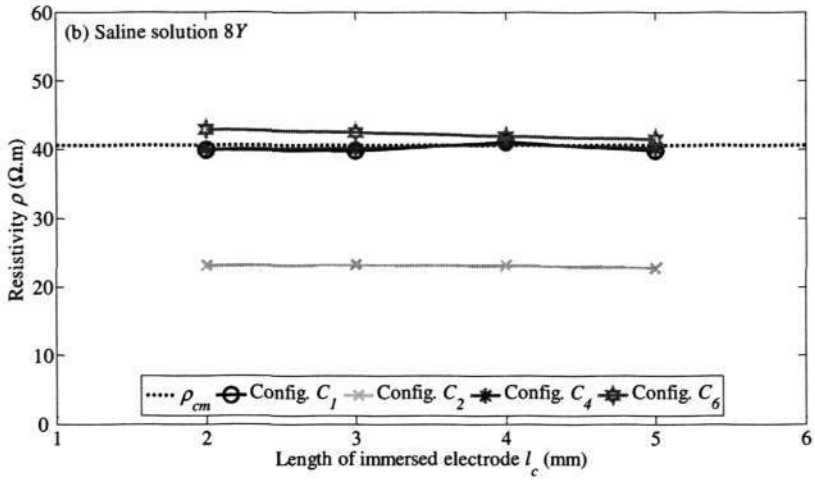

Figure 8.5 - Plot of the calculated resistivity using the four-electrode method as the length of the immersed electrode was varied for saline solutions (a) 8*X* and (b) 8*Y*.

The evaluation of the experimental results showed that when either l_c was small with a large *s*, i.e., at l_c = 2 mm and *s* = 20 mm, or when l_c was varied, the calculated saline resistivities remained fairly constant and were in good agreement with ρ_{cm} only for set-ups C_1 and C_4, whereas for set-ups C_2 and C_6., the calculated resistivities do not agree with ρ_{cm}.

8.5.2 Discussions for the four-electrode method

From the evaluation of the experimental results, it was observed that for all the set-ups, with the exception of the set-up C_2, an accurate resistivity of the saline solution was obtained for specific parameters of *s* and l_c. One example as shown in the results was when *s* and l_c were maintained at 5 mm and 2 mm, respectively. However, it was also noted that the above observation do not remain true when either one of the parameter *s* or l_c was varied. When either *s* or l_c was varied, an accurate resistivity was only obtained using the set-ups C_1 and C_4.

It was inferred from the numerical simulation results in Section 8.3 that the resistivities obtained using set-ups C_1 and C_4 were expected to be the same. These numerical simulation results were validated from the evaluation of the experimental results, where it was shown that when either s or l_c was varied, the resistivities obtained using set-ups C_1 and C_4 were the same and they were also in good agreement with ρ_{cm}.

In addition, the numerical simulation results in Section 8.3 also inferred that the resistivities obtained using set-ups C_2 and C_6 were expected to be the different from those obtained using set-ups C_1 and C_4. This observation was again validated from the evaluation of the experimental results, where it was shown that when either s or l_c was varied, the resistivities obtained using set-ups C_2 and C_6 were different from those obtained using set-ups C_1 and C_4 and they were also not in good agreement with ρ_{cm}.

An investigation into the cause of these discrepancies is in order. When measurements are conducted using the four-electrode method as either s or l_c is varied, it is of significant importance to obtain an ideal potential distribution. This is because the calculated resistivity is dependent on the potential difference obtained between electrodes B and C, which is in turn dependent on the potential distribution located at intervals in the regions between electrodes A and D.

It is worthwhile to note that the ideal potential distribution obtained using the four-electrode method, as either s or l_c is varied, is based on the following circumstances:

(i) current is injected using two outer electrodes A and D, i.e., the currents at electrodes A and D are $+I$ and $-I$, respectively, and

(ii) potential at the far field is zero, this can be modelled by grounding the boundary of the container.

All the above circumstances were found in the set-up C_1, hence the potential distribution obtained using the set-up C_1 was the same as the ideal potential distribution as either s or l_c was varied. It was shown in the numerical simulations in Section 8.3 that the potential distributions obtained using set-ups C_1 and C_4 were the same in terms of the flow pattern and the absolute values. For the set-up C_4, the current was injected at the electrode A, the electrode D was grounded and measurements were conducted in a metal container. As only the electrode D was grounded in the measurement set-up, all the current that was injected at the electrode A was recollected at the electrode D, thus the currents at the electrodes A and D were $+I$ and $-I$, respectively. Moreover, as the measurement was conducted in a metal container, where the resistivity of the metal container is very low, the potential at the far field was almost zero. Hence the potential distribution obtained using the set-up C_4 was the same as the ideal potential distribution, which was obtained using the set-up C_1, as either s or l_c was varied.

In addition, it was shown in the numerical simulations in Section 8.3 that the potential distributions obtained using set-ups C_2 and C_6 were different from the ideal potential distribution obtained using the set-up C_1. For the set-up C_2, both the electrode D and the container were grounded, hence the current that was injected at the electrode A was recollected at the electrode D, as well as at the container, consequently the potential distribution obtained using the set-up C_2 was different from the ideal potential distribution obtained using the set-up C_1, as either s or l_c was varied. For the set-up C_6, as the measurement was conducted in an insulator container, the potential at the far field was not zero. Hence the potential distribution obtained using the set-up C_6 was different from the ideal potential distribution obtained using the set-up C_1, as either s or l_c was varied.

In summary, the evaluation of the experimental results showed that an inaccurate resistivity was obtained using the four-electrode method with set-ups C_2 and C_6 when either s or l_c was varied. In contrast, the evaluation showed that an accurate resistivity measurement was obtained with set-ups C_1 and C_4 for the following tested situations:

(i) when l_c was fixed and s was varied from 5 mm to 30 mm, or

(ii) when s was fixed and l_c was varied from 2 mm to 5 mm.

8.5.3 Experimental results for the two-electrode method

As l_c was fixed at 2 mm and d was varied from 5 mm to 30 mm, the resistivities for saline solutions 8X and 8Y under the different set-ups were calculated and tabulated as shown in Table 8.V. In addition, the calculated resistivities for saline solutions 8X and 8Y were plotted as shown in Figs. 8.6(a) and 8.6(b), respectively.

Table 8.V - Calculated resistivities of saline solutions 8X and 8Y using the different set-ups as the inter-electrode spacing was varied.

	ρ ($\Omega \cdot$m)							
	Saline solution 8X				Saline solution 8Y			
d (mm)	C_1	C_2	C_4	C_6	C_1	C_2	C_4	C_6
5	2.10	1.06	2.10	2.08	41.2	21.8	41.1	41.2
10	2.06	1.04	2.00	2.02	39.6	21.5	40.2	40.6
20	2.04	1.04	2.05	2.04	41.4	21.9	41.1	41.4
30	2.01	1.07	2.08	2.01	40.3	21.6	40.0	40.3

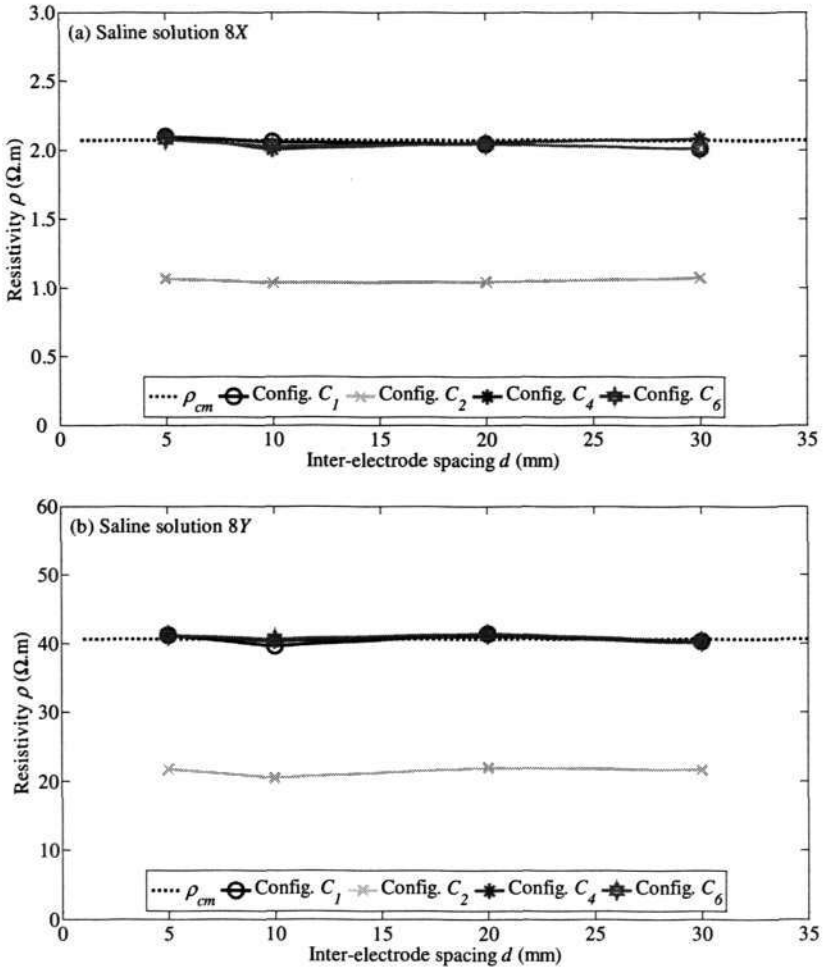

Figure 8.6 - Plot of the calculated resistivity using the two-electrode method as the inter-electrode spacing was varied for saline solutions (a) 8*X* and (b) 8*Y*.

The evaluation of the experimental results showed that as d was varied, the calculated resistivities of saline solutions 8*X* and 8*Y* remained fairly constant and were in agreement with ρ_{cm} for all the set-ups except the set-up C_2.

As d was fixed at 20 mm and l_c was varied from 2 mm to 5 mm, the resistivities for saline solutions 8*X* and 8*Y* under the different set-ups were calculated and tabulated as shown in Table 8.VI. In addition, the calculated resistivities for saline solutions 8*X* and 8*Y* were plotted as shown in Figs. 8.7(a) and 8.7(b), respectively.

Table 8.VI - Calculated resistivities of saline solutions 8*X* and 8*Y* using the different set-ups as the length of the immersed electrode was varied.

	$\rho\ (\Omega \cdot \mathrm{m})$							
	Saline solution 8*X*				Saline solution 8*Y*			
l_c (mm)	C_1	C_2	C_4	C_6	C_1	C_2	C_4	C_6
2	2.04	1.04	2.05	2.08	41.4	21.9	41.1	41.4
3	2.12	1.06	2.06	2.01	40.1	21.8	40.0	41.1
4	2.06	1.06	2.09	2.07	39.6	20.9	40.0	39.9
5	2.07	1.03	2.04	2.08	40.2	21.7	40.6	41.2

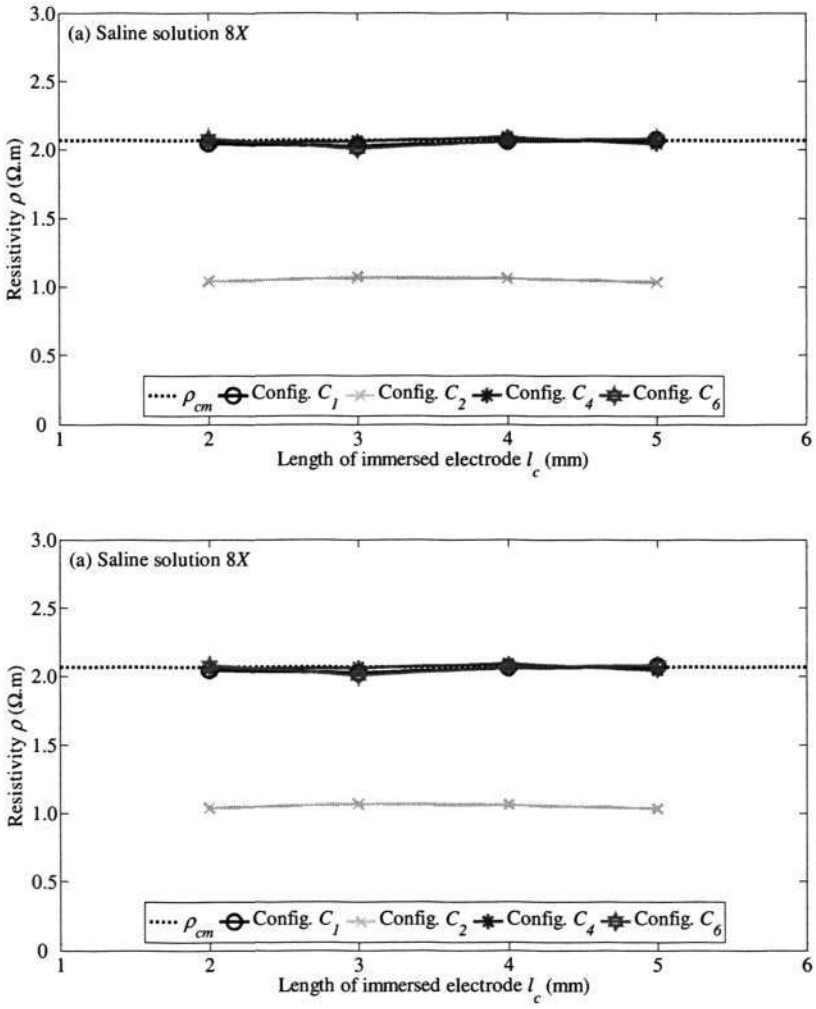

Figure 8.7 - Plot of the calculated resistivity using the two-electrode method as the length of the immersed electrode was varied for saline solutions (a) 8*X* and (b) 8*Y*.

The evaluation of the experimental results showed that as l_c was varied, the calculated resistivities of the saline solutions $8X$ and $8Y$ remained fairly constant and were in agreement with ρ_{cm} for all the set-ups except the set-up C_2.

8.5.4 Discussions for the two-electrode method

It was inferred from the numerical simulation results in Section 8.3 that the resistivities obtained using set-ups C_1, C_4 and C_6 were expected to be the same. These numerical simulation results were validated from the evaluation of the experimental results, where it was shown that when either d or l_c was varied, the resistivities obtained using set-ups C_1, C_4 and C_6 were the same and they were also in good agreement with ρ_{cm}. In addition, the numerical simulation results also inferred that the resistivity obtained using the set-up C_2 was expected to be the different from those obtained using set-ups C_1, C_4 and C_6. This observation was again validated from the evaluation of the experimental results, where it was shown that when either d or l_c was varied, the resistivity obtained using the set-up C_2 was different from those obtained using set-ups C_1, C_4 and C_6 and it was also not in good agreement with ρ_{cm}.

An investigation into the cause of the discrepancy for the set-up C_2 is in order. When measurements were conducted using the two-electrode method as either d or l_c was varied, the important point to take note is that the currents at the source and the sink electrodes were $+I$ and $-I$, respectively. This is because the potential difference measured using the two-electrode method is based on the self- and the mutual potential of the electrodes A and B, which was induced by the currents at the electrodes A and B.

All the above circumstances were found in set-ups C_1, C_4 and C_6. For the set-up C_1, currents were injected into electrodes A and B with the sample measured in a grounded metallic

container. For set-ups C_4 and C_6, the current was injected at the electrode A, the electrode B was grounded and measurements were conducted in a container that is not grounded. As only the electrode B was grounded in the measurement set-ups, all the current that was injected at the electrode A was recollected at the electrode B, thus the currents at the electrodes A and B were $+I$ and $-I$, respectively. For the set-up C_2, both the electrode B and the container were grounded and consequently, the current at the electrode B was not $-I$.

In summary, from the evaluation of our experimental results, it was observed that for all the suitable set-ups that were under study, with the exception of the set-up C_2, an accurate resistivity of the saline solution was obtained for the following situations:

(i) when l_c was fixed and d was varied from 5 mm to 30 mm, or

(ii) when d was fixed and l_c was varied from 2 mm to 5 mm.

8.6 Concluding Remarks

In this chapter, the effects of the different set-ups for the resistivity measurements of finite-volume samples by means of both the four and the two-electrode methods were studied. The evaluation of the experimental results highlighted the proper set-ups for the different experimental circumstances. In addition, the evaluation showed that when the proper set-ups were used, the saline resistivities that were obtained using the commercial conductivity meter and the derived geometric factors were both in good agreement and remained consistent, even when the inter-electrode spacing or the length of the immersed electrode was varied. Since resistivity measurement may be carried out under various experimental circumstances, knowledge of the proper set-up to be used is therefore important as it allows one to be able to accurately determine the resistivity of the conductive medium.

CHAPTER 9 - CONCLUSION AND RECOMMENDATION

9.1 Conclusion

The limitations of the currently used techniques for the resistivity measurement of conductive media and the determination of the parameters of a two-layer soil model were discussed in this thesis. The resistivity measured using the two-electrode method was reported to be affected by the effect of the electrode polarisation impedance. In addition, the resistivity measured using the commonly used four-electrode method was also known to be inaccurate when the sample size was small. It had also been shown that the depth of the first layer of a two-layer model estimated using the Sunde's graphical method was not unique and not in good agreement with the measured depth of the first layer.

In this thesis, a theoretical and experimental study on some aspects of resistivity measurement of conductive media using both the four and the two-electrode methods was reported. Conductive media with both small and ultra-small-volume samples were of particular interest, where such samples are often encountered in the biomedical and microfluidics applications. A novel geometric factor, derived in the prolate spheroidal coordinates, for the *in situ* resistivity measurement using the four-electrode method with slender cylindrical electrodes was proposed and experimentally validated. The evaluation of the experimental results showed that the saline resistivities that were obtained using a commercial conductivity meter and the proposed geometric factor were both in good agreement as the inter-electrode spacing or the length of immersed electrode was varied. In particular, a percentage error of less than 5% was achieved even when the length of the immersed electrode was comparable with or larger than the inter-electrode spacing, which was an improvement over the results obtained using the

conventional geometric factors proposed by Wenner and Baishiki, which were derived based on the modelling of the electrodes as points and slender cylinders, respectively. In addition, the evaluation of the experimental results also showed that the resistivity obtained using the four-electrode method was not affected by the sample size when the depth of the sample was at least or equal to four times the inter-electrode spacing.

A new technique incorporating more accurate resistivity data, which is an improvement over the conventional Sunde's graphical method, was proposed for the determination of the parameters of a two-layer soil model. From scale-model experiments conducted on two-layer model of saline solutions and agar in an electrolytic tank, the proposed measurement technique has been shown to obtain a more accurate two-layer soil model. In addition, the evaluation of the experimental results showed that the depth of the first layer estimated using the proposed measurement technique was more accurate than the depth estimated using the conventional Sunde's graphical method.

Next, novel geometric factors, derived in the prolate spheroidal and the cylindrical coordinates, for the *in situ* resistivity measurement of small-volume sample of conductive media using the two-electrode method with slender cylindrical silver-silver chloride electrodes were proposed and experimentally validated. The evaluation of the experimental results showed that the saline resistivities determined using the derived geometric factors and a commercial conductivity meter were both in good agreement when the inter-electrode spacing, the length of the immersed electrode or the depth of sample was varied. In addition, the proposed two-electrode measurement technique with slender cylindrical electrodes was able to obtain accurate resistivity even when the ratio of the inter-electrode spacing to the depth of the sample was 1:1. The ability of the proposed measurement technique in obtaining accurate resistivity for small-volume samples is important as small-volume samples are often encountered in biomedical applications.

An enhancement for the resistivity measurement of small-volume samples using the two-electrode method with slender cylindrical electrodes was presented next. A new geometric factor, derived in the oblate spheroidal coordinates, for the resistivity measurement of ultra-small-volume samples of conductive media using the two-electrode method with planar disc silver-silver chloride electrodes was proposed and experimentally validated. The evaluation of the experimental results showed that the resistivities of the saline solutions determined using the derived geometric factor and a commercial conductivity meter were both in good agreement even when the inter-electrode spacing, electrode radius and the depth of sample were small. These results showed that the proposed measurement method is a promising measurement technique of biofluids for applications in microfluidics devices. Furthermore, the proposed two-electrode measurement technique with planar disc electrodes was shown to obtain accurate resistivity even when the ratio of the inter-electrode spacing to the depth of the sample was 1:0.6, this is an improvement over the ratio of 1:1, which was achieved when the slender cylindrical electrodes were used instead of the planar disc electrodes. It is worthwhile to note that the effectiveness of the working of the two-electrode method, where a simplified equivalent circuit model of it is shown in Fig. 6.2, is dependent on the methods used to minimize the effects of the electrode-electrolyte impedance, as described in Chapter 6.

Finally, since errors in measurement set-ups were known to cause a large variation in the reported resistivities of the biological tissues, the effects of the different set-ups on the resistivity of finite-volume samples determined using both the four and the two-electrode methods were investigated and reported. The resistivities of saline solutions that were obtained using a commercial conductivity meter and those that were determined using the different set-ups for both the four and the two-electrode methods were compared and evaluated as the inter-electrode spacing or the length of the immersed electrode was varied. The set-ups, which are suitable for resistivity measurement under the above-mentioned circumstances, were then reported.

9.2 Recommendations for Future Research Work

Improvements to the currently used resistivity measurement techniques were presented and experimentally validated in this thesis. Potentially, there are myriads of discoveries yet to be explored in both the proposed four and two-electrode measurement techniques for the biomedical and the power system grounding applications. The recommendations for the future research work can be broadly classified into the following fields:

(i) The proposed geometric factors presented were derived by solving for the potential at all points in a semi-infinite conductive, homogeneous and isotropic medium, which was due to a steady or direct current that enters the medium at the surface. However, resistivity measurements have also been conducted using high frequency alternating currents as excitation sources. Therefore, it will be interesting to study the implementation of the proposed measurement techniques for the determination of the electrical properties of the medium, such as the complex resistivity and the permittivity, in circumstances where high frequency alternating currents are used.

(ii) The proposed geometric factors and measurement techniques were experimentally validated by experiments conducted in saline solutions and agar layers, where the resistivities of the saline solutions and the agar were chosen to approximate that of biological tissues. However, the imperative application of the proposed geometric factors and measurement techniques is for the understanding of the electrical properties of humans and animals. Hence, it will be interesting to extend the current research to conduct *in vivo* resistivity measurements on humans and animals.

(iii) The current research methodologies were derived for and experimentally validated in an isotropic conductive medium. However, it was known that there were differences in the tissues resistivities when measurements were taken in an anisotropic conductive medium. Thus, it will be interesting to extend and implement the proposed measurement techniques in anisotropic conductive media.

(iv) The proposed measurement technique for the determination of the parameters was derived for a two-layer model, which was arranged horizontally. However, lateral changes in the resistivity, which resulted in a vertical fault, are also encountered in the field. Therefore, it will be interesting to extend the proposed measurement technique for applications where there is a vertical fault in the soil structure.

(v) The derived theoretical geometric factors and measurement techniques, which are based on static analysis, are verified from experiments conducted when the dimensions of the measurement system are small. However, when the dimensions are larger, such as soil resistivity measurements, the usage of AC methods may lead to different factors due to the skin effects in the soil. Therefore, it will be advantageous to determine the validity of the proposed methods and the development of the geometric factors for measurements at higher frequencies for system of greater extent.

CANDIDATE'S PUBLICATIONS

1. **Chee-Earn Chong** and Yoke-Lin Tan, "A new geometric factor for *in situ* resistivity measurement using four slender cylindrical electrodes," *IEEE Trans. Biomed. Eng.*, vol. 55, no. 2, pp. 594-602, 2008.
2. Yoke-Lin Tan and **Chee-Earn Chong**, "Resistivity measurement of a small-volume sample using two planar disc electrodes and a new geometric factor," *IEEE Sensors J.*, vol. 8, no. 5, pp. 516-521, 2008.

BIBLIOGRAPHY

[1] Schwan, H. P., "Alternating current spectroscopy of biological substances," *Proc. IRE*, vol. 47, pp. 1841-1855, 1959.

[2] T. J. C. Faes, H. A. van der Meij, J. C. De Munck, and R. M. Heethaar, "The electric resistivity of human tissues (100 Hz - 10 MHz): a meta-analysis of review studies," *Physiol. Meas.*, vol. 20, pp. R1-R10, 1999.

[3] S. Cho and H. Thielecke, "Design of electrode array for impedance measurement of lesions in arteries," *Physiol. Meas.*, vol. 26, pp. S19-S26, 2005.

[4] S. Kun and R. Peura, "Effects of sample geometry and electrode configuration on measured electrical resistivity of skeletal muscle," *IEEE Trans. Biomed. Eng.*, vol. 47, pp. 163-169, 2000.

[5] T. C. Baynham and S. B. Knisley, "Effective epicardial resistance of rabbit ventricles," *Annals Biomed. Eng.*, vol. 27, pp. 96-102, 1999.

[6] C. S. Henriquez and A. A. Papazoglou, "Using computer models to understand the roles of tissue structure and membrane dynamics in arrhythmogenesis," *Proc. IEEE*, vol. 84, pp. 334-354, 1996.

[7] A. E. Pollard, M. J. Burgess, and K. W. Spitzer, "Computer simulations of three-dimensional propagation in ventricular myocardium: Effects of intramural fiber rotation and inhomogeneous conductivity on epicardial activation," *Circ. Res.*, vol. 72, pp. 744-756, 1993.

[8] P. Steendijk, E. T. van der Velde, and J. Baan, "Dependence of anisotropic myocardial electrical resistivity on cardiac phase and excitation frequency," *Basic Res. Cardiol.*, vol. 89, pp. 411-426, 1994.

[9] O. R. M. Ryynanen, J. A. K. Hyttinen, P. H. Laarne, and J. A. Malmivuo, "Effect of electrode density and measurement noise on the spatial resolution of cortical potential distribution," *IEEE Trans. Biomed. Eng.*, vol. 51, pp. 1547-1554, 2004.

[10] D. B. Jorgenson, D. R. Haynor, G. H. Bardy, and Y. Kim, "Computational studies of transthoracic and transvenous defibrillation in a detailed 3-D human thorax model," *IEEE Trans. Biomed. Eng.*, vol. 42, pp. 172-184, 1995.

[11] Strelioff, D., "A computer simulation of the generation and distribution of cochlear potentials," *J. Acoust. Soc. Amer.*, vol. 54, pp. 620-629, 1973.

[12] D. Haemmerich, S. T. Staelin, J. Z. Tsai, S. Tungjitkusolmun, D. M. Mahvi, and J. G. Webster, "*In vivo* electrical conductivity of hepatic tumours," *Physiol. Meas.*, vol. 24, pp. 251-260, 2003.

[13] A. J. Surowiec, S. S. Stuchly, J. R. Barr, and A. Swarup, "Dielectric properties of breast carcinoma and the surrounding tissues," *IEEE Trans. Biomed. Eng.*, vol. 35, pp. 257-263, 1988.

[14] L. A. Geddes and L. E. Baker, *Principles of Applied Biomedical Instrumentation*. 3rd ed. New York: Wiley, 1989.

[15] A. P. Meliopoulos, A. D. Papalexopoulos, R. P. Webb, and C. J. Blattner, "Estimation of soil parameters from driven rod measurements," *IEEE Trans. Power App. Syst.*, vol. 103, pp. 2579-2587, 1984.

[16] J. Ma and F. P. Dawalibi, "Study of influence of buried metallic structures on soil resistivity measurements," *IEEE Trans. Power Del.*, vol. 13, pp. 356-365, 1998.

[17] Blattner, C. J., "Analysis of soil resistivity test methods in two-layer earth," *IEEE Trans. Power App. Syst.*, vol. 104, pp. 3603-3608, 1985.

[18] I. F. Gonos and I. A. Stathopulos, "Estimation of multilayer soil parameters using genetic algorithms," *IEEE Trans. Power Del.*, vol. 20, 2005.

[19] *IEEE Guide for Safety in AC Substation Grounding*, IEEE Std. 80, 2000.

[20] *IEEE Guide for Measuring Earth Resistivity, Ground Impedance, and Earth Surface Potentials of a Ground System*, IEEE Std. 81, 1983.

[21] H. P. Schwan and C. D. Ferris, "Four-electrode null techniques for impedance measurement with high resolution," *Rev. Sci. Instrum.*, vol. 39, pp. 481-485, 1968.

[22] P. Steendijk, G. Mur, E. T. Van Der Velde, and J. Baan, "The four-electrode resistivity technique in anisotropic media: Theoretical analysis and application on myocardial tissue *in vivo*," *IEEE Trans. Biomed. Eng.*, vol. 40, pp. 1138-1148, 1993.

[23] P. L. Guyader, F. Trelles, and P. Savard, "Extracellular measurement of anisotropic bidomain myocardial conductivities. I. Theoretical analysis," *Annals Biomed. Eng.*, vol. 29, pp. 862-877, 2001.

[24] D. C. Barber and B. H. Brown, "Applied potential tomography," *J. Phys. E*, vol. 17, pp. 723-733, 1984.

[25] Wenner, F. C., "A method of measuring earth resistivity," *Bull. Bureau Std.*, vol. 12, pp. 469-482, 1916.

[26] S. Rush, J. A. Abildskov, and R. McFee, "Resistivity of body tissues at low frequencies," *Circ. Res.*, vol. 12, pp. 40-50, 1963.

[27] Y. Wang, P. H. Schimpf, D. R. Haynor, and Y. Kim, "Geometric effects on resistivity measurements with four-electrode probes in isotropic and anisotropic tissues," *IEEE Trans. Biomed. Eng.*, vol. 45, pp. 877-884, 1998.

[28] J. Z. Tsai, H. Cao, S. Tungjitkusolmun, E. J. Woo, V. R. Vorperian, and J. G. Webster, "Dependence of apparent resistance of four-electrode probes on insertion depth," *IEEE Trans. Biomed. Eng.*, vol. 47, pp. 41-48, 2000.

[29] F. L. H. Gielen, W. Wallinga-de Jonge, and K. L. Boon, "Electrical conductivity of skeletal muscle tissue: experimental results from different muscles *in vivo*," *Med. Biol. Eng. Comput.*, vol. 22, pp. 569-577, 1984.

[30] R. Plonsey and R. Barr, "The four-electrode resistivity technique as applied to cardiac muscle," *IEEE Trans. Biomed. Eng.*, vol. 29, pp. 541-546, 1982.

[31] P. N. Robillard and D. Poussart, "Spatial resolution of four electrode array," *IEEE Trans. Biomed. Eng.*, vol. 26, pp. 465-470, 1979.

[32] L. A. Geddes and L. E. Baker, "The specific resistance of biological material - A compendium of data for the biomedical engineer and physiologist," *Med. Biol. Eng.*, vol. 5, pp. 271-293, 1967.

[33] C. Gabriel, S. Gabriel, and E. Corthout, "The dielectric properties of biological tissue: I. Literature survey," *Phys. Med. Biol.*, vol. 41, pp. 2231-2249, 1996.

[34] H. Cao, S. Tungjitkusolmun, Y. B. Choy, J.-Z. Tsai, V. R. Vorperian, and J. G. Webster, "Using electrical impedance to predict catheter-endocardial contact during RF cardiac ablation," *IEEE Trans. Biomed. Eng.*, vol. 49, pp. 247-253, 2002.

[35] H. Cao, M. A. Speidel, Jang-Zern Tsai, M. S. Van Lysel, V. R. Vorperian, and J. G. Webster, "FEM analysis of predicting electrode–myocardium contact from RF cardiac catheter ablation system impedance," *IEEE Trans. Biomed. Eng.*, vol. 49, pp. 520-526, 2002.

[36] M. Akhtari, H.C. Bryant, A.N. Mamelak, L. Heller, J.J. Shih, M. Mandelkern, A. Matlachov, D.M. Ranken, E.D. Best, and W.W. Sutherling, "Conductivities of three-layer human skull," *Brain Topogr.*, vol. 13, pp. 29-42, 2000.

[37] R. S. Baishiki, C. K. Osterberg, and F. Dawalibi, "Earth resistivity measurements using cylindrical electrodes at short spacings," *IEEE Trans. Power Del.*, vol. 2, pp. 64-71, 1987.

[38] Holder, D. S., *Electrical Impedance Tomography: Methods, History and Applications*. Bristol and Philadelphia: Institute of Physics Publishing, 2005.

[39] D. A. Witsoe and E. Kinnen, "Electrical resistivity of lung at 100 kHz," *Med. Biol. Eng.*, vol. 5, pp. 239-248, 1967.

[40] M. F. Suesserman and F. A. Spelman, "Quantitative *in vivo* measurements of inner ear tissue resistivities - I: *In vitro* characterization," *IEEE Trans. Biomed. Eng.*, vol. 40, pp. 1032-1047, 1993.

[41] K. Cheng, P. P. Tarjan, and P. M. Mertz, "Conductivities of pig dermis and subcutaneous fat measured with rectangular pulse electrical current," *Bioelectromagnetics*, vol. 17, pp. 458-466, 1996.

[42] E. Entcheva, J. Eason, F. Claydon, and R. Malkin, "Spatial effects from bipolar current injection in 3D myocardium: Implications for conductivity measurements," *Comp. Cardio.*, vol. 24, pp. 717-720, 1997.

[43] S. B. Baumann, D. R. Wozny, S. K. Kelly, and F. M. Meno, "The electrical conductivity of human cerebrospinal fluid at body temperature," *IEEE Trans. Biomed. Eng.*, vol. 44, pp. 220-223, 1997.

[44] T. Xie, S. C. Tjin, Q. Yang, and S. L. Ng, "Effects of blood's velocity on blood resistivity," *IEEE Trans. Instrum. Meas.*, vol. 47, pp. 1197-1200, 1998.

[45] M. Akhtari, H.C. Bryant, A.N. Mamelak, E. R. Flynn, L. Heller, J.J. Shih, M. Mandelkern, A. Matlachov, D.M. Ranken, E.D. Best, M. A. Dimauro, R. R. Lee, and W.W. Sutherling, "Conductivities of three-layer live human skull," *Brain Topogr.*, vol. 14, pp. 151-167, 2002.

[46] J. Z. Tsai, J. A. Will, S. H. Van Stelle, H. Cao, S. Tungjitkusolmun, Y. B. Choy, D. Haemmerich, V. R. Vorperian, and J. G. Webster, "Error analysis of tissue resistivity measurement," *IEEE Trans. Biomed. Eng.*, vol. 49, pp. 484-494, 2002.

[47] J. Z. Tsai, J. A. Will, S. H. Van Stelle, H. Cao, S. Tungjitkusolmun, Y. B. Choy, D. Haemmerich, V. R. Vorperian, and J. G. Webster, "*In-vivo* measurement of swine myocardial resistivity," *IEEE Trans. Biomed. Eng.*, vol. 49, pp. 472-483, 2002.

[48] Xueli Zhao, Y. Kinouchi, E. Yasuno, D. Gao, T. Iritani, T. Morimoto, and M. Takeuhi, "A new method for noninvasive measurement of multilayer tissue conductivity and structure," *IEEE Trans. Biomed. Eng.*, vol. 51, pp. 362-370, 2004.

[49] L. F. Fuks, M. Cheney, D. Isaacson, D. G. Gisser, and J. C. Newell, "Detection and imaging of electric conductivity and permittivity at low frequency," *IEEE Trans. Biomed. Eng.*, vol. 38, pp. 1106-1110, 1991.

[50] J. C. Newell, Y. Peng, P. M. Edic, R. S. Blue, H. Jain, and R. T. Newell, "Effect of electrode size on impedance images of two- and three-dimensional objects," *IEEE Trans. Biomed. Eng.*, vol. 45, pp. 531-534, 1998.

[51] J. L. Mueller, D. Isaacson, and J. C. Newell, "A reconstruction algorithm for electrical impedance tomography data collected on rectangular electrode arrays," *IEEE Trans. Biomed. Eng.*, vol. 46, pp. 1379-1386, 1999.

[52] R. G. van Nostrand and K. L. Cook, *Interpretation of Resistivity Data*. Washington: United States Printing Office, 1966.

[53] Gish, O. H., "Preliminary earth-resistivity measurements on the site of the Department of Terrestrial Magnetism at Washington, D.C.," *Carneige Inst. Washington Year Book*, vol. 23, pp. 179-180, 1924.

[54] W. J. Rooney and O. H. Gish, "Measurements of large volumes of undisturbed earth," *Terrestrial Magnetism Atmos. Electricity*, vol. 30, pp. 161-168, 1925.

[55] Rooney, W. J., "Earth resistivity measurements in the copper country of Michigan," *Terrestrial Magnetism Atmos. Electricity*, vol. 32, pp. 97-126, 1927.

[56] Lee, F. W., "Measuring the variation of ground resistivity with a Megger," *U.S. Bur. Mines Tech.*, Paper 440, 1928.

[57] Swartz, J. H., "Resistivity measurements upon artificial beds," *U.S. Bur. Mines Inf. Circ.*, vol. 6445, pp. 9, 1931.

[58] Maxwell, J. C., *A Treatise on Electricity and Magnetism*. New York: Dover Publications, Inc., 1954.

[59] Hummel, J. N., "A theoretical study of apparent resistivity in surface potential methods," *Am. Inst. Mining Metall. Engineers Techl. Pub.*, vol. 418, pp. 3-33, 1931.

[60] S. S. Stefanesco, C. Schlumberger, and M. Schlumberger, "The distribution of electrical potential about a point electrode in an earth of horizontal, homogeneous, and isotropic beds," *J. Physique et Radium*, vol. 1, pp. 132-141, 1930.

[61] Lancaster-Jones, E., "The earth-resistivity method of electrical prospecting," *Mining Mag.*, vol. 43, pp. 19-29, 1930.

[62] Tagg, G. F., "The earth resistivity method of geophysical prospecting: Some theoretical considerations," *Mining Mag.*, vol. 43, pp. 150-158, 1930.

[63] D. O. Ehrenburg and R. J. Watson, "Mathematical theory of electrical flow in stratified media with horizontal, homogeneous and isotropic layers," *Am. Inst. Mining Metall. Engineers Trans.*, vol. 97, pp. 423-442, 1931.

[64] Roman, I., "How to compute tables for determining electrical resistivity of underlying beds and their application to geophysical problems," *U.S. Bur. Mines Tech.*, Paper 502, 1931.

[65] Roman, I., "Some interpretations of earth-resistivity data," *Am. Inst. Mining Metall. Engineers Trans.*, vol. 110, pp. 183-200, 1934.

[66] Pekeris, C. L., "Direct method of interpretation in resistivity prospecting," *Geophysics*, vol. 5, pp. 31-42, 1940.

[67] Maillet, R., "The fundamental equations of electrical prospecting," *Geophysics*, vol. 12, pp. 529-556, 1947.

[68] Blattner, C. J., "Study of driven ground rods and four point soil resistivity tests," *IEEE Trans. Power App. Syst.*, vol. 101, pp. 2837-2850, 1982.

[69] A. P. Meliopoulos and A. D. Papalexopoulos, "Interpretation of soil resistivity measurements: Experience with the model SOMIP," *IEEE Trans. Power Del.*, vol. 1, pp. 142-151, 1986.

[70] Alamo, J. L. del, "A comparison among eight different techniques to achieve an optimum estimation of electrical grounding parameters in two-layered earth," *IEEE Trans. Power Del.*, vol. 8, pp. 1890-1899, 1993.

[71] H. R. Seedher and J. K. Arora, "Estimation of two-layer soil parameters using finite Wenner resistivity expressions," *IEEE Trans. Power Del.*, vol. 7, pp. 1213-1217, 1992.

[72] F. Dawalibi and D. Mukhedkar, "Influence of ground rods on grounding grids," *IEEE Trans. Power App. Syst.*, vol. 98, pp. 2089-2098, 1979.

[73] R. Caldecott and D. G. Kasten, "Scale model studies of station grounding grids," *IEEE Trans. Power App. Syst.*, vol. 102, pp. 558-566, 1983.

[74] R. Caldecott, D. G. Kasten, S. Minkara, and C. X. Chen, "Investigation of soil resistivity measuring techniques using an electrolytic tank," *IEEE Trans. Power App. Syst.*, vol. 103, pp. 2983-2988, 1984.

[75] Webster, J. G., *Medical Instrumentation: Application and Design*. 3rd ed. New York: Wiley, 1998.

[76] Y. Zou and Z. Guo, "A review of electrical impedance techniques for breast cancer detection," *Med. Eng. Phys.*, vol. 25, pp. 79-90, 2003.

[77] J. Zou, J. L. He, R. Zeng, W. M. Sun, G. Yu, and S. M. Chen, "Two-stage algorithm for inverting structure parameters of the horizontal multilayer soil," *IEEE Trans. Magn.*, vol. 40, pp. 1136-1139, 2004.

[78] J. Ma and F. P. Dawalibi, "Influence of inductive coupling between leads on resistivity measurements in multilayer soils," *IEEE Trans. Power Del.*, vol. 13, pp. 999-1004, 1998.

[79] J. M. Nahman and D. Salamon, "A practical method for the interpretation of earth resistivity data obtained from driven rod tests," *IEEE Trans. Power Del.*, vol. 3, pp. 1375-1379, 1988.

[80] Milsom, J., *Field Geophysics*. 3rd ed. West Sussex: Wiley, 2003.

[81] Schwan, H. P., "Four-electrode null techniques for impedance measurement with high resolution," *Rev. Sci. Instrum.*, vol. 39, pp. 481-485, 1968.

[82] K. S. Paulson, M. K. Pidcock, and C. N. McLeod, "A probe for organ impedance measurement," *IEEE Trans. Biomed. Eng.*, vol. 51, pp. 1838-1844, 2004.

[83] Jian-Zhong Bao, C. C. Davis, and R. E. Schmukler, "Impedance spectroscopy of human erythrocytes: System calibration and nonlinear modeling," *IEEE Trans. Biomed. Eng.*, vol. 40, pp. 364-378, 1993.

[84] P. Mirtaheri, S. Grimnes, and O. G. Martinsen,, "Electrode polarization impedance in weak NaCl aqueous solutions," *IEEE Trans. Biomed. Eng.*, vol. 52, pp. 2093-2099, 2005.

[85] D. Schwartzman, I. Chang, J. J. Michele, M. S. Mirotznik, and K. R. Foster, "Electrical impedance properties of normal and chronically infracted left ventricular myocardium," *J. Intervent. Card. Electrophysiol.*, vol. 3, pp. 213-224, 1999.

[86] Y. Feldman, I. Ermolina, and Y. Hayashi, "Time domain dielectric spectroscopy study of biological systems," *IEEE Trans. Dielect. Elect. Insul.*, vol. 10, pp. 728-753, 2003.

[87] Tagg, G. F., *Earth Resistances*. London: George Newnes Limited, 1964.

[88] Palmer, L. S., "Examples of geoelectric surveys," *Procs. IEE*, vol. 106, pp. 231-244, 1959.

[89] Sharma, P. V., *Geophysical Methods in Geology*. 2nd ed. New York: Elsevier, 1986.

[90] Parasnis, D. S., *Principles of Applied Geophysics*. 3rd ed. London: Chapman and Hall, 1979.

[91] W. M. Telford, L. P. Geldart, R. E. Sheriff, and D. A. Keys, *Applied Geophysics*. London; New York: Cambridge University Press, 1976.

[92] Palmer, L. S., "Location of subterranean cavities by geoelectric methods," *The Mining Magazine*, vol. 91, pp. 137-141, 1954.

[93] Sheriff, R. E., *Geophysical Methods*. New Jersey: Prentice Hall, 1989.

[94] Meltzer, A., "Electrical resistivity measurements using the Wenner array to estimate the depth and soil type of a river thaw bulb," *MSc Thesis*, University of Alaska Anchorage, 1998.

[95] S. S. Vinogradov, P. D. Smith, and E. D. Vinogradova, *Canonical Problems in Scattering and Potential Theory Part I: Canonical Structures in Potential Theory*. Boca Raton: Chapman & Hall/CRC, 2001.

[96] Meliopoulos, A. P. S., *Power System Grounding and Transients: An Introduction*. New York and Basel: Marcel Dekker, Inc., 1988.

[97] Bronzino, J. D., *The Biomedical Engineering Handbook: Biomedical Engineering Fundamentals*. 3rd ed. Boca Raton: Taylor & Francis, 2006.

[98] A. P. Meliopoulos, R. P. Webb, and E. B. Joy, "Analysis of grounding systems," *IEEE Trans. Power App. Syst.*, vol. 100, pp. 1039-1048, 1981.

[99] Wait, J. R., *Geo-Electromagnetism*. New York: Academic Press, Inc., 1982.

[100] E. C. Stoner and E. P. Wolfarth, "A mechanism of magnetic hysteresis in heterogeneous alloys," *Phil. Trans. Roy. Soc.*, vol. A240, pp. 599-642, 1948.

[101] H. Braunisch, C. O. Ao, K. O'Neill, and J. A. Kong, "Magnetoquasistatic response of conducting and permeable prolate spheroid under axial excitation," *IEEE Trans. Geosci. Remote Sensing*, vol. 39, pp. 2689-2701, 2001.

[102] J. Ruohonen, P. Ravazzani, and F. Grandori, "An analytical model to predict the electric field and excitation zones due to magnetic stimulation of peripheral nerves," *IEEE Trans. Biomed. Eng.*, vol. 42, pp. 158-161, 1995.

[103] M. Tejedor, H. Rubio, L. Elbaile, and R. Iglesias, "External fields created by uniformly magnetized ellipsoids and spheroids," *IEEE Trans. Magn.*, vol. 31, pp. 830-836, 1995.

[104] A. Butera and J. A. Barnard, "Ferromagnetic resonance of permalloy artificially nanostructured films," *IEEE Trans. Magn.*, vol. 37, pp. 2213-2215, 2001.

[105] Chang, H., "Fields external to open-structure magnetic devices represented by ellipsoid or spheroid," *British J. Appl. Phys.*, vol. 12, pp. 160-163, 1961.

[106] P. M. Morse and H. Feshbach, *Methods of Theoretical Physics*. New York: McGraw-Hill Pub. Com., 1953.

[107] P. Moon and D. E. Spencer, *Field Theory Handbook*. 2nd ed. Berlin, New York: Springer-Verlag, 1971.

[108] A. J. Bard and L. R. Faulkner, *Electrochemical Methods: Fundamentals and Applications*. 2nd ed. New York: Wiley, 2001.

[109] P. Hua, E. J. Woo, J. G. Webster, and W. J. Tompkins, "Using compound electrodes in electrical impedance tomography," *IEEE Trans. Biomed. Eng.*, vol. 40, pp. 29-34, 1993.

[110] I. Jurgens, J. Rosell, and P. J. Riu, "Electrical impedance tomography of the eye: *In vitro* measurements of the cornea and the lens," *Physiol. Meas.*, vol. 17, pp. A187-A195, 1996.

[111] A. Ivorra, R. Gomez, N. Noguera, R. Villa, A. Sola, L. Palacios, G. Hotter, and J. Aguilo, "Minimally invasive silicon probe for electrical impedance measurements in small animals," *Biosen. Bioelect.*, vol. 391, pp. 391-399, 2003.

[112] T. Suselbeck, H. Thielecke, I. Weinschenk, A. Reininger-Mack, T. Stieglitz, J. Metz, M. Borggrefe, A. Robitzki, and K. K. Haase, "*In vivo* intravascular electric impedance spectroscopy using a new catheter with integrated microelectrodes," *Basic Res. Cardiol.*, vol. 100, pp. 28-34, 2005.

[113] Y. Kim, H.-W Woo, and A. E. Luedtke, "Impedance tomography and its application in deep venous thrombosis detection," *IEEE Eng. Med. Biol. Mag.*, vol. 8, pp. 46-49, 1989.

[114] Y. Kim and P. H. Schimpf, "Electrical behavior of defibrillation and pacing electrodes," *Proc. IEEE*, vol. 84, pp. 446-456, 1996.

[115] S. Al-Zeibak and N. H. Saunders, "A feasibility study of *in vivo* electromagnetic imaging," *Phys. Med. Biol.*, vol. 38, pp. 151-160, 1993.

[116] A. Morris, H. Griffiths, and W. Gough, "A numerical model for magnetic induction tomographic measurements in biological tissues," *Physiol. Meas.*, vol. 22, pp. 113-119, 2001.

[117] H. Griffiths, W. R. Stewart, and W. Gough, "Magnetic induction tomography: A measuring system for biological tissues," *Ann. NY Acad. Sci.*, vol. 873, pp. 335-345, 1999.

[118] Z. Popovic and B. D. Popovic, *Introductory Electromagnetics*. New Jersey: Prentice Hall, 2000.

[119] Chee-Earn Chong and Yoke-Lin Tan, "A new geometric factor for *in situ* resistivity measurement using four slender cylindrical electrodes," *IEEE Trans. Biomed. Eng.*, In Press, doi:10.1109/TBME.2007.903704.

[120] *YSI EC300 Operations Manual*. YSI Environmental, Inc, Yellow Springs OH, 2003.

[121] *LeCroy WaveSurfer Xs Series Oscilloscopes Operator's Manual*. LeCroy Corporation, Chestnut Ridge, New York, 2006.

[122] R. Plonsey and D. B. Heppner, "Consideration of quasi-stationarity in electrophysiological systems," *Bull. Math. Biophys.*, vol. 29, pp. 657-664, 1967.

[123] F. Dawalibi and C. J. Blattner, "Earth resistivity measurement interpretation techniques," *IEEE Trans. Power App. Syst.*, vol. 103, pp. 374-382, 1984.

[124] Alamo, J. L. del, "A second order gradient technique for an improved estimation of soil parameters in a two-layer earth," *IEEE Trans. Power Del.*, vol. 6, pp. 1166-1170, 1991.

[125] T. Takahashi and T. Kawase, "Analysis of apparent resistivity in a multi-layer earth structure," *IEEE Trans. Power Del.*, vol. 5, pp. 604-612, 1990.

[126] Sunde, E. D., *Earth Conduction Effects in Transmission Systems*. New York: Dover Publications, Inc., 1968.

[127] Calixto, P., "Soil resistivity measurement: Two-layer model, proposed revisions to IEEE Standard 80-2000 and IEEE Standard 81-1983," *IEEE Power Engin. Rev.*, vol. 22, pp. 66-68, 2002.

[128] *Getting started with MATLAB*: Version 7, The MathWorks, Inc., 3 Apple Hill Drive, Natick, MA 01760-2098.

[129] Hyams, D. G., *CurveExpert 1.3*. 2005. Avaliable: http://curveexpert.webhop.biz/.

[130] D. A. Hettrick, J. H. Battocletti, P. S. Pagel, G. G. Vurek, J. P. Tessmer, J. R. Kersten, and D. C. Warltier, "Correlation of esophageal conductance measurements with aortic and left ventricular diameters and stroke volume," *IEEE Trans. Biomed. Eng.*, vol. 47, pp. 559-564, 2000.

[131] Briggs, L. J., "Electrical instruments for determining the moisture, content, and soluble salt content of soils," *U.S. Dept. Agr. Bul. 15*, pp. 1-35, 1899.

[132] D. R. Davis and D. W. Kennard, "Influence of electric current on the skin," *Nature (London)*, vol. 4821, pp. 1186-1187, 1962.

[133] E. T. McAdams, J. Jossinet, A. Lackermeier, J. A. McLaughlin, and D. Macken, "The linear and non-linear electrical properties of the electrode-electrolyte interface," *Biosen. Bioelect.*, vol. 10, pp. 67-74, 1995.

[134] J. O. M. Bockris and A. K. N. Reddy, *Modern Electrochemistry*. New York: Plenum, 1977.

[135] Lyklema, J., *Fundamentals of Interface and Colloid Science*. London: Academic, 1995.

[136] T. Ragheb and L. A. Geddes, "Electrical properties of metallic electrodes," *Med. Biol. Eng. Comput.*, vol. 28, pp. 182-186, 1990.

[137] Y. Feldman, A. Andrianov, E. Polygalov, I. Ermolina, G. Romanychev, Y. Zuev, and B. Milgotin, "Time domain dielectric spectroscopy: An advanced measuring system," *Rev. Sci. Instrum.*, vol. 67, pp. 3208-3216, 1996.

[138] Jones, R. G., "Measurements of the electrical conductivity of water," *IEE Procs. Sci. Meas. Technol.*, vol. 149, pp. 320-322, 2002.

[139] C. Grosse and M. C. Tirado, "Low-frequency dielectric spectroscopy of colloidal suspensions," *J. Non-Cryst. Solids*, vol. 305, pp. 386-392, 2002.

[140] H. P. Schwan, G. Schwarz, J. Maczuk, and H. Pauly, "On the low frequency dielectric dispersion of colloidal particles in electrolyte solution," *J. Phys. Chem.*, vol. 66, pp. 2626-2635, 1962.

[141] K-H. Lim and E. I. Francis, "Electrical properties of aqueous dispersions of polymer microspheres," *J. Colloid Interface Sci.*, vol. 110, pp. 201-213, 1986.

[142] L. A. Geddes and C. P. Da Costa, "The specific resistance of canine blood at body temperature," *IEEE Trans. Biomed. Eng.*, vol. 20, pp. 51-53, 1973.

[143] L. A. Geddes, C. P. Da Costa, and G. Wise, "The impedance of stainless-steel electrodes," *Med. Biol. Eng.*, vol. 9, pp. 511-521, 1971.

[144] Geddes, L. A., "Measurement of electrolytic resistivity and electrode-electrolyte impedance with a variable-length conductivity cell," *Chemical Instrumentation*, vol. 4, pp. 157-168, 1973.

[145] L. A. Geddes and C. Sadler, "The specific resistance of blood at body temperature," *Med. Biol. Eng.*, vol. 11, pp. 336-339, 1973.

[146] R. Hayakawa, H. Kanda, M. Sakamoto, and Y. Wada, "New apparatus for measuring the complex dielectric constant of a highly conductive material," *Japan. J. Appl. Phys.*, vol. 14, pp. 2039-2052, 1975.

[147] H. Nakamura, Y. Husimi, and A. Wada, "Time domain measurement of dielectric spectra of aqueous polyelectrolyte solutions at low frequencies," *J. Appl. Phys.*, vol. 52, pp. 3053-3061, 1981.

[148] D. F. Myers and D. A. Saville, "Dielectric spectroscopy of colloidal suspensions," *J. Colloid Interface Sci.*, vol. 131, pp. 448-460, 1989.

[149] C. Iliescu, D. P. Poenar, M. Carp, and F. C. Loe, "A microfluidic device for impedance spectroscopy analysis of biological samples," *Sens. Actuators B: Chem.*, In Press, doi:10.1016/j.snb.2006.08.009.

[150] D. He, M. A. Shannon, and N. R. Miller, "Micromachined silicon electrolytic conductivity probes with integrated temperature sensor," *IEEE Sensor J.*, vol. 5, pp. 1185-1196, 2005.

[151] C. Ionescu-Zanetti, R. M. Shaw, J. Seo, Y.-N. Jan, L. Y. Jan, and L. P. Lee, "Mammalian electrophysiology on a microfluidic platform," *Proc. Nat. Acad. Sci.*, vol. 102, pp. 9112-9117, 2005.

[152] X. Li, K. G. Klemic, M. A. Reed, and F. J. Sigworth, "Microfluidic system for planar patch clamp electrode arrays," *Nano Lett.*, vol. 6, pp. 815-819, 2006.

[153] M.-S. Chun, M. S. Shim, and N. W. Choi, "Fabrication and validation of a multi-channel type microfluidic chip for electrokinetic streaming potential devices," *Lab on a Chip*, vol. 6, pp. 302-309, 2006.

[154] T. Lehnert, M. A. M. Gijs, R. Netzer, and U. Bischoff, "Realization of hollow SiO2 micronozzles for electrical measurements on living cells," *Appl. Phys. Lett.*, vol. 81, pp. 5063-5065, 2002.

[155] K. A. Dunphy-Guzmán, R. N. Karnik, J. S. Newman, and A. Majumdar, "Spatially controlled microfluidics using low-voltage electrokinetics," *J. Microelectromech. Syst.*, vol. 15, pp. 237-245, 2006.

[156] B. J. Polk, A. Stelzenmuller, G. Mijares, W. MacCrehan, and M. Gaitan, "Ag/AgCl microelectrodes with improved stability for microfluidics," *Sens. Actuators B: Chem.*, vol. 114, pp. 239-247, 2006.

[157] Norman, R. A., *Principles of Bioinstrumentation*. New York: Wiley, 1988.

[158] Q. Ramadan, V. Samper, D. Poenar, and C. Yu, "Magnetic-based microfluidic platform for biomolecular separation," *Biomed. Microdevices*, vol. 8, pp. 151-158, 2006.

[159] X. J. Liang, A. Q. Liu, C. S. Lim, T. C. Ayi, and P. H. Yap, "Determining refractive index of single living cell using an integrated microchip," *Sens. Actuators A: Phys.*, In Press, doi:10.1016/j.sna.2006.06.045,, 2006.

[160] A. R. Minerick, R. Zhou, P. Takhistov, and H.-C Chang, "Manipulation and characterization of red blood cells with alternating current fields in microdevices," *Electrophoresis*, vol. 24, pp. 3703-3717, 2003.

[161] Yoke-Lin Tan and Chee-Earn Chong, "Resistivity measurement of a small-volume sample using two planar disc electrodes and a new geometric factor," *IEEE Sensors J.*, accepted for publication 2007.

[162] D. P. Poenar, C. Iliescu, M. Carp, A. J. Pang, and K. J. Leck, "Glass-based microfluidic device fabricated by parylene wafer-to-wafer bonding for impedance spectroscopy," *Sens. Actuators A: Phys.*, In Press, doi:10.1016/j.sna.2006.10.009.

[163] Ansoft, *Maxwell SV*, Avaliable: http://www.ansoft.com/maxwellsv/.